Universität Stuttgart

Electron cyclotron emission investigations at the stellarator TJ-K

Von der Fakultät Energie-, Verfahrens- und Biotechnik der Universität Stuttgart zur Erlangung der Würde eines Doktors der Naturwissenschaften (Dr. rer. nat.) genehmigte Abhandlung

vorgelegt von
Gabriel Sichardt
aus Schmalkalden

Hauptberichter:	Prof. Dr. Thomas Hirth
1. Mitberichter:	Prof. Dr. Marc Kreutzbruck
2. Mitberichter:	Priv.-Doz. Dr. Heinrich P. Laqua
Tag der mündlichen Prüfung:	7. Mai 2020

Institut für Grenzflächenverfahrenstechnik und Plasmatechnologie der Universität Stuttgart

2020

Kurzfassung

Mikrowellendiagnostiken sind in der fusionsorientierten Plasmaphysik weit verbreitet. Insbesondere die Messung der Elektron-Zyklotron-Emission (ECE) wird routinemäßig zur zuverlässigen Bestimmung der radialen Temperaturverteilung im Plasma verwendet. Sie wird aber auch zur Bestimmung der Elektronendichte und Detektion überthermischer Elektronen eingesetzt und ist aufgrund ihres nicht-invasiven Messverfahrens hervorragend zur Diagnostik der extremen Bedingungen, die in Fusionsplasmen vorherrschen, geeignet. So wird das Plasma weder beeinflusst, noch die Diagnostik beschädigt. Obwohl ECE-Diagnostiken schon seit vielen Jahrzehnten eingesetzt werden, sind sie weiterhin Gegenstand aktueller Forschungs- und Entwicklungsarbeiten. Vor allem die korrekte Auswertung und Interpretation der Messungen an Plasmen niedriger Dichte und Temperatur, die im Gegensatz zu Fusionsplasmen optisch dünn sind, stellt eine Herausforderung dar. Der in Stuttgart befindliche Stellarator TJ-K wird mit solch dünnen Plasmen betrieben, was aber auch den Einsatz von Langmuir-Sonden zur Temperaturbestimmung und somit zum Test und zur Kalibrierung einer neuen ECE-Diagnostik gestattet.

Diese Arbeit widmet sich dem Aufbau einer Messanordnung für ECE an TJ-K, sowie deren Optimierung und Anwendung. Dazu werden Modellierung, Simulation und Experiment kombiniert, um die Prozesse am spezifischen Aufbau zu verstehen und die Diagnostik an diese anzupassen.

Der erste Teil dieser Arbeit beschreibt die Entwicklung und den Einsatz der Diagnostik. Dazu werden der Transport und die Ausbreitung der ECE im dreidimensional modellierten Plasma simuliert. Daraus wird ein Optimierungsansatz abgeleitet: Durch geeignete Positionierung eines angepassten Spiegels zur definierten Reflexion der ECE wird ein abstimmbares Resonatorsystem gebaut, das die Ortsauflösung der Diagnostik verbessert. Nach Identifizierung der Messsignale als ECE in Abgrenzung zur thermischen Bremsstrahlung wird das Messsystem mit einer Heiß-Kalt-Methode kalibriert. Obwohl das Plasma infolge der geringen optischen Dichte nur $0,2\,\%$ der Schwarzkörperintensität emittiert, wurden mittels ECE gemessene Elektronentemperaturen mit denen aus Langmuir-Sonden-Messungen bestätigt.

Im zweiten Teil werden numerisch Elektronentrajektorien im 3D-Magnetfeld von TJ-K in Abhängigkeit der kinetischen Teilchenenergien studiert. Die Trajektorien liegen auf Drift-Flächen, die von der Geschwindigkeit und Orientierung des Elektrons zum Magnetfeld abhängen. Inwieweit Elektronen auf größeren Drift-Flächen von der Gefäßwand direkt aufgefangen werden und so zu einem toroidalen Nettostrom führen, wird mit Simulationen verschiedener Maxwell-Boltzmann-Geschwindigkeitsverteilungen sowie monoenergetischer Verteilungen mit je mehreren Millionen Elektronen untersucht. Es zeigt sich, dass besonders Elektronenpopulationen zusätzlich zur thermischen Geschwindigkeitsverteilung bei Teilchenenergien von beispielsweise 1 keV, sogenannte überthermische Elektronen, besonders hohe Ströme erzeugen. Auch bereits thermische Elektronen mit typischen Energien von 10 eV liefern toroidale Nettoströme, die vergleichbar mit experimentell beobachteten Strömen sind. Die aufgebaute ECE-Diagnostik erlaubt zeitaufgelöste Messungen lokaler Temperaturen zur Korrelation mit toroidalen Strömen.

Abstract

Microwave diagnostics are widely used in fusion-oriented plasma research. Especially, electron cyclotron emission (ECE) measurements are routinely employed for reliable investigations of radial temperature profiles. Furthermore, an ECE diagnostic can be used to measure electron densities or detect superthermal electrons. Due to its non-invasive character, it is well suited for application to extreme conditions like in fusion plasmas since neither the plasma is perturbed nor the diagnostic harmed. Despite decades of development, ECE diagnostics are still subject of current research and development. Especially the correct interpretation of measurements at plasmas with low densities and temperatures, which are in contrast to fusion plasmas optically thin, is challenging. The stellarator experiment TJ-K in Stuttgart is operated with such thin plasmas allowing for the use of Langmuir probes for temperature measurements and thus as a benchmark for a new ECE diagnostic system.

This work is about the development, optimization, construction and application of an ECE diagnostic for TJ-K. Modeling, simulation and experiment are combined to understand the processes at the specific experiment and to adapt the setup to these conditions.

The first part of this thesis describes the development and test of the diagnostic. To this end, the transport and propagation of electron cyclotron radiation is simulated in the three-dimensionally modeled plasma of TJ-K. From the results, an optimization approach is derived: with a suitably positioned and optimally curved mirror for defined reflections, a tunable resonator system is built that improves the localization of the measurements significantly. After identification of the measurement signals as ECE opposed to thermal bremsstrahlung, the measurement system is calibrated with the hot-cold method. Although only about 0.2 % of the black body intensity is emitted from the optically thin plasma the temperatures obtained from the ECE diagnostic could be verified by Langmuir probe measurements.

In the second part, numerical investigations of electron trajectories in the 3D magnetic field of TJ-K are employed to study their dependence on the kinetic particle energy. The trajectories form drift orbits which depend on the speed and orientation of the electron compared to the magnetic field. To what extent electrons on larger drift orbits collide with the vessel wall and thus contribute to toroidal net currents is investigated using simulations with different velocity distributions. It becomes apparent that especially electron populations additional to the thermal distribution at higher energies like for instance 1 keV, superthermal electrons, can result in large toroidal net currents. Already thermal electrons with typical energies of 10 eV provide numerically toroidal net currents that are comparable to the experimentally observed currents. The installed ECE diagnostic allows for temporally resolved measurements of local radiation temperatures for correlation with toroidal net currents.

List of symbols

The number sign # as prefix indicates the number of a measurement at TJ-K, which is counted according to the lab book with absolute numbers regardless of the current measurement campaign. These numbers are also called shot numbers which originates from the short measurement durations of tokamak experiments.
The alphabetic symbols used in this thesis are listed in the following two tables for Latin and Greek symbols, respectively.

Latin symbols

Symbol	Description
a	grid constant of the FDTD simulations
a_c	distance from coax coupler pin to the coupler flange
a_n	exponent parameter in the 1D density profile regression
a_1, a_2	semiaxes of the polarization ellipse
A	area
A_a, A_b	transition probabilities for spectral line a and b
A_{probe}	surface of the plasma-exposed probe tip of a Langmuir probe
b	measurement bandwidth of the ECE diagnostic
b_c	distance between coupler flange and origin of the movable wall at $d_c = 0$
$\vec{B}$, $\vec{B}_1$	static background magnetic field, magnetic field of a microwave
B_{ax}	magnetic field strength at the magnetic axis at port O5
c	speed of light in vacuum
d	relative position between last closed flux surface and vessel wall
d_c	position of the tunable short of the diagnostic resonator
e	elementary charge
$\vec{E}_1$	electric field of an electromagnetic wave
$\tilde{E}$	time-variant electric field of a signal
$\hat{E}$	electric field amplitude of a signal
E_a, E_b	excitation energy corresponding to the spectral lines a and b
f, f_a, f_b	frequency, frequencies of spectral lines a and b
f_{ce}, f_{pe}	electron cyclotron frequency, electron plasma frequency
f_{UH}, f_R	upper hybrid frequency, right-hand cutoff frequency
$f_M(\vec{v})$	Maxwellian probability density function
$\vec{F}$	force

$\vec{F}_L$, $F_{L,x}$, $F_{L,y}$	Lorentz force and its components in x and y direction
$\vec{F}_{cf}$	centrifugal force
g	gain factor (of an amplifier) (chapter 4)
g_a, g_b	statistical weight of spectral line a and b
G	Gaussian random number (chapter 5)
h	Planck's constant
i	first grid point index in the FDTD simulations
I	microwave intensity (chapter 4), toroidal net current (chapter 5)
I_L	current at a Langmuir probe (section 3.4.3)
I_e, $I_{i,sat}$, $I_{e,sat}$	electron current, ion saturation current, electron saturation current
I_{mono}	toroidal net current from a monoenergetic population
I_a, I_b	intensities of spectral lines a and b
j	second grid point index in the full-wave simulations
j_l	emissivity of harmonic l
$\vec{j}$	current density
k	third grid point index in the full-wave simulations
k_B	Boltzmann constant
l	harmonic number
l_{coll}	mean free path
L	path length of the interferometer signal
L_B	gradient length of the magnetic field
m, m_e, m_i	rest mass, electron rest mass, ion rest mass
n_e, n_i, n_0	electron density, ion density, neutral particle density
N	refractive index
N_m	number of modes in a resonator cavity
p_0	neutral gas pressure (before a plasma discharge)
p	probability
P	microwave heating power
P_b	power emitted by thermal bremsstrahlung
P_l	ECE microwave power emitted at harmonic l
P_{meas}, P_{rec}	time-integrated measured power, received fluctuating power at the analyzer
P_{RJ}	Rayleigh-Jeans power
q, q_{dr}, q_{TJK}	resonator quality factor, of the diagnostic resonator and the TJ-K vessel
Q, Q_{ant},	contributions to the measurement signal, in front of the antenna,
$Q_{tor}, Q^{(i,j,k)}$	Q in the entire torus and at grid point (i,j,k)
r	coordinate along the minor radius of the torus
$\vec{r}$	position vector like in $\vec{r} = (x, y, z)$
r_0	minor radius of the toroidal vacuum vessel, $r_0 = 0.175\,\mathrm{m}$ for TJ-K
r_{dr}	effective reflection coefficient in the diagnostic resonator for one round trip
r_{vh}	ratio of the current through the vertical and helical coil of TJ-K
R	coordinate along the major radius of the torus
$\vec{R}_c$	curvature radius vector of the magnetic field

R_0	major radius of the toroidal vacuum vessel, $R_0 = 0.6\,\mathrm{m}$ for TJ-K
R_{vert}, R_{hor}	(approximately) vertical and horizontal ECE mirror curvature radii
R_{vessel}, R_{LCFS}	position of vessel and last closed flux surface along the major radius
$\vec{s}$	microwave propagation path
t, t_0, t_1	time, points in time
t_{dr}, t_{TJK}	energy decay time of the diagnostic resonator and TJ-K as resonator
T_e, T_i	electron temperature, ion temperature (in Kelvin)
T_{BB}, T_{rad}	black body temperature, radiation temperature
$T(G)$	transform of a velocity distribution
$\vec{u}$	Stokes vector describing the polarization of a wave (see section 4.5)
u_1, u_2	uniformly distributed random numbers, in section 5.1.3
u_{Ar}, u_{He}	number of argon or helium discharges used in the evaluation
U	voltage
$\vec{v}$	velocity
$\vec{v}_D$, $\vec{v}_D^c$, $\vec{v}_D^\nabla$	drift velocity, curvature drift velocity, gradient drift velocity
$v_\parallel$, $v_\perp$	speed parallel and perpendicular to the background magnetic field
v_{th}	thermal speed (the most probable speed in a 3D Maxwellian distribution)
v_{ph}	phase speed of an electromagnetic wave
V	volume
V_t	volume of a torus with TJ-K size
w, w_0	beam radius, beam waist
W, $W_\perp$, $W_\parallel$	kinetic energy, perpendicular and parallel to the background magnetic field
x, y	horizontal coordinates in a Cartesian coordinate system (see section 3.1)
z	vertical coordinate in Cartesian and toroidal coordinate systems
z_a	coordinate along the axis of the antenna in section 4.3.1
z_0	beam waist position relative to the antenna aperture

Greek symbols

Symbol	Description
α	absorption coefficient
γ	Lorentz factor
δ	skin depth (length an electromagnetic wave penetrates a medium)
ε_0	electric field constant
η	pitch angle of an electron $\eta = \arctan\left(v_\perp / v_\parallel\right)$
θ	poloidal angle
Θ	observation angle of the diagnostic compared to the magnetic field vector
κ	shape function of the 1D electron density profile
λ, λ_{wg}	wavelength, wavelength inside a waveguide

$\ln(\Lambda)$	Coulomb logarithm
μ, μ_0, μ_r	magnetic permeability, vacuum permeability and relative permeability
ρ	charge density
ρ_L	Larmor radius
$\boldsymbol{\sigma}$,σ	electric conductivity, as tensor and scalar
σ_{e0}	electron-neutral collision cross-section
$\sigma_{\mathrm{Ar,eff.}}$, $\sigma_{\mathrm{He,eff.}}$	effective electron-neutral collision cross-section in argon and helium
τ_{coll}	collision time
τ	optical depth
τ_{ee}, $\tau_{ee}^{\parallel}$, $\tau_{ee}^{\perp}$	electron-electron collision time, parallel and perpendicular
τ_{ei}, $\tau_{ei}^{\parallel}$, $\tau_{ei}^{\perp}$	electron-ion collision time, parallel and perpendicular
τ_{e0}, τ_{tot}	electron-neutral and total collision time
τ_n, τ_E	particle confinement time, energy confinement time
φ	phase of an electromagnetic wave
ϕ	toroidal angle
Φ_{fl}, Φ_p	floating potential, plasma potential
Φ_l	shape function of ECE emissivity and absorption for harmonic number l
χ	elliptization angle of the polarization
Ψ	polarization angle
ω, ω_{pe}	angular frequency, angular electron plasma frequency
ω_{ce}, $\omega_{ce,l}$	angular electron cyclotron frequency, of harmonic l
Ω	solid angle

List of figures

1.1. Illustration of a deuterium-tritium fusion reaction. 19
1.2. Illustration of a tokamak setup. 20
1.3. Diagram of the thesis structure. 22

3.1. Schematic top view of TJ-K with the diagnostics used for ECE measurements, indication of the port numbering and definition of the coordinate axes. 27
3.2. Vertical cut through a schematic torus showing two poloidal cross-sections with the coordinates being indicated. 28
3.3. Perspective illustration of the vessel curvatures. 29
3.4. Scheme of TJ-K with a cut-out. Flux surfaces and poloidal cross-sections of flux surfaces for different port positions are shown. 30
3.5. Absolute value of the magnetic field for a current of 1140 A and a current ratio of 57 % in the poloidal plane of an outer port. 31
3.6. Absolute value of the magnetic field and its gradient along the major radius at z=0 for the outer port O5 with regression curves. 32
3.7. Vertical shift of the upper turning point and horizontal shift the outer turning point of a flux surface compared to the flux surface at $\phi = 90°$ (port O5). 32
3.8. Relative emitted intensity of the main spectral lines of a helium and an argon plasma for different thermal energies. 35
3.9. Current-voltage characteristic of a Langmuir probe. 36

4.1. Frequency distribution of the second harmonic shape function for perpendicular observation of electron cyclotron emission in TJ-K for 15 GHz. 43
4.2. Intensity from one-dimensional integration of the radiation transport equation in TJ-K for different thermal electron energies and numbers of passes through the plasma. . . . 47
4.3. Resonance and cutoff frequencies in the ECE frequency range at the central line of an outer port of TJ-K. 49
4.4. Illustration of the grid setup in the Yee algorithm. 51
4.5. 1D density profile from Langmuir probe measurements with fitted super-Gaussian approximation. 54
4.6. Relative distance to the vessel wall measured from the LCFS and evaluated along rays from the magnetic axis. 55
4.7. Density distribution in the poloidal plane at port O6 modeled from Langmuir probe measurements. 55

4.8. Typical 1D profile of the thermal electron energy measured with a Langmuir probe. . . 56
4.9. Distribution of the time-averaged squared electric field in the toroidal mid-plane for a 15 GHz microwave determined in a 3D full-wave simulation without and with mirror. . 57
4.10. Distribution of the time-averaged squared electric field in the poloidal plane at $\phi = 90°$ and $\phi = 270°$ for a 15 GHz microwave, determined in a 3D full-wave simulation for TJ-K without and with mirror. 58
4.11. Perspective 3D view on the contributions $Q^{(i,j,k)}$ to the ECE signals obtained in 3D FDTD simulations. 58
4.12. Electric field line structure of the TE11, TM11 and TE12 circular waveguide modes. . 61
4.13. Electric field lines and absolute electric field in arbitrary units of the TE11 circular waveguide mode. 61
4.14. Optimized shape of the ECE antenna and a reference antenna optimized in the 12-13 GHz range and simulated mode purity. 62
4.15. Measured ECE antenna patterns in the horizontal plane. 63
4.16. Measured maximium power of the main lobe for different frequencies. 64
4.17. Electric wave field contour plot showing the wavefront curvature with adjusted circles in vacuum and with plasma. 65
4.18. Phase front curvature radii resulting from full-wave simulations in the vertical and horizontal plane with analytical calculation as a reference for the vacuum case. 66
4.19. Schematic view of the in-vessel components of the ECE diagnostic system at TJ-K and photograph of the diagnostic. 66
4.20. Schematic vertical cut of the tunable resonator setup with standing wave pattern. . . . 67
4.21. Schematic of the tunable coupler. 68
4.22. Time trace of the diode signal from the diagnostic resonator during input signal modulation. 70
4.23. Time trace of the diode signal from the vacuum vessel when the input signal is modulated. 71
4.24. Calculated temperature dependence of the power emitted by bremsstrahlung in the temperature range of TJ-K with 3 MHz bandwidth. 74
4.25. Received microwave power at 14.5 GHz over $n_e T_e^2$ and $n_e^2/\sqrt{T_e}$. 76
4.26. Mean and standard deviation of the received microwave power at 14.5 GHz over $n_e T_e^2$ and $n_e^2/\sqrt{T_e}$, evaluated in microwave power intervals. 76
4.27. Time traces of 15 GHz emission, the interferometer, ion saturation current of a Langmuir probe and the optical diode in a modulated discharge. 77
4.28. Polarization ellipse with the definitions of the angles and axes. 78
4.29. Rotation angle of the polarization for a wave passing through a magnetized plasma and back again. 80
4.30. Polarization ellipses at ten equidistant points along the path from the ECE antenna to the vessel wall. 81
4.31. Measured transfer function of the low pass filter and measured gain characteristic of the LNA amplifiers. 83
4.32. Received power spectrum at the spectrum analyzer from a liquid nitrogen cooled microwave absorber and at room temperature. 85

4.33. Electron temperatures from ECE measurements compared to Langmuir measurements. Evaluation with T_e, with T_e^2 and $n_e T_e^2$ dependence for low optical depths are shown. . 88

5.1. Experimentally obtained absolute toroidal net currents in TJ-K for different neutral gas pressures with two microwave heating frequencies used simultaneously and signed toroidal net current for different powers of the 8 GHz heating. 91
5.2. Vertical drift of an electron in a magnetic field gradient. 94
5.3. Electron trajectories compared to the magnetic field line as projection to a poloidal plane for various electron energies and different perpendicular speeds. 96
5.4. Schematic illustration of the drift velocities that lead to drift orbits of an electron in a toroidal plasma. 96
5.5. Poincaré plot of a co-moving electron and a counter-moving electron in guiding center approximation and the full trajectory. 97
5.6. Maximum horizontal distance between the flux surface and the drift orbit evaluated in a poloidal plane for electron motion in TJ-K parallel and antiparallel to the magnetic field with constant $v_\perp/|\vec{v}|$. 98
5.7. Maximum horizontal distance between the drift surface and the flux surface in the $\phi = 0$ plane for variation of only one velocity component. 99
5.8. Probability of different speeds in 3D Maxwell-Boltzmann distributed gases with different thermal energies. 100
5.9. Effective electron-neutral scattering cross-section in He and Ar. 103
5.10. Contributions to the total toroidal net current in the poloidal plane of the ECE diagnostic for 10 eV and 100 eV. 108
5.11. Contributions to the total toroidal net current in the poloidal plane of the ECE diagnostic for 1 keV in Ar and He. 109
5.12. Toroidal net currents for velocity distributions with a 10 eV Maxwellian background and a fraction of superthermal electrons. 110

A.1. Frequency trend of the beam waist position compared to the antenna aperture. 118
A.2. Frequency trend of the beam waist width. 118
A.3. Measured phase shift of the Waveline 708c phase shifter. 119
A.4. Drawing of the antenna and the setup in the vacuum vessel in a poloidal cut. 120
A.5. Engineering drawing of the ECE mirror. 121
A.6. Drawing of the ECE mirror mount. 122

List of tables

3.1. Emission angles of the 8 GHz array antenna for different frequencies. 38
3.2. Comparison of different parameters concerning microwaves and ECE in TJ-K, WEGA, ASDEX Upgrade, Wendelstein 7-X and the Compact Helical System. 39

4.1. ECE harmonic frequencies in TJ-K and X-mode ECE strength for perpendicular observation normalized to the second harmonic. 42
4.2. Ratio of the signal contributions Q from the volume between antenna and inner wall compared to the entire torus for different frequencies and geometries with and without mirror. 59
4.3. Beam parameters as obtained from the antenna optimization and used in the full-wave simulations. 62
4.4. Main lobe power and width of the ECE antenna at different frequencies. 63
4.5. Insertion losses and reflection parameters of the resonator components. 84

5.1. Effective scattering cross-sections used for the calculation of the mean free path for electron trajectory simulations. 104
5.2. Collision times and mean free paths for different thermal energies in TJ-K for helium. 104
5.3. Collision times and mean free paths for different thermal energies in TJ-K for argon. . 105
5.4. Mean toroidal length of trajectories for given mean free paths and the resulting rounded fraction of toroidal turns for the simulations such that only outer ports are used. . . . 107
5.5. Toroidal net current from simulations for different Maxwellian velocity distributions and monoenergetic populations. 107
5.6. Toroidal net current from simulations for different Maxwellian velocity distributions and monoenergetic populations restricted to the confinement region. 109

A.1. Dimensions and cutoff frequencies of the rectangular waveguides types around the ECE frequency range of TJ-K with the naming according to the IEC (International Electrotechnical Commission) and the EIA (Electronic Industries Association). 117

Contents

Kurzfassung **3**

Abstract **5**

List of symbols **7**

List of figures **11**

List of tables **15**

1. Introduction and objective **19**

2. State of science and technology **23**

3. Setup of the stellarator TJ-K **27**

- 3.1. Coordinate systems 28
- 3.2. Shape of the vacuum vessel 28
- 3.3. Magnetic field 29
- 3.4. Employed TJ-K diagnostic systems 33
  - 3.4.1. Interferometer 33
  - 3.4.2. Optical diode and spectroscopy 34
  - 3.4.3. Langmuir probes 35
- 3.5. Microwave heating 37
- 3.6. Comparison to other experiments concerning electron cyclotron emission (ECE) 39

4. Design and test of an electron temperature diagnostic using ECE for TJ-K **41**

- 4.1. Electron cyclotron emission in TJ-K 41
  - 4.1.1. Electron cyclotron emission theory 41
  - 4.1.2. Numerical calculation of electron cyclotron emission radiation transport 46
- 4.2. Simulation of microwave propagation in the vacuum vessel 48
  - 4.2.1. Finite difference time domain method for Maxwell's equations 50
  - 4.2.2. Antenna reciprocity theorem 52
  - 4.2.3. Mapping of densities and temperatures 53
  - 4.2.4. 3D full-wave simulations for the ECE diagnostic at TJ-K 56
  - 4.2.5. Results of the full-wave simulations 57

4.3. Design of microwave components 60
    4.3.1. Optimization and characterization of an ECE antenna 60
    4.3.2. Optimization of an in-vessel mirror 64
    4.3.3. Design of a tunable resonator 67
4.4. Distinction from thermal bremsstrahlung 73
    4.4.1. Methods to identify the electron cyclotron emission 73
    4.4.2. Measurement results 75
4.5. Polarization of ECE 78
    4.5.1. Theory of depolarizing effects in TJ-K 78
    4.5.2. Estimation of the Faraday and Cotton-Mouton effect strengths in TJ-K 80
4.6. Measurement of electron temperatures from TJ-K plasmas 82
    4.6.1. Experimental setup 82
    4.6.2. Liquid nitrogen calibration 84
    4.6.3. Procedure of the measurements 86
    4.6.4. Resulting electron temperatures 86
4.7. Summary and discussion of the ECE measurements at optically thin plasmas 87

5. Simulation of electron drift orbits and toroidal net currents **91**
5.1. Theory of electron trajectory simulations 92
    5.1.1. The guiding center approximation 92
    5.1.2. Electron drift orbits in TJ-K 96
    5.1.3. Electron velocity distributions 100
    5.1.4. Relativistic effects 102
    5.1.5. Collisions 102
5.2. Simulation setup and procedure 105
5.3. Simulation results and calculation of toroidal net currents 106
    5.3.1. Toroidal net currents from superthermal electrons 110
5.4. Summary and discussion of the toroidal net current simulations 111

6. Summary and outlook **113**

A. Appendix **117**
A.1. Rectangular waveguide properties 117
A.2. Superposition of measurement signals 117
A.3. Antenna simulation results 118
A.4. 3D full-wave simulation hardware requirements 118
A.5. Phase shifter calibration 119
A.6. Drawings of the ECE diagnostic 119

Bibliography **123**

1 Introduction and objective

The diverse applications of plasmas include a variety of technological purposes [1] like etching, surface activation, coating, chemical reactions and medical purposes [2] like sterilization or plasma coagulation. Research in fusion plasma physics concentrates on the use of plasmas in the generation of electricity by the fusion of two light atomic nuclei. The fusion reaction with the highest reactivity is the fusion of deuterium and tritium into helium [3]:

$$^{2}_{1}\mathrm{H} \;+\; ^{3}_{1}\mathrm{H} \rightarrow \; ^{4}_{2}\mathrm{He}(3.5\,\mathrm{MeV}) \;+\; \mathrm{n}(14.1\,\mathrm{MeV}).$$

The deuterium-tritium-fusion as illustrated in figure 1.1 generates huge amounts of kinetic energy in the form of a fast helium ion and a fast neutron without directly generating radioactive waste with enormous decay times like in fission.

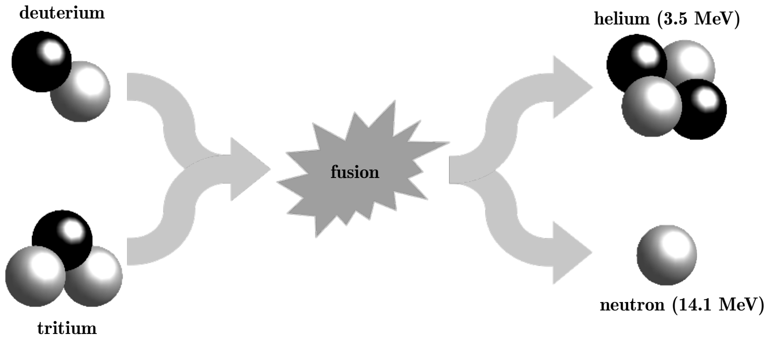

Figure 1.1.: Illustration of a deuterium-tritium fusion reaction.

The rate of fusion reactions depends on the ion density n_i, which determines the number of possible fusion partners, and the ion temperature T_i, which is of special interest since fusion reactions need a large temperature to provide for the activation energy of the reaction. Because a fusion reaction is the combination of two nuclei into one and nuclei are always positively charged, the Coulomb repulsion of nuclei is an opposing force. Assisted by the tunneling effect, not the entire barrier potential has to be delivered as kinetic energy but still large temperatures are needed to reach sufficient tunneling probabilities. Matter with sufficiently high temperatures is in the plasma state with high degrees of ionization. In order to realize a fusion power plant, high rates of fusion reactions are necessary to ensure that more energy is released than needed to sustain the plasma at high temperatures. The helium ion that is produced in a fusion reaction can be captured in a magnetic cage and its energy can be used to support the heating of the plasma through collisions. To deploy this heating efficiently, the energy confinement time τ_E in the plasma should be large. The neutron, however, has no electric charge. For this reason, it does not react to magnetic forces and can leave a magnetically confined

plasma. Its energy can be converted outside the plasma to generate electrical power.
The conditions for a fusion power plant require sufficient heating through the helium ions that leads to a self-sustained operation, called a burning plasma. This is possible when the three parameters ion density, ion temperature and energy confinement time fulfill the Lawson criterion [3]

$$n_i \tau_E k_B T_i \geq 5 \cdot 10^{24}\,\text{eV s m}^{-3},$$

with the Boltzmann constant k_B. Fusion of deuterium and tritium can be reached in toroidal vacuum vessels with magnetic fields that provide the confinement. The necessary confinement times are possible when the magnetic field forms closed surfaces with a constant magnetic flux on them, therefore called flux surfaces. On these flux surfaces, the charges are confined inside the vessel. A toroidal magnetic field but also a twist in the field lines by a poloidal component is needed for stable conditions since a purely toroidal field geometry gives rise to electric fields that generate outward charge transport [4]. The experimental concepts of stellarators and tokamaks realize such magnetic cages. A tokamak as shown in figure 1.2 generates the toroidal field using vertically aligned field coils that are distributed toroidally and are labeled "toroidal field coil" in the illustration.

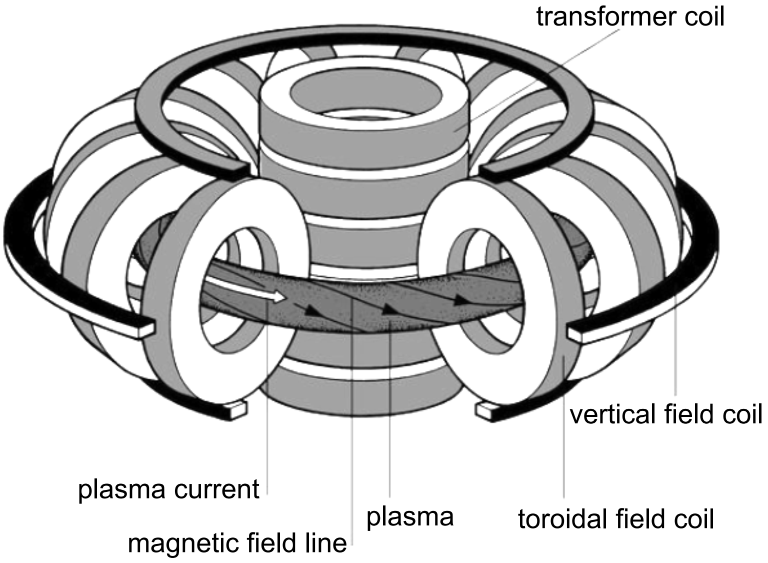

Figure 1.2.: Illustration of a tokamak setup, adapted from [5].

Another coil acts as the primary coil of a transformer using the plasma as the secondary coil giving rise to a toroidal current in the plasma that generates the poloidal field. These two field components add up to a helical field and a magnetic cage is generated that confines the plasma. Further vertical field coils are used to set the position of the plasma in the vessel.
A stellarator achieves the magnetic confinement with closed flux surfaces without a toroidal plasma current. Instead of a transformer coil, helical field coils generate the twist in the field lines from the outside. Therefore, no ramped current in a transformer coil is needed to induce a current in the plasma which makes the continuous operation of stellarators possible. In fusion reactor conditions a strong energetic coupling between electrons and ions leads to comparable electron and ion temperatures [4]. Therefore, the commonly used electron cyclotron resonance heating that in the first place heats up

the electrons, indirectly also heats the ions. Consequently, one of the main parameters of a plasma is its electron temperature as a factor to reach high ion temperatures and as the quantity that receives the heating power. Today most fusion-related plasma experiments are equipped with sophisticated diagnostic systems measuring electron temperatures from electron cyclotron emission (ECE) [6]. These diagnostics analyze the radiation that is emitted from the gyration of electrons around the magnetic field lines in a magnetically confined plasma like those of stellarators and tokamaks. The evaluation of the emission spectrum delivers time-resolved temperature profiles along the line of sight of the diagnostic and it can also be used to detect superthermal electrons [6,7]. In operation close to fusion parameters such non-invasive diagnostics can be employed in conditions that would harm temperature probes and hereby pollute the plasma. ECE diagnostics have proven a reliable source of temperature data as the results showed repeatedly good agreement with Thomson scattering measurements [8,9] and ECE is even used as a reference diagnostic for temperature measurements using Thomson scattering [10].

Without an ECE diagnostic at TJ-K, electron temperatures were routinely measured using Langmuir probes (see section 3.4.3). This allows for localized time-resolved measurements at the tip of the probe. Temperature profiles can be retrieved by simultaneously using spatially separated probes in the plasma or by moving a single probe. The measurement of a time-resolved temperature profile by means of the analysis of an ECE frequency spectrum has the advantages of having no components in the plasma and no moving parts. An optical diode (section 3.4.2) can also be used to gain information about the electron temperature. The setup at TJ-K images the optical emission of the plasma to one diode. Thus there is no spatial information contained and only volume integrated data is available. The same argument applies to the occasional UV-VIS spectroscopy measurements that can also indicate electron temperatures as described in section 3.4.2. An ECE diagnostic system combines the advantages of Langmuir probe measurements and of the optical temperature diagnostics available at TJ-K, namely localized measurements of non-invasive nature.

In addition to temperature measurements, ECE diagnostics show distinct changes in the emission spectrum when the velocity distribution of the electrons in the plasma is not purely Maxwellian but contains a superthermal contribution [6, 7, 11]. The trajectories of such superthermal electrons lie on drift orbits. The examination of their contribution to previously observed toroidal net currents [12,13] constitutes a further motivation of the usage of an ECE diagnostic for TJ-K. The objectives of this work are therefore:

- to design, build and use an ECE diagnostic for the optically thin plasmas of TJ-K for temperature measurements, and,
- to investigate numerically the toroidal net currents that are possible from superthermal electrons in TJ-K.

The structure of this thesis is as follows (compare figure 1.3): at first, the current state of science and technology is sketched in chapter 2 and the properties of the stellarator TJ-K that are important for ECE measurements and toroidal net currents are presented in chapter 3. The electron temperature measurements and the detection of superthermal electrons are connected as the capabilities of ECE diagnostics. They thus form the two main parts, chapter 4 and 5, of this thesis. Finally, chapter 6 summarizes the outcome of ECE investigations at TJ-K and adds some ideas for further research.

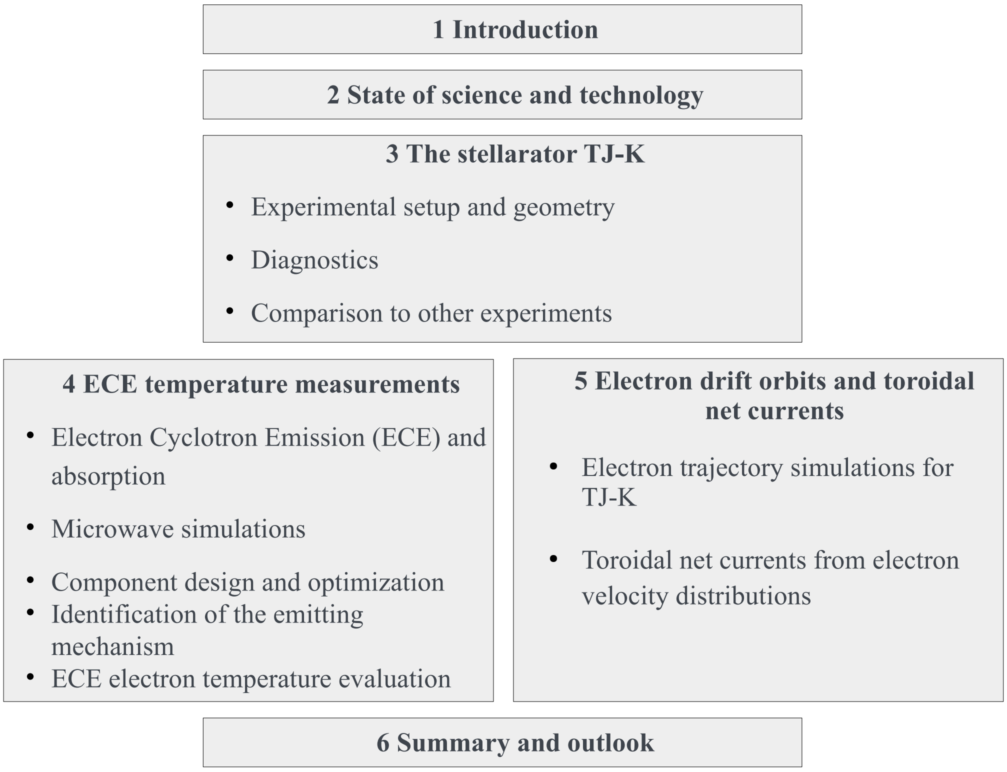
1 Introduction
2 State of science and technology
3 The stellarator TJ-K
Experimental setup and geometry
Diagnostics
Comparison to other experiments
4 ECE temperature measurements
Electron Cyclotron Emission (ECE) and absorption
Microwave simulations
Component design and optimization
Identification of the emitting mechanism
ECE electron temperature evaluation
5 Electron drift orbits and toroidal net currents
Electron trajectory simulations for TJ-K
Toroidal net currents from electron velocity distributions
6 Summary and outlook

Figure 1.3.: Diagram of the thesis structure.

2 State of science and technology

Diagnostics measuring the ECE are widespread in magnetic confinement fusion research because of their benefits and the few requirements: only optical access to a magnetically confined plasma, preferentially with a monotonous magnetic field gradient, is needed. Due to the wide range use, ECE diagnostics are adapted to many different conditions but are mainly used in toroidal devices for temperature profile measurements and to perceive superthermal electrons. In addition, they can be used for density profile measurements [14], temperature fluctuation measurements, drift wave studies [15] or to measure the direction of the magnetic field [6, 16]. Extensions to measure temperatures in two dimensions, called ECE imaging, are under current development and require further theoretical explanation [6]. Typically, the ECE diagnostic is composed of a highly-directive antenna at the outer side of the device (the low-field side, LFS, where the magnetic field strength is small) that collects the microwaves, a set of bandpass filters that split the signal into separate channels, amplifiers and semiconductor detectors [9, 17–19]. There are also setups using interferometers [8] or scanning heterodyne semiconductor receivers [20] for the spectral analysis. The frequency in the spectrum corresponds to a spatial region in the plasma, determined by the local magnetic field strength, and the detected power can be related to the radiation temperature. Together, this information is then used to obtain the temperature profile along the line of sight. Observation of the emission is regularly performed at harmonics of the X-mode [16, 21] where the polarization of the ECE is perpendicular to the background magnetic field as this is the dominant emission polarization [22]. Equipment for power detection and spectral analysis was already well developed in the 1980s [16] while especially for small experiments the design of an antenna with a suitable directivity is a challenge. Because knowing the ECE's path is essential for the interpretation of the radiation transport [16], ray tracing simulations with program packages like TRAVIS [23], ECRad[1] [24], TRECE [25], RAYS [26] or many more are used to translate the radiation intensities to electron temperatures and, finally, to a temperature profile. When the power received by the antenna is not only due to ECE propagating directly from the plasma to the antenna, a plain mirror approach is used to model the ECE path including reflections at the vessel wall. Such models can be either described by a geometrical series [21, 24, 27–29] or are simply solved in the ray tracing simulations with only a few passes of the line of sight through the plasma [23]. In small vessels like in TJ-K, the walls are strongly curved compared to the beam size of the antenna and wavelength of the ECE such that the plane mirror approximation is not valid. In such cases, a beam dump opposite the antenna is considered essential to use optically thin harmonics [21] but microwave absorbers then need to cope with the microwave heating power or have to be shielded against it. Furthermore, beam dumps have been ascertained as not completely effective [6]. Another option for small devices with optically thin plasmas is the use of a curvature-optimizing mirror at the inner wall. In the literature, no realization of such a mirror was found and this work describes the first investigations of such a mirror, installed in the small-scale stellarator TJ-K.

---

[1] working title, name unpublished.

The system is commonly calibrated using a black body radiation source at two different temperatures (hot-cold method) [6, 16, 18, 28, 30] but also calibrated emitters or calibrated power meters can be used [6]. In many cases, the waveguide can be switched to the calibration source by use of a mirror [8,28,31] for in-situ calibration. Accessibility and moderate dimensions of the diagnostic at TJ-K allow for a calibration detached from the vessel. For ITER it is planned [32] and in other experiments it is routine [16, 21, 30] to use a rotating mirror (chopper) that periodically switches between a hot and a liquid nitrogen (LN2) cooled reference but also continuous measurements of the reference sources are common in radiometer calibration [33].

Often the plasmas are optically thick which has the advantage that the intensity of the ECE is then independent of parameters other than the electron temperature, like the electron density [34]. But even in optically thin plasmas, the electron temperatures are normally obtained from a linear dependence on the radiation intensity of the second or higher ECE harmonics [21,28]. For this analysis, the optical depth τ needs to be in the vicinity of 1. Typical values for the optical depth in thin cases are of the order of 0.2 [21] or 0.5 [28]. ECE measurements at the stellarator WEGA [18] operated with an extremely low measured optical depth of about $8 \cdot 10^{-3}$ and the expected optical depth for the diagnostic at TJ-K is extraordinarily low at $2 \cdot 10^{-3}$.

High-temperature plasmas show strong ECE from several harmonics. When these harmonics have a frequency overlap an evaluation of the temperature is very problematic and therefore the profile measurements are restricted to the regions without harmonic overlap which for example costs half of the radial profiles in JET [16], the largest tokamak in the world. Also for future experiments and fusion power plants the overlap is a subject of current investigations as higher temperatures increase the overlap due to strong relativistic broadening [6]. In optically thin measurements this problem is not present as then the higher harmonics emit only insignificant power. Instead, optically thin plasmas come with the difficulty that multiple complicated reflections of the microwaves in the vessel occur because the plasma is thin enough that the diagnostic sees through it. Furthermore, the contribution from a population of superthermal electrons to the measurement signals is in thin plasmas too strong to allow for density measurements [16]. When the optical depth is only moderately low, the electron temperature is obtained from the knowledge of the optical depth. Transmission measurements with a highly-directive emitter at the high-field side and an equally directive ECE antenna can be used to measure τ and make temperature and density measurements possible [16,18]. Because of the extraordinarily low optical depth in TJ-K, the nature of radiation transport is investigated prior to using models for typical ECE diagnostics. By comparison of the emission in X-mode and O-mode, where the polarization is parallel to the background magnetic field, the direction of the magnetic field can be probed only in devices without polarization scrambling that occurs from multiple reflections [22,22,35] in optically thin plasmas or from the plasma itself. Only in high-temperature plasmas, these problems can be avoided by using higher harmonics as they react less to the plasma and are simultaneously strong enough for measurements [16].

Additional to temperature measurements, ECE diagnostics are often used to gain evidence of superthermal electrons. A quantitative understanding of their impact on ECE signals is only possible when they appear with a low percentage [16]. Superthermal electrons lead to an intense broadband emission that has a more intense impact in the case of an optically thin plasma such that smaller deviations in the velocity distribution are visible [6, 7]. As soon as the velocity distribution is not Maxwellian, neither a temperature is defined nor the emission theory based on Kirchoff's laws may be applied [36] and therefore the strong reaction to superthermal electrons in optically thin plasmas is beneficial for recognizing the operating regimes: non-Maxwellian velocity distributions are easy to identify.

In addition to the development of ECE diagnostics, current research also further investigates aspects of the cyclotron emission itself, like its contribution to the power loss of fusion plasmas [6].

Toroidal net currents were found using Rogowski coil [37, 38] measurements both in TJ-K [12, 13] and the WEGA stellarator where their existence was explained from drift orbit effects of superthermal electrons [39]. This connection is picked up and investigated in simulations of electron trajectories with the parameters and geometry of TJ-K. The equation of motion for the guiding center of even relativistic electrons is theoretically discussed for drift orbits in nested flux surfaces [40, 41]. The generation of superthermal electrons in WEGA was explained by electrons being accelerated by the wave field in front of the antenna of the microwave heating [39, 42].

3 Setup of the stellarator TJ-K

Plasmas for fusion-related research are often generated in toroidal experiments with magnetic field coils. The magnetic fields generated from electric currents in the coils are capable of the deflection of electric charges, like the electrons and ions in a plasma, without contact. Sophisticated setups allow for magnetic field structures that keep the plasma confined in a vessel without the plasma colliding with the vessel wall. This is achieved by the formation of magnetic flux surfaces, 3D surfaces with cross-sections through which the magnetic flux is constant. The electrons and ions in a plasma are confined on these flux surfaces but the charges can move along the field lines on them. Therefore, it is convenient to bend the flux surfaces toroidally together such that closed nested surfaces are formed.
Mainly two basic concepts of toroidal magnetic confinement setups are used: the tokamak and the stellarator (see also section 1). The main experimental setup that is used during this work is a stellarator called TJ-K that is located at the Institut für Grenzflächenverfahrenstechnik und Plasmatechnologie (IGVP) in Stuttgart after it was first put into operation in Madrid and later transferred to Kiel.
A helically twisted field coil around the torus generates the toroidal (along ϕ in figure 3.1) and the poloidal (perpendicular to ϕ) magnetic field components simultaneously.

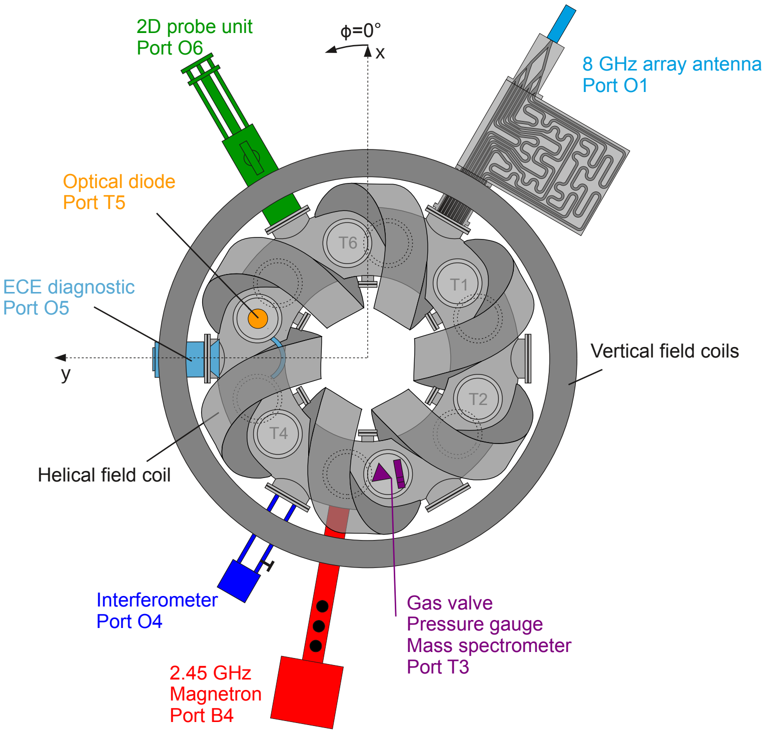
2D probe unit
Port O6
ϕ=0°
x
8 GHz array antenna
Port O1
Optical diode
Port T5
T6
T1
ECE diagnostic
Port O5
y
Vertical field coils
T2
T4
Helical field coil
Interferometer
Port O4
Gas valve
Pressure gauge
Mass spectrometer
Port T3
2.45 GHz
Magnetron
Port B4

Figure 3.1.: Schematic top view of TJ-K with the diagnostics used for ECE measurements, indication of the port numbering and definition of the x- and y-axis and the toroidal angle ϕ. The z-axis points out of the plane.

In order to compensate for the vertical contribution in the magnetic field that is also generated by the helical field coil, another set of vertical field coils is employed. In total, this setup generates magnetic field lines that form nested magnetic flux surfaces that are capable of confining a plasma.
In the case of TJ-K, which is shown in a top view in figure 3.1, the helical coil winds six times evenly around the toroidal vessel. This leads to a six-fold symmetry of the magnetic field structure. The toroidal vacuum vessel of TJ-K has four port types and six toroidally evenly distributed ports of each type. At each port of the same type, the geometry of the magnetic field and the plasma is the same. The different port types, top, bottom, inner and outer port, are at completely different geometries. The numerous ports are used for heating, the vacuum pump and offer easy access for various diagnostics.
In the following sections, the coordinate systems that are employed are described and then used to provide details about the vessel, the plasma and the magnetic geometry of TJ-K.

3.1 Coordinate systems

Points in a toroidal system can be referenced in a variety of coordinate systems. A Cartesian coordinate system with orthogonal axes x, y and z is used with the axes chosen in a right-handed system with the vertical z-axis pointing upwards and the x-axis pointing from the torus center through the first inner port I1 (see figure 3.1).
Often it is helpful to reference a point in a poloidal plane. Two systems are useful that are both illustrated in figure 3.2.

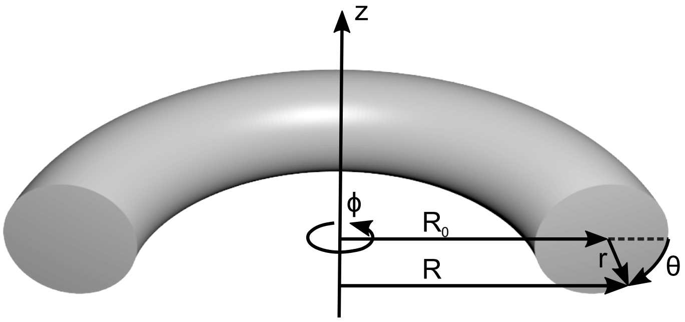

Figure 3.2.: Vertical cut through a schematic torus showing two poloidal cross-sections with the poloidal angle θ, the poloidal radius r, the large radius R, the major torus radius R_0, the vertical coordinate z and the toroidal angle ϕ being indicated.

Since a poloidal plane is defined by the toroidal angle ϕ, counted from port I1 counter-clockwise from a top view, two spatial coordinates remain to be defined. One way is to specify the vertical coordinate z in this plane and the coordinate R along the major radius.
Another option is to use a polar system in the poloidal plane that has its origin in the center of the circular poloidal cross-section. The polar angle θ is counted from the outboard side clockwise and the distance from the poloidal center is called r.

3.2 Shape of the vacuum vessel

TJ-K is a medium-sized stellarator with a toroidal vacuum vessel made out of stainless steel 316L. The major torus radius R_0 is 60 cm and the minor radius r_0 is 17.5 cm. There are four types of cylindrical ports to access the vessel: bottom (B), top (T) and outer (O) ports have a diameter of 250 mm while the inner ports (I) are smaller due to the lack of space between the windings of the helical field coil towards the torus center. Inner ports have a diameter of only 63 mm. As visible in figure 3.1 the coordinate systems are chosen such, that the x-axis and $\phi = 0°$ go through the inner port 1 (I1) and the y-axis through port O5. Every 60° the next port of the same type can be found, up to port number 6. For historical reasons, the port numbering is clock-wise, therefore the outer port O1 is located at 330°, the top port T1 at 310° and the bottom port B1 at 350°. The ports are used for diagnostics, heating systems and the vacuum pump while unused ports are either closed with metal blank flanges or windows. With the different use of ports and the flexibility of the setup of TJ-K the exact vessel shape as it is experienced by microwaves propagating in the vessel is complex and changing from experiment to experiment. The shape of the flux surfaces is in contrast not sensitive on a change from a blank flange to a window or the addition of a port extension. Therefore, the shape of the confined plasma is not influenced by such changes. Due to the toroidal shape, from the inside, the vessel wall has a convex-concave curvature at the central column and a concave-concave curvature towards large R as illustrated in figure 3.3.

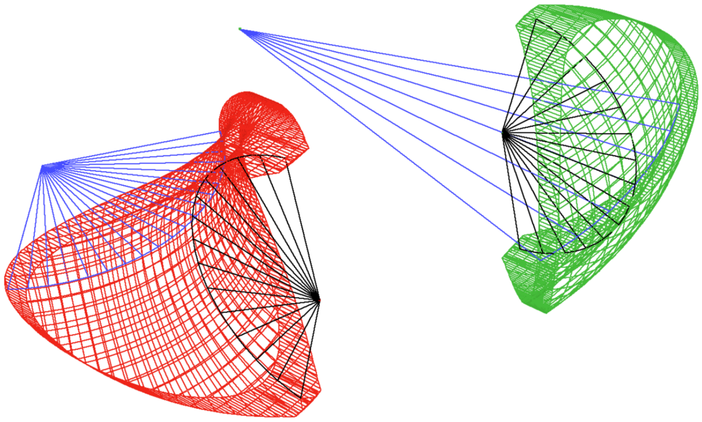

Figure 3.3.: Perspective illustration of the vessel curvatures. The red vessel section (left) shows the curvature at the inner column and the green (right) section shows the curvature at the outer wall. Rays indicate the curvature vectors in the vertical (black) and horizontal (blue) plane: the poloidal center (black) and the toroidal center (blue).

In the concave-concave case (green and right in figure 3.3) as it occurs at the outboard side in the vacuum vessel (low-field side), both the horizontal and vertical curvature centers are located at the same side of the surface: towards the torus center. For the surface at the high-field side (red, left) the horizontal curvature center at the torus center is behind the vessel wall but the vertical curvature center, the center of the poloidal plane, is in front of it in the vacuum chamber. The effects of different curvatures of the vessel wall for the ECE diagnostic are discussed in section 4.3.2.

3.3 Magnetic field

The coil system of TJ-K is fed from a high current supply with the currents that are needed to generate the magnetic field for the confinement of the plasma. A total magnetic field strength of $B_{ax} \approx 0.27\,\mathrm{T}$ on the magnetic axis, the center of the nested flux surfaces, is used in this work. This magnetic field is reached with about 1140 A nominal current from the power supply at approximately 400 V. The current is then distributed to the helical and the vertical field coils with a tunable current ratio r_{vh}. For standard operation, a current ratio of 57 % is used at TJ-K, which is the only ratio for all measurements and simulations in this work. The choice of the current ratio determines the radial position and shape of the flux surfaces formed by the magnetic field. Those are the tube-like 3D surfaces, shown in red in figure 3.4, with cross-sections of constant magnetic flux. Their shape is essential for the plasma since they define the behavior of charge motion in it.

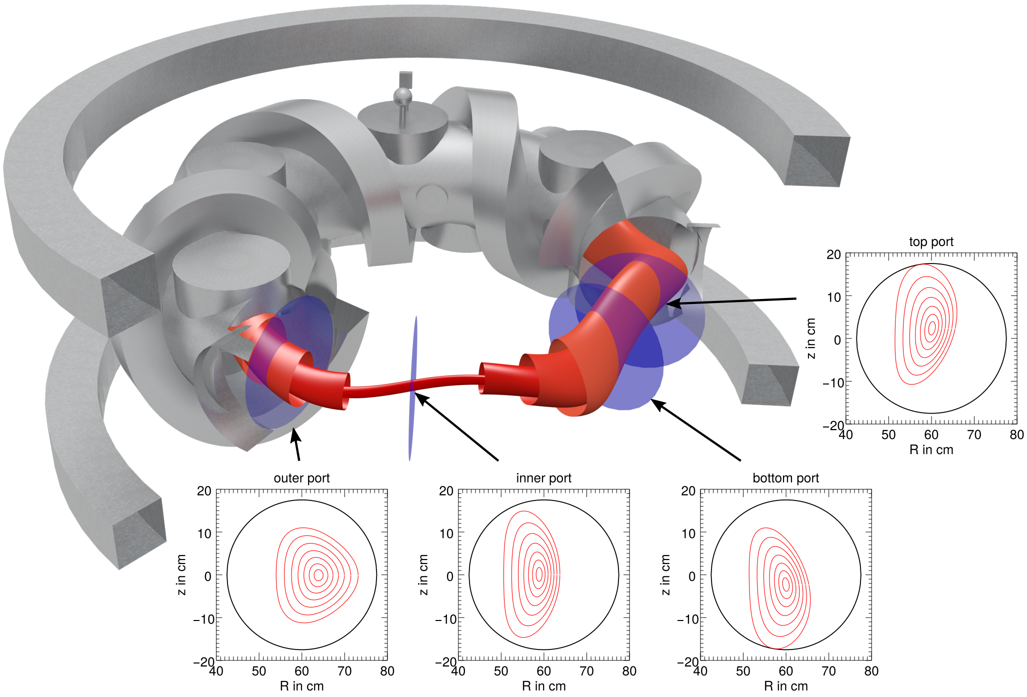

Figure 3.4.: Scheme of TJ-K with a cut-out. The vessel and coils are shown in gray and flux surfaces are indicated, also with a cut-out, in red. At the blue discs, poloidal cross-sections of the flux surfaces are plotted. The positions of the discs correspond to the different port types.

The flux surfaces do not have an exact toroidal shape but show extrusions away from the coils towards the ports. Therefore, the magnetic axis moves downwards when the position is followed from a top port past an outer port towards a bottom port. The magnetic field line at the center of the plasma and the center of the major diagnostic port type discussed here, the outer port, is tilted by about 14.3° with respect to the horizon. Simultaneously, a twist of the magnetic field lines is needed like in the tokamak configuration shown in figure 1.2. Therefore, the orientation of the magnetic field vectors varies systematically but in various directions. In a cylindrical volume from the outer port towards the inner wall, the direction of the magnetic field has a root mean squared variation of about 8.2°. Due to the Lorentz force

$$\vec{F}_L = -e\vec{v} \times \vec{B},$$

that acts perpendicular to the magnetic field $\vec{B}$ and the velocity $\vec{v}$ when an electron with charge $-e$ moves in a magnetic field, the movement perpendicular to the field lines is limited to the resulting circular motion, the gyration. Gyroradius and Larmor radius are both used in the literature as terms for the radius of the circular motion in the plane perpendicular to the magnetic field. Parallel to the field line, the Lorentz force has no influence, leading to free motion with high mobility in this direction while the motion from one to another flux surface is limited by the gyration. The high mobility of charges parallel to the field lines results in efficient equilibration of density and temperature on flux surfaces. Thus, density and temperature can be considered constant on flux surfaces as a first approximation [4]. Still, fluctuations and perturbations on the flux surfaces are possible. The flux surfaces in a stellarator have a complex shape with changing cross-section shapes and centers along the toroidal angle. With a constant density on the flux surfaces, the vertical cuts in figure 3.4 that are called poloidal cross-sections also show the 2D structure of the density and temperature profile in the confinement region for the four port types. How the density and temperature vary from flux surface to flux surface can be determined with 1D measurements as it is done in section 4.2.3. Bottom and top ports, therefore, have an asymmetric density structure for a diagnostic's perspective viewing from below or above, respectively. At inner and outer ports the density is much closer to symmetric. Refractive effects of the plasma on microwave diagnostics at these ports are therefore less complicated. The absolute value of the magnetic field in a poloidal cross-section at an outer port is shown in figure 3.5. In this plane, the field strength is close to up-down symmetric with respect to the R-axis and the lines of equal strength are only slightly curved. The toroidal component of the magnetic field dominates and is orientated in the same direction as ϕ.

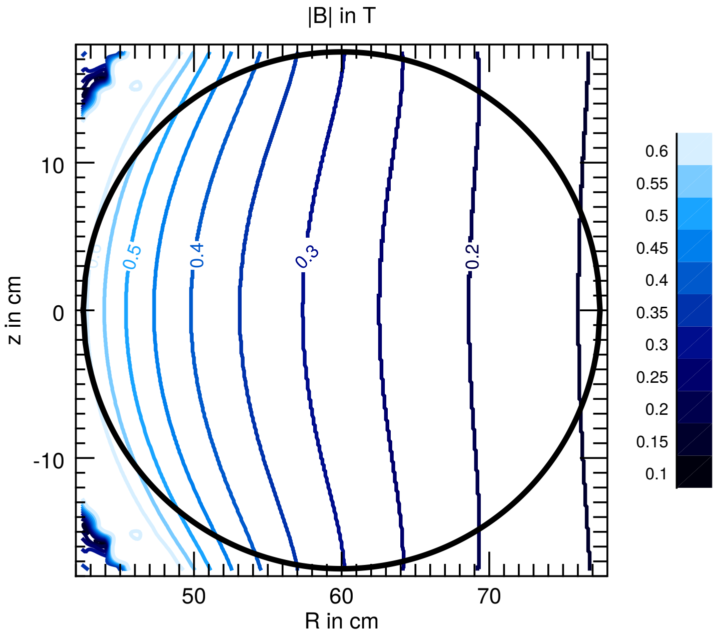

Figure 3.5.: Absolute value of the magnetic field for a current of 1140 A and a current ratio of 57 % in the poloidal plane of an outer port. The vessel is indicated as a black circle.

The radial change of the absolute field at $z = 0\,\mathrm{m}$ can be approximated in the confinement region by a $1/R$ dependence as shown in figure 3.6. If also the region outside the plasma is needed, a combination of two exponential decay functions is appropriate but adds complexity to the description and is not needed in this thesis. The derivative of the absolute magnetic field with respect to the major radius is also described accurately by this regression as can be seen on the right side in the figure. The resulting gradient length L_B in the confinement region is

$$L_B := \frac{|\vec{B}|}{\frac{\mathrm{d}|\vec{B}|}{\mathrm{d}R}} = -(0.27 \pm 0.02)\,\mathrm{m}, \tag{3.1}$$

which is independent of the coil current as long as the current ratio is kept at 57 % because the magnetic field strengths and its gradient both are proportional to the coil current.

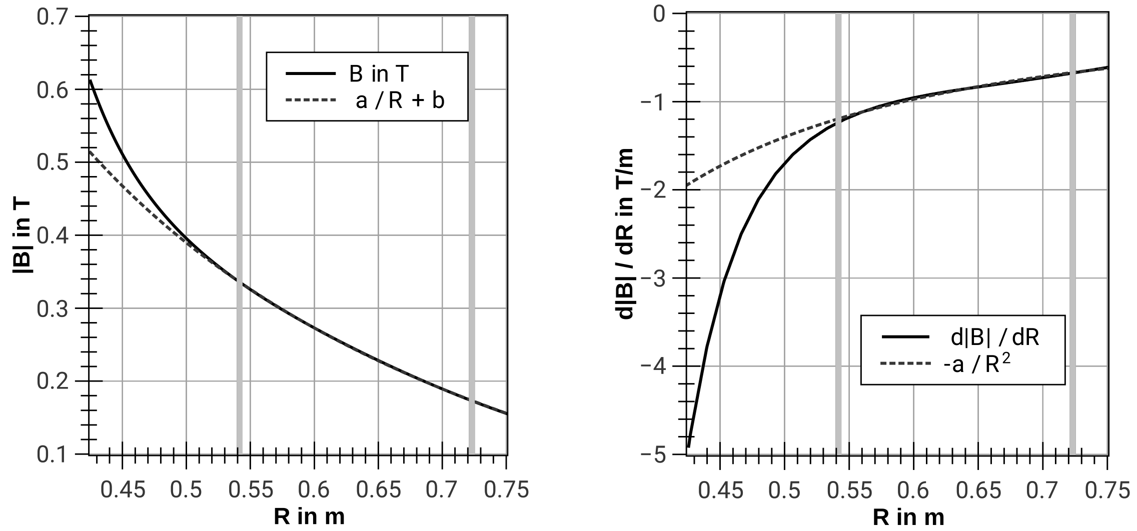

Figure 3.6.: Absolute value of the magnetic field and its gradient along the major radius at z=0 for the outer port O5. The dotted lines show regression curves with $a \approx 0.350\,\mathrm{T/m}$ and $b \approx -0.311\,\mathrm{T}$. Within the limits of the confinement region (thick gray vertical lines) there is a good agreement between the regression and the numerically calculated values.

Together with the large port diameter and the symmetry with respect to the R-axis, the outer ports are the best choice for an ECE diagnostic at TJ-K.

When a poloidal cross-section is analyzed, the changing shape and center along ϕ determine the required accuracy in the toroidal angle. To convey an impression of the sensitivity, figure 3.7 shows to what extent the toroidal angle changes the vertical position of the upper turning point and the horizontal position of the outer turning point of a cross-section of the same flux surface around the outer port O5 at $\phi = 90°$.

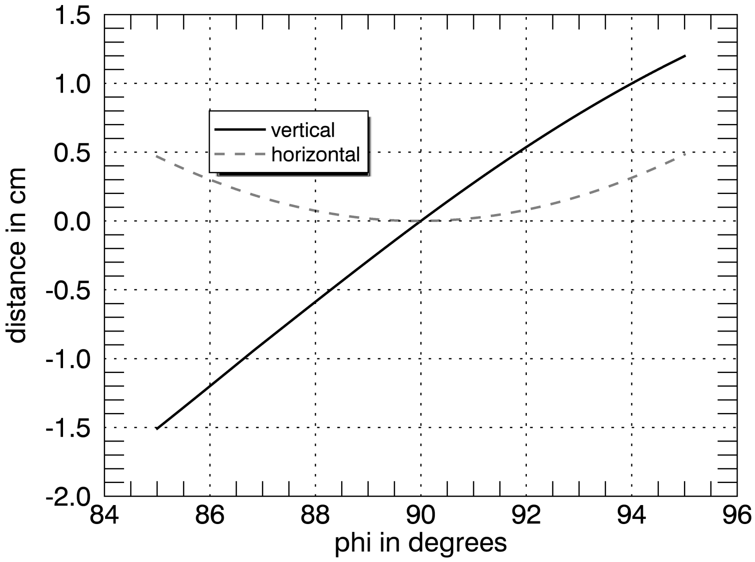

Figure 3.7.: Vertical shift of the upper turning point and horizontal shift the outer turning point of a flux surface compared to the flux surface at $\phi = 90°$ (port O5).

The vertical shift is stronger than the horizontal shift in the direction of the major radius. The required accuracy of simulations and of the adjustment of experimental setups can be derived from these plots: for angular uncertainties of $6 \cdot 10^{-2}$ degrees that appear in the electron trajectory simulations with step sizes of $5 \cdot 10^{-4}$ m in chapter 5, the shifts are both below 0.17 mm. A difference of one degree already leads to vertical shifts of about 3 mm.

All the previous descriptions apply to perfectly aligned magnetic field coils at TJ-K but a slight misalignment of the order of few millimeters of the field coils was found comparing experiments and simulations [43]. For more realistic results, simulations use the magnetic field configuration with the slightly modified field geometry unless the ideal symmetry is needed. The use of the idealized coil geometry is then indicated. Without idealization, the geometry is not exactly six-fold symmetric but the simulations are closer to experimental conditions.

3.4 Employed TJ-K diagnostic systems

3.4.1 Interferometer

A standard microwave diagnostic is an interferometer which delivers information about the integrated electron density along its line of sight. This diagnostic is a first example of the propagation of electromagnetic waves in a plasma. A microwave is split into a probing wave that is led through the plasma and a reference wave without plasma contact. From the phase difference of the probing wave and the reference wave, the line-averaged electron density of the plasma can be calculated. In this section, the case without an influence of the background magnetic field is described which can be applied to the interferometer at TJ-K [44] as it works with a wave predominantly in O-mode where this influence is negligible. The refractive index N and therefore also the phase speed v_{ph} of the electromagnetic wave are like in the case without background field. The phase speed of a wave with angular frequency ω in a plasma with electron density n_e is given by [4]

$$v_{ph} = \frac{c}{N} = \frac{c}{\sqrt{1 - \frac{\omega_{pe}^2}{\omega^2}}}, \tag{3.2}$$

with the vacuum speed of light c, the electron plasma frequency $\omega_{pe} = \sqrt{\frac{n_e e^2}{\varepsilon_0 m_e}}$, the electron rest mass m_e, elementary charge e and the electric field constant ε_0. The phase speed is larger than c, hence a phase difference $\Delta\varphi$ occurs even if the paths of the reference wave and the probing wave are equally long. The time that a phase front needs to pass the plasma $t_1 = L/v_{ph}$ is therefore shorter than for propagation of the same length L in vacuum $t_0 = L/c$. Since the frequency stays constant, the probing wave and the reference wave would reach the point behind the plasma with the phase difference

$$\Delta\varphi = \omega \cdot (t_0 - t_1) \, . \tag{3.3}$$

The combination of equations (3.2) and (3.3) results in

$$\Delta\varphi = \frac{\omega L}{c} \left(1 - \sqrt{1 - \frac{\omega_{pe}^2}{\omega^2}} \right) . \tag{3.4}$$

As the interferometer frequency needs to be far above the plasma frequency in order to penetrate the plasma, the square root can be written as a second order Taylor series around $\frac{\omega_{pe}^2}{\omega^2} = 0$:

$$\sqrt{1 - \frac{\omega_{pe}^2}{\omega^2}} \approx 1 - \frac{1}{2}\frac{\omega_{pe}^2}{\omega^2}.$$

The resulting phase difference is

$$\Delta\varphi \approx \frac{L}{2c\omega} \cdot \frac{n_e e^2}{\varepsilon_0 m_e}. \tag{3.5}$$

The electron density of the plasma was assumed to be constant. In reality, the plasma has a density gradient, which is accounted for by integration, leading to the diagnosis of the line-averaged density $\bar{n}_e$. From the phase difference of the two waves the line-averaged density can then be calculated as

$$\bar{n}_e := \int_0^L n_e \frac{\mathrm{d}s}{L} = \frac{2c\omega\varepsilon_0 m_e}{e^2 L}\Delta\varphi. \tag{3.6}$$

Since in practice the paths are not equally long, the change of the phase difference from the state without plasma to the state with plasma is evaluated.

At TJ-K the interferometer operates at 64 GHz. The probing wave is reflected at a mirror which is mounted at the inner vessel wall. In this setup, it has to be accounted for the probing wave passing the plasma twice on its way, to the mirror and again on its way back. The absolute phase shift caused by the plasma can then be obtained by comparison of the interferometer signal during the plasma discharge to the signal without plasma. The high frequency of the wave and the fast electronic components allow for measurements of the line-integrated density with a time resolution of about $10\,\mu$s. Therefore, also line-averaged density fluctuations or the evolution of the density during the extinction of a plasma can be measured. With this setup, a line-averaged density of up to $1.4 \cdot 10^{18}\,\mathrm{m}^{-3}$ can be detected within the phase difference range from 0 to 2π. Larger densities can be detected by counting the fringe jumps when a phase shift of 2π is reached [45].

3.4.2 Optical diode and spectroscopy

Atomic and ionic transitions in the plasma are excited by collisions with electrons, neutrals and ions. The resulting emission from the relaxation of the atoms is in the visible and near UV wavelength regime. Both, the overall intensity in the visible range and the intensity of specific lines can be used to obtain information about the electron temperature.

The optical diode that is installed at top port T5 of TJ-K is a Siemens BPX 61 Si PIN diode. It detects wavelengths in the range from 400 nm to 1100 nm with a broad FWHM angular sensitivity of 110°. Like in a photovoltaic cell, incoming photons generate charges which form a current that is over a wide range proportional to the incoming intensity.

Emission from TJ-K plasmas in the optical range is mainly generated by relaxation of ions and neutrals that are excited through collisions with electrons [46]. Figure 3.8 shows for the typical thermal energies of TJ-K that the intensity in the optical range depends strongly on the thermal energy of the plasma. The emitted intensity monotonously increases with higher plasma temperatures. This relation can be used inversely when the density is constant and no stray signals are present. Therefore, the signal from the optical diode indicates the electron temperature of a plasma in thermodynamic equilibrium.

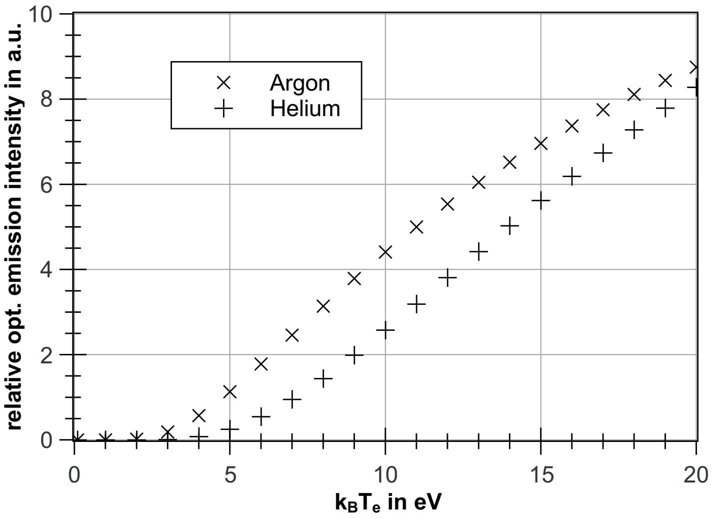

Figure 3.8.: Relative emitted intensity of the main spectral lines of a helium and an argon plasma for different thermal energies based on data from the NIST ASD [47].

The diode is shielded from ambient light and a metal mesh is fixed on the vacuum window that prevents microwaves from sources like the heating system or the plasma itself from passing. Plasmas with $k_BT_e < 4\,\mathrm{eV}$ emit only very low intensities with a comparatively flat temperature dependence. Therefore, temperature investigations in this range would require a highly sensitive diagnostic.

The field of view and wavelength integration of the optical diode result in a signal that indicates the average, density-weighted electron temperature. No spatial resolution is available and absolute temperatures are not provided directly but the time resolution is excellent. Dominated by the amplifier reaction time, time resolutions down to $12\,\mu\mathrm{s}$ are available with the current amplifier setup.

Measurements with a spectrometer additionally contain information about the wavelength of the emission. By evaluation of the relative intensities of two spectral lines, a and b, of the same ion the electron temperature of a plasma in local thermodynamic equilibrium can be derived [48, 49]:

$$T_e = \frac{E_a - E_b}{k_B \cdot \ln\left(\frac{A_b g_b f_b I_a}{A_a g_a f_a I_b}\right)}, \tag{3.7}$$

where k_B is the Boltzmann constant, $E_{a,b}$ are the excitation energies of line a and b, $A_{a,b}$ the transition probabilities, $g_{a,b}$ the statistical weight of the lines, $f_{a,b}$ the frequencies and $I_{a,b}$ the measured intensities. All but the measured line intensities is available from databases like the NIST Atomic Spectra Database (ASD) [47]. Spectroscopic measurements can be used to obtain temperature profiles when sufficient spatial information is acquired and Abel inversion, see e.g. [50], or a similar technique for more complex geometries, is used. The time resolution of temperature profiles is limited by the scanning speed, both in wavelength and space. At TJ-K, spectrometric measurements are only used in dedicated experiments and without spatial resolution or high temporal resolution with no permanent setup [46, 51–53].

3.4.3 Langmuir probes

Langmuir probes are currently the standard diagnostic for temperature measurements at TJ-K. The probes consist of an electrically insulating tube with a wire within. At the tip of the probe, the wire protrudes into the plasma. This works as an electrode with electrical contact to the plasma while the rest of the wire is electrically insulated from the plasma. Outside the vacuum vessel the wire is connected to a voltage generator and data acquisition such that either current-voltage characteristics, the floating potential Φ_{fl} with no external voltage U or the electron or ion saturation currents, $I_{e,sat}$ and $I_{i,sat}$, with sufficiently high fixed external voltage can be recorded. A typical current-voltage characteristic is shown in figure 3.9.

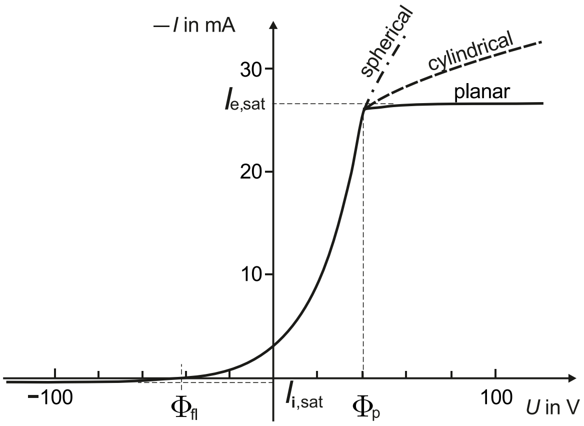

Figure 3.9.: Current-voltage characteristic of a Langmuir probe, adapted from [54].

In the plasmas of TJ-K, the ion temperature is lower than the electron temperature ($T_i < T_e$) and the ion and electron densities are approximately equal ($n_i \approx n_e$) because the plasmas are largely singly ionized. Then the number of electrons that reach an unbiased electrode in the plasma over time is larger than the number of ions, caused by the higher thermal velocity of the electrons. Thus, the Langmuir probe charges up negatively leading to a negative floating potential Φ_{fl}. The arising electric field between probe and plasma governs the charge flux to the probe surface A_{probe} and a Debye sheath forms that shields the probe from the bulk plasma. When an external potential below the plasma potential Φ_p is applied to the probe, electrons from the sheath are repelled and ions are attracted. This leads to an ion current to the probe. Saturation of this current appears for more negative voltages since the ion flux from the plasma to the sheath is limited. In the case of cold ions, a pre-sheath forms and the ion sound speed limits the ion supply. Finally, the ion saturation current [55]

$$I_{i,sat} \approx 0.6 e n_i \sqrt{\frac{k_B T_e}{m_i}} A_{probe}, \tag{3.8}$$

can be drawn from the plasma. In the case of a cylindrical probe, the ion current does not strictly saturate since the bias voltage increases the sheath size [56]. As there is also no ideal saturation of the ion current in TJ-K measurements, the current at the fixed voltage of $U = -99\,\mathrm{V}$ is used in this work to obtain relative densities that can be used to measure the profile shape. Absolute density profiles are obtained by acquisition at several positions and normalization with the line-averaged density that is obtained from the interferometer. Due to the approximate equality of ion and electron density, the ion saturation current provides the electron density via equation (3.8) when the electron temperature is known. The inverse ion plasma frequency determines the time resolution of ion saturation current measurements [57] which is of the order of $10^{-8}\,\mathrm{s}$ at TJ-K.

In order to retrieve the electron temperature T_e from Langmuir probes, the characteristic is needed. Voltages higher than the floating potential attract electrons and repel ions leading to a negative current, that evolves exponentially,

$$I_e(U) = I_{e,sat} \cdot \exp\left(\frac{e(\Phi_p - U)}{k_B T_e}\right), \tag{3.9}$$

until this current also saturates at the electron saturation current $I_{e,sat}$, following the analogous effect of the ion current,

$$I_{e,sat} \approx 0.6 e n_e \sqrt{\frac{k_B T_e}{m_e}} A_{probe}. \tag{3.10}$$

There is also an analogous exponential contribution for the ion current, but the electron current dominates the characteristics. The total current I_L in the exponential region is then

$$I_L(U) \approx 0.6 e n_e \sqrt{\frac{k_B T_e}{m_e}} A_{probe} \left(1 - \exp\left(\frac{e(\Phi_p - U)}{k_B T_e}\right)\right). \tag{3.11}$$

From a regression in the exponential region, the electron temperature T_e is obtained. This temperature then can be used to get the density from the ion saturation current. The electron saturation current is not used as density diagnostic because of its strong dependence on the probe shape, as shown in figure 3.9, that originates in the differing charge trajectories for the probe shapes (see e.g. [56]). In fusion plasmas, Langmuir probes can only be used in edge regions. The very high temperatures and densities in the plasma core would be lethal to Langmuir probes. TJ-K temperatures and densities are rather low for a fusion-relevant experiment. Therefore, Langmuir probes can be used in the entire plasma and are extensively used in turbulence studies by means of sophisticated Langmuir probe arrays [58, 59]. A 2D-movable probe is available at the outer port O6 that is used to acquire one-dimensional density profiles for the simulations of electron trajectories (see section 5) and ECE propagation (section 4.2). This probe is also used to measure temperatures that are compared to temperatures obtained by ECE measurements. The wire consists of tungsten with a diameter of 0.2 mm. The cylindrical tip of the probe is approximately 2 mm long. The rest of the wire is electrically shielded from the plasma by means of an Al_2O_3 ceramic tube.

3.5 Microwave heating

A plasma in TJ-K can be generated by accelerating electrons in the electric field of a microwave. When an electron gains enough energy to ionize an atom before it collides, a cascade of ionizations can be reached that provides for the charge densities needed for a plasma. Further energy transfer from the microwave to the electrons also provides for the electron temperatures that are needed for plasma properties. A very efficient way to transfer energy from the wave field to the electrons is to use a microwave frequency that equals the gyration frequency of the electrons in the magnetic field of the confining magnetic cage. This method is called electron cyclotron resonance heating (ECRH) [60]. At TJ-K microwave sources in three different frequency ranges are currently available:

A magnetron at port B4 operates at the fixed frequency of 2.45 GHz with adjustable output power up to 3 kW. Due to the low amount of current that is needed to generate the relatively low field strength for 2.45 GHz resonance, a long operation time in the range of 30-45 minutes is possible before the coil system reaches its temperature limit. In the 14 GHz range, there is a system of three klystrons that can be used to heat the plasma [53, 61]. The microwaves from two of these klystrons are coupled and enter the vessel at port T4. The third klystron can be connected via an array antenna at port O2.

For ECRH, very large coil currents are needed to generate the magnetic field for 14 GHz microwaves. Therefore, this heating scenario comes with short operation times of no more than 45 seconds.
A klystron that operates around 8 GHz is connected via a flexible waveguide and a phased array antenna to port O1. The klystron supports 8 different working frequencies in the range of 7.9 GHz to 8.4 GHz. For the measurements in this work, this system was used and the heating frequency was chosen to be 8.256 GHz, exclusively. Over the magnetron, the klystron has the advantage of a very clean emission spectrum. Compared to the 14 GHz system, the 8 GHz system is beneficial because of the longer operation times due to lower magnetic field currents.
The array antenna that is sketched in figure 3.1 splits the power from the klystron into several waveguides with different lengths. Between each pair of neighboring lines, the length differs by 290 mm. At the antenna aperture, these single delay lines come together with different phases. By superposition, a horizontally tilted microwave beam is created. When a different microwave frequency is used, the tilt angle of the heating microwave changes due to the altered phase difference between the lines. In table 3.1 the emission angles of the antenna are shown for different frequencies where positive angles are towards port O2 and negative angles towards port O6. Negative angles, therefore, mean that the propagation of the microwave has a component parallel to the toroidal magnetic field, positive angles mean that the emission is tilted in the antiparallel direction.

frequency in GHz	emission angle in °
7.9	-44.8
8.0	-28.4
8.1	-8.1
8.2	9.2
8.3	24.7
8.4	42.7

Table 3.1.: Emission angles of the 8 GHz array antenna for different frequencies [62].

As the dependence on the frequency is almost linear in this region, for the klystron frequency of 8.256 GHz used in this work the emission angle is about +18°. For 8 GHz ECRH heating a coil current of about 1100 A is needed which allows for measurements up to 2 minutes. The klystron used as microwave amplifier in this work is a CPI K3X65C klystron [63] with a maximum of 2.6 kW continuous wave power at the output flange fed by an Anritsu 68147C frequency generator. The -1 dB bandwidth is 40 MHz and the harmonic output is lower than -80 dBc. For a carrier signal of 2 kW at 8.256 GHz, this means that the second harmonic at 16.512 GHz is weaker than $20\,\mu$W. In an electron cyclotron resonance heated plasma, this second harmonic emission from the klystron is natively in the second harmonic ECE frequency range that a diagnostic detects. Its effect on the measurements is discussed in section 4.4.2.
Power modulation of this klystron is possible in different ways. Either the input signal from the signal generator is modulated or the klystron's "RF Inhibit" switch is used that disconnects the power from the solid-state intermediate power amplifier that pre-amplifies the signals in the CPI K3X65C before they reach the klystron tube.

3.6 Comparison to other experiments concerning electron cyclotron emission (ECE)

There is a wide variety of fusion experiments with electron cyclotron emission diagnostics. Some of the important parameters for ECE measurements are summarized in table 3.2 for TJ-K and four different magnetically confined plasma experiments: the ASDEX Upgrade (AUG) tokamak and the stellarators Wendelstein 7-X (W7-X), the Compact Helical System (CHS) and the Wendelstein Experiment in Greifswald für die Ausbildung (WEGA)[1].

experiment	TJ-K	WEGA	CHS	AUG	W7-X
vessel radii in m	0.6 ; 0.175	0.72; 0.19	1; 0.4	1.6; 0.6-1.2	5.5; 0.5-1.25
poloidal vessel shape	circular	circular	circular	D-shaped	bean-shaped
magnetic field in T	0.27	0.5	1	3	3
ECE frequency in GHz	15	28	56	140	140
ECE wavelength in mm	20	11	5	2	2
electron density in m^{-3}	$6 \cdot 10^{17}$	$5 \cdot 10^{18}$	10^{19}	$2 \cdot 10^{20}$	$3 \cdot 10^{20}$
$k_B T_e$ in eV	10	50	500	$1.3 \cdot 10^4$	10^4
optical depth	$2 \cdot 10^{-3}$	$8 \cdot 10^{-3}$	0.5	> 1	> 1
data source		[18, 65]	[28, 66, 67]	[68, 69]	[70]

Table 3.2.: Comparison of different parameters concerning microwaves and ECE in TJ-K, WEGA, ASDEX Upgrade (AUG), Wendelstein 7-X (W7-X) and the Compact Helical System(CHS).

CHS and WEGA were chosen since their plasmas are optically thin for their respective ECE diagnostics [18, 28]. TJ-K with its major vessel radius of 0.6 m and its minor vessel radius of 0.175 m is the smallest of these experiments. The vessel of WEGA has dimensions comparable to TJ-K but is still larger than it. As a result, TJ-K has the strongest wall curvatures, especially at the inboard side. The main requirement for ECE diagnostics is the existence of a magnetic field which leads to the gyration of the electrons and the emission of microwaves. Since the strength of the magnetic field determines the gyration frequency, it also directly determines the ECE frequency and wavelength. In TJ-K a comparatively weak field strength of about 270 mT on axis places the second harmonic ECE frequency around 15 GHz with 2 cm of wavelength. This leads to broad microwave beams, or a wide field of view of a diagnostic compared to AUG, W7-X, CHS and WEGA where much smaller ECE wavelengths are used. Two effects on the localization of measurements result from that: the field of view includes a large lateral part of the resonant emitting surface, covering multiple flux surfaces, and its spot on the strongly three-dimensionally curved inner vessel wall is large. Extraordinary is the small optical depth of about $2 \cdot 10^{-3}$ resulting from the low densities and temperatures. While AUG and W7-X operate in optically thick plasmas, even the low optical depths in the Compact Helical System are at least in the vicinity of unity. The already very low optical depths that were measured at the stellarator WEGA were about $8 \cdot 10^{-3}$ which is still a factor of 4 above the expected value for TJ-K. For the design of an ECE diagnostic at TJ-K, the combination of low optical depth, a broad field of view and a strongly curved vessel impose a challenge on localized measurements. This challenge is addressed in chapter 4.

---

[1] after its retirement in 2013, WEGA was moved to the U.S.A. and renamed to HIDRA [64].

4 Design and test of an electron temperature diagnostic using ECE for TJ-K

An electron cyclotron emission (ECE) diagnostic for the second harmonic X-mode is designed, built and used for temperature measurements as described in this chapter. Important theoretical aspects are discussed in section 4.1 followed by their application to TJ-K. In the subsequent section 4.2, 3D simulations are presented to find the distribution of the contributing emissive regions for the diagnostic. Section 4.3 specifies the components used for the diagnostic and gives details about the design process for TJ-K individualized parts. The following sections 4.4 and 4.5 show a comparison of theoretically expected microwave properties to experimental results at TJ-K, assisted by simulations. Electron temperatures measured with the new ECE diagnostic at TJ-K are benchmarked against Langmuir probe measurement results in section 4.6. Finally, the applicability of an ECE diagnostic to the extraordinarily optically thin plasmas of TJ-K is summarized and discussed in section 4.7.

4.1 Electron cyclotron emission in TJ-K

4.1.1 Electron cyclotron emission theory

The circular gyration of electrons is an accelerated motion of a charge and therefore leads to the emission of electromagnetic waves. With Maxwell's equations for an electric field $\vec{E}_1$, magnetic field $\vec{B}_1$, charge density ρ, current density $\vec{j}$, electric field constant ε_0 and the magnetic field constant μ_0,

$$\begin{aligned}
\vec{\nabla} \cdot \vec{E}_1 &= \frac{\rho}{\varepsilon_0}, \\
\vec{\nabla} \cdot \vec{B}_1 &= 0, \\
\vec{\nabla} \times \vec{E}_1 &= -\frac{\partial \vec{B}_1}{\partial t}, \\
\vec{\nabla} \times \vec{B}_1 &= \mu_0 \vec{j} + \mu_0 \varepsilon_0 \frac{\partial \vec{E}_1}{\partial t},
\end{aligned} \tag{4.1}$$

as a starting point, the emissive character of a gyrating charge is easy to understand. The circular motion is decomposed into two linear oscillations with $\pi/2$ phase difference that are perpendicular to each other and simultaneously perpendicular to the background magnetic field. Each linear charge motion forms an alternating electric current. According to the last line of equations (4.1) (the Maxwell-Ampère law) this leads to an oscillating curl of a magnetic field. This oscillating magnetic field itself leads to an oscillating electric field as the third line (the Maxwell-Faraday equation) shows. With the coupling of this electric field back to a magnetic field in the Maxwell-Ampère law, an electromagnetic wave that propagates away from the gyrating charge is formed. The emission perpendicular to the local background magnetic field vector $\vec{B}$ is not simply generated by a linearly oscillating charge but due to the non-zero size of the gyroradius the second linear motion comes into play: the electron moves periodically parallel to the direction of propagation of the emitted wave. This leads to an emission spectrum that is composed of harmonics l of the angular cyclotron or gyration frequency ω_{ce} [18,34]:

$$\omega_{ce,l} := l \cdot \omega_{ce} = l \cdot \frac{e|\vec{B}(\vec{r})|}{m_e}. \tag{4.2}$$

ECE perpendicular to the magnetic field (X-mode) is described in the following as this is the main contribution [22] and therefore a perpendicular line of sight $\vec{s}$ ($\Theta := \sphericalangle(\vec{B}, \vec{s}) = 90°$) is chosen for the ECE diagnostic. This choice simplifies and clarifies the description. In some cases in the following, first the general formulas are shown and then simplified in the end by inserting Θ as well as the harmonic number which is $l = 2$ for the second harmonic that is used.

The intensity of the radiation is dependent on the electron temperature whereas its frequency is determined by the strength of the background magnetic field $|\vec{B}|$. Since the magnetic field is not homogeneous, a range of frequencies for electron cyclotron emission is possible. In order to have one defined location where the radiation with a certain frequency comes from, it is important to measure along a line of sight where the absolute magnetic field has a monotonous and non-zero gradient. This is the case for the line of sight from an outer port of TJ-K inwards along the major radius up to the inner vessel wall as can be seen in figure 3.5. For TJ-K plasmas with a nominal coil current of 1140 A the frequency ranges for the four first harmonics inside the confinement region at the poloidal plane of an O-port are listed in table 4.1 showing an overlap of the frequency bands.

harmonic	frequency in GHz	relative power
1st	4.7 to 9.5	$4.5 \cdot 10^4 \mathrel{\hat{=}} +47\,\mathrm{dB}$
2nd	9.4 to 19	$1.0 \mathrel{\hat{=}} 0\,\mathrm{dB}$
3rd	14 to 28	$2.8 \cdot 10^{-5} \mathrel{\hat{=}} -46\,\mathrm{dB}$
4th	18.8 to 38	$8.8 \cdot 10^{-10} \mathrel{\hat{=}} -91\,\mathrm{dB}$

Table 4.1.: ECE harmonic frequencies in TJ-K and X-mode ECE strength for perpendicular observation normalized to the second harmonic.

From measurements of the intensity spectrum, a temperature profile along the line of sight of the diagnostic can be generated. Except for broadening effects that are described at the end of this section the spatial resolution is determined by the frequency resolution Δf and the field gradient, which yields for the second harmonic at a non-relativistic plasma:

$$\Delta f = \frac{1}{2\pi} \Delta\omega_{ce,2} = \frac{1}{2\pi} \cdot 2 \cdot \frac{e}{m_e} \Delta|\vec{B}|. \tag{4.3}$$

When the diagnostic measures with a bandwidth of $b = 3\,\mathrm{MHz}$ then this corresponds to the range $\Delta|\vec{B}|$ in the magnetic field strength

$$\Delta|\vec{B}| = 3\,\mathrm{MHz} \cdot \pi \cdot \frac{m_e}{e} \approx 5.4 \cdot 10^{-5}\,\mathrm{T}. \tag{4.4}$$

Since the magnetic field in the 8 GHz heating scenario changes along a horizontal axis through an

O-port of TJ-K at rates between $0.65\,\frac{\mathrm{T}}{\mathrm{m}}$ and $1.2\,\frac{\mathrm{T}}{\mathrm{m}}$ in the confinement region (see figure 3.6), the spatial resolution is between $46\,\mu$m and $85\,\mu$m. This resolution is only of the size of some electron Larmor radii which is of the order of $30\,\mu$m in the same scenario with $k_BT_e \approx 10\,\mathrm{eV}$. A desired spatial resolution of a millimeter would require a measurement bandwidth of about 50 MHz.

Along its propagation path, the electron cyclotron radiation experiences different refractive indices N caused by the electron density and the background magnetic field. Also, it is absorbed and emitted in resonant regions. At a location with a certain magnetic field strength not only the discrete harmonic frequencies can be emitted and absorbed, as equation (4.2) could suggest, but the slight variations in the electrons' masses due to the relativistic mass shift and their velocity distribution lead to a shape function Φ_l for the emission and absorption spectrum [34] with

$$\Phi_l(\omega) = \frac{\sqrt{\pi}\omega}{\omega_{ce,l}^2}\left(\frac{2m_ec^2}{k_BT_e}\right)^{l+1.5}\frac{l!}{(2l+1)!}\left(1-\frac{\omega}{\omega_{ce,l}^2}\right)^{l+0.5}\exp\left(\frac{-m_ec^2}{2k_BT_e}\left(1-\frac{\omega^2}{\omega_{ce,l}^2}\right)\right). \tag{4.5}$$

The shape function of the second harmonic for different temperatures in the typical range for TJ-K is shown for ($R \approx 0.605\,\mathrm{m}$, $z = 0\,\mathrm{m}$, $\phi = 90°$), on the central line at port O5, in figure 4.1 for observation perpendicular to the magnetic field.

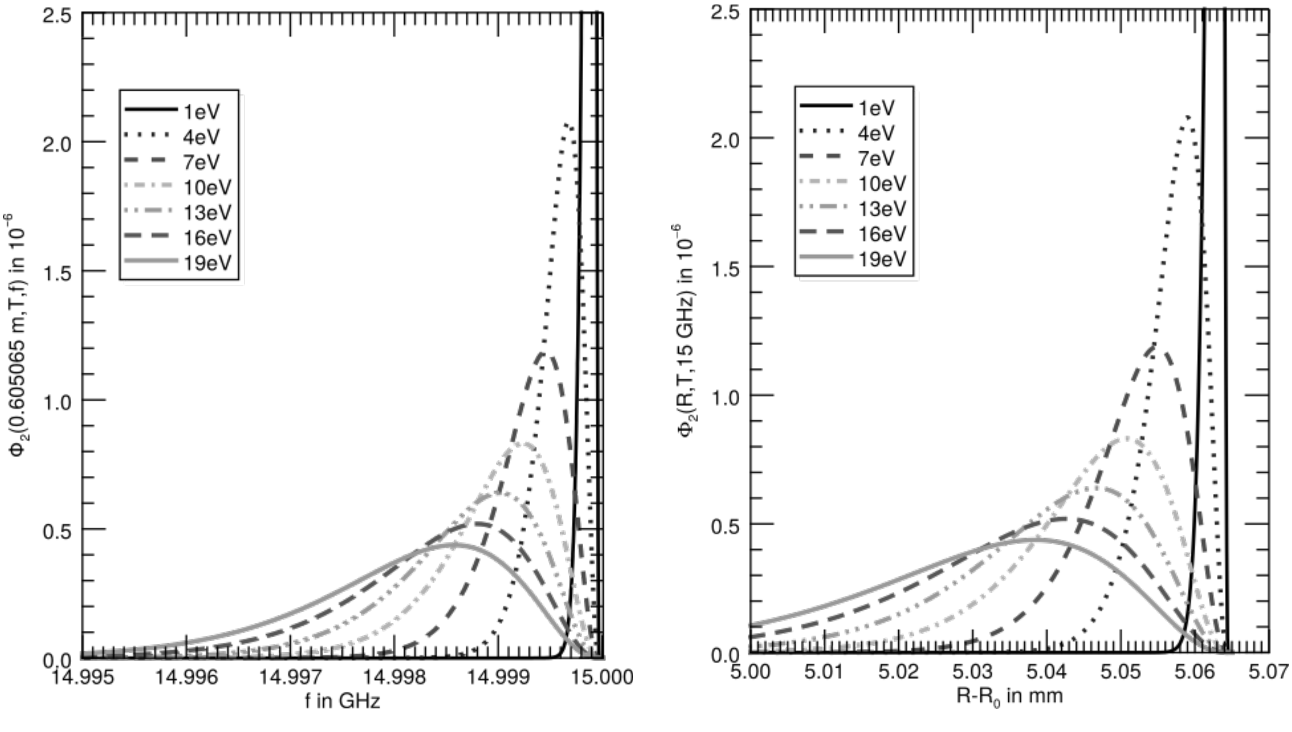

Figure 4.1.: Frequency distribution of the second harmonic shape function for perpendicular observation of electron cyclotron emission in TJ-K at ($R \approx 0.605\,\mathrm{m}$, $z = 0\,\mathrm{m}$, $\phi = 0.5\pi$) with $|\vec{B}| = 247.7\,\mathrm{mT}$ and the spatial distribution for 15 GHz covering a field span of 0.68 mT, both for different thermal energies, 1140 A and $r_{vh} = 57\,\%$.

The shape function for the weak parallel emission is determined by Doppler broadening and thus has a Gaussian distribution. Since the ECE diagnostic at TJ-K measures along the major radius, the case of perpendicular observation can be used as a first approximation. With increasing thermal energies the shape functions Φ_l becomes broader. Consequently, the shape function's height decreases with higher thermal energies in order to fulfill the normalization $\int \Phi_l(\omega)\mathrm{d}\omega = 1$. The full width at half maximum

(FWHM) is of the order of a few MHz which is in the range of the bandwidth of ECE measurements at TJ-K.

The emission is described by the emissivity j_l which is the emitted power P_l per plasma volume V, frequency and solid angle Ω. For a Maxwellian-distributed $f_M(\vec{v})$ electron population with the speed parallel to the background magnetic field $v_\parallel$ and perpendicular to it $v_\perp$ and the vacuum speed of light c the emissivity is [34]

$$\begin{aligned} j_l &= 2\pi \int \frac{\partial^2 P_l}{V \partial\omega\partial\Omega} f_M(\vec{v}) v_\perp \mathrm{d}v_\perp \mathrm{d}v_\parallel \\ &= \frac{e^2\omega_{ce,l}^2 n_e}{8\pi^2\varepsilon_0 c} \frac{l^{2l-1}}{(l-1)!} \sin(\Theta)^{2(l-1)} (\cos(\Theta)^2+1) \left(\frac{k_B T_e}{2m_e c^2}\right)^l \cdot \Phi_l(\omega), \\ j_{2,\Theta=90^\circ} &= \frac{e^2\omega_{ce,2}^2 n_e}{\pi^2\varepsilon_0 c} \left(\frac{k_B T_e}{2m_e c^2}\right)^2 \cdot \Phi_2(\omega), \end{aligned} \tag{4.6}$$

where the last line is true for the second harmonic with observation perpendicular to the magnetic field ($l = 2$, $\Theta = 90°$). The absorption coefficient α has a similar structure [34]:

$$\begin{aligned} \alpha_l &= \frac{\pi}{2c} \frac{e^2 n_e}{m_e\varepsilon_0} \frac{l^{2l-1}}{(l-1)!} \sin(\Theta)^{2(l-1)} (\cos(\Theta)^2+1) \left(\frac{k_B T_e}{2m_e c^2}\right)^{l-1} \frac{\Phi_l(\omega)}{2\pi}, \\ \alpha_{2,\Theta=90^\circ} &= \frac{2}{c} \frac{e^2 n_e}{m_e\varepsilon_0} \frac{k_B T_e}{2m_e c^2} \Phi_2(\omega). \end{aligned} \tag{4.7}$$

Both the emissivity and the absorption determine the evolution of the radiation intensity of the ECE along the line of sight $\vec{s}$ of the diagnostic as described by the radiation transport equation:

$$\frac{\mathrm{d}I}{\mathrm{d}s} = j - \alpha I. \tag{4.8}$$

How the intensity evolves for the second harmonic in TJ-K is investigated in section 4.1.2. The contribution from different harmonics can already be estimated from the ratio of the ECE power P_{l+1} of the $(l+1)$-th X-mode ECE harmonic normalized to the l-th harmonic [3]:

$$\frac{P_{l+1}}{P_l} = \left(\frac{v_\perp}{2c}\right)^2 \left(\frac{l+1}{l}\right)^{2l}. \tag{4.9}$$

The relative ECE powers in table 4.1 were obtained from this equation for $k_B T_e = 10\,\mathrm{eV}$ and with equal parallel and perpendicular velocities. The values show that there is no significant contribution from harmonics with $l > 2$ and therefore their frequency overlap can be neglected. Emission much stronger than the second harmonic is expected from the first harmonic. Therefore, its power would be easier to detect but the first harmonic comes with complications like larger wavelengths that require large waveguide and antenna components and reduce the spatial resolution as well as the need for a narrow high-power filter that protects the diagnostic from the kilowatt heating power. Furthermore, the first harmonic can not propagate freely in the plasma due to cutoffs (see section 4.2). Therefore, the first harmonic is not chosen for the ECE diagnostic. As seen in table 4.1, there is almost no frequency overlap between first and second harmonic at outer ports of TJ-K where the ECE diagnostic will be placed such that the frequency range from 9.5 GHz to 19 GHz is free from significant ECE other than the second harmonic. Therefore, the second harmonic is used for the ECE diagnostic at TJ-K. Perpendicular observation eliminates the angular dependencies in the absorption and emissivity since

$\sin(\Theta)^{2(l-1)}(\cos(\Theta)^2+1)=1$ for $\Theta=\pi/2$. In the case of the second harmonic ($l=2$) deviations of more than 3° still show 99.9 % of emissivity j and absorption coefficient α, deviations of 10° more than 90 %. Therefore, the discussion of the theory is limited to the perpendicular case for the second harmonic ECE. As a rule of thumb, the O-mode ECE is by $(v_{\|}/2)^2$ weaker than the X-mode [3]. For example, for the pitch angle of $\eta=\arctan(v_{\perp}/v_{\|})=\pi/4$ and $k_BT_e=10\,\mathrm{eV}$ this means that the X-mode is by +47 dB stronger and the O-mode can thus be neglected.

As the frequency of the electron cyclotron radiation is used to obtain the position where it originates from, frequency broadening effects play an important role in the spatial resolution of an ECE diagnostic. Doppler broadening and the line width due to relativistic broadening including the Maxwellian velocity distribution were already mentioned. The importance of these and more broadening effects for ECE measurements at TJ-K is discussed in the following. All given line widths are for 15 GHz second harmonic ECE with a thermal energy of 10 eV and the electron density $n_e=5\cdot10^{17}\,\mathrm{m}^{-3}$.

The line width due to the relativistic mass increase was already discussed (see equation 4.5) including the velocity distribution in the plasma. For realistic TJ-K data, the line width depending on the thermal energy is plotted in figure 4.1. The width from the shape function is about 1.3 MHz for this location. According to the simplified approximation formula [34]

$$\Delta f \approx f\cdot\frac{k_BT_e}{m_ec^2}, \tag{4.10}$$

the relativistic broadening produces a width of only 0.3 MHz. However, both values are of the order of the measurement bandwidth $b=3\,\mathrm{MHz}$ that will be used in the experiments.

Doppler broadening strictly only occurs if the observation angle differs from 90°. But because of the 3D twisted and curved field lines, there is always a portion of the radiation that is not seen perpendicularly to the magnetic field. Especially when reflections in the vessel are considered, a mixture of observation angles is present and the Doppler shift, as well as a combination of X-mode and O-mode, is seen by the diagnostic. The line width due to Doppler broadening is about [34]

$$\Delta f \approx f\cdot\sqrt{\frac{k_BT_e}{m_ec^2}}\cos\Theta, \tag{4.11}$$

with the observation angle $\Theta=\sphericalangle\left(\vec{B},\vec{s}\right)$ and the line of sight $\vec{s}$. For purely perpendicular observation ($\Theta=\pi/2$) the line width from Doppler broadening vanishes. Purely parallel observation has a width of 66 MHz in this case. For 10° deviation from this case the line width at 10 eV and 15 GHz is about 12 MHz. In comparison, the root mean squared variation of the direction of the magnetic field in a cylindrically modeled field of view at the center of the outer port is with 8.2° lower (see section 3.3). Because the width of a field of view will be lower than the size of the port, the Doppler broadening can also be expected to be in the range of the 3 MHz bandwidth of the diagnostic.

When an emitter is deflected or decelerated by a collision the radiative process ends abruptly leading to the emission of broad bandwidth bremsstrahlung. The line width created from this collisional broadening is in the same range as the collision frequency [71]. In the case of ECE, these collisions can happen with other electrons, ions or neutral atoms. The line width Δf_{coll} due to collisions can be approximated by [16]

$$\Delta f_{coll} \approx \frac{\omega_{pe}}{2\pi}\frac{\ln(\Lambda)}{\Lambda}, \tag{4.12}$$

where $\ln(\Lambda) \approx \ln\left(\frac{(12\pi)^2\varepsilon_0^3 k_B^3 T_e^3}{e^6 n_e} - 1\right)$ is the Coulomb logarithm that describes the relative contribution of small-angle scattering processes in the Coulomb potential of the scattering partner [4]. For TJ-K, the Coulomb logarithm is approximately 13 and the collision damping leads to 0.8 MHz width which is lower than the widths generated by the previously discussed effects. Therefore, the width due to collisional broadening is covered by the other widths.

Radiation broadening comes from the fact that the emitting electron loses energy to the electromagnetic wave leading to the reduction of its velocity [71]. The line width due to this effect is given by [16]

$$\Delta f \approx \frac{1}{2\pi}\frac{\omega_{ce}^2 4e^2}{3m_e c^3}, \tag{4.13}$$

which is only of the order of 10^{-13} Hz for the magnetic field of TJ-K and can be neglected. Further broadening effects like quantum effects are also negligible [16].

The comparison of the different effects shows that the broadening is dominated by relativistic broadening for perpendicular observation and Doppler broadening as soon as the observation is not perpendicular to the magnetic field. When the observation is close to perpendicular, the measurement bandwidth $b = 3\,\mathrm{MHz}$ is still larger than the line widths and therefore determines the spatial resolution according to the magnetic field structure described in section 3.3.

4.1.2 Numerical calculation of electron cyclotron emission radiation transport

In section 4.1.1 the importance of radiation emission and absorption for the intensity measured by an ECE diagnostic is described from the point of view of a fixed position. From the perspective of a fixed frequency, which is the view that a spectrometric diagnostic has, the shape function Φ_2 comes into play by consideration of the spatial gradient in the magnetic field strength. This means that ECE with a certain frequency is not only emitted and absorbed at the exact location where equation (4.2) is fulfilled but the combination of shape function and magnetic gradient creates a width of the region of emission and absorption for a discrete frequency.

The spatial shape function for 15 GHz is shown in figure 4.1 on the right. Naturally, also the spatial shape function becomes wider with higher thermal energies. The evolution of the intensity I of ECE along its propagation path $\vec{s}$ is described by the radiation transport equation (4.8): ECE from the resonant surface is absorbed according to the local absorption coefficient α and (re-)emitted with the local emissivity j along its path to the antenna, finally yielding the intensity that is measured. The resulting intensity can be obtained by integration of the radiation transport equation along its path including the local variations in j and α. Plasma parameters contribute to the emissivity and the absorption mainly through the electron density and the electron temperature. High densities and temperatures result in strong absorption and emission leading to the saturation of the intensity at the black body power P_{RJ} for the temperature of the black body T_{BB} as given by the Rayleigh-Jeans law, in the low-frequency approximation [34]:

$$P_{RJ} = \frac{f^2}{c^2} k_B T_{BB}. \tag{4.14}$$

The Rayleigh-Jeans law, therefore, can be used to obtain the black body temperature T_{BB} from the measured power. In many plasmas, emission and absorption do not reach the black body level. The apparent temperature from ECE measurements in this case, the radiation temperature T_{rad}, is [3]

$$T_{rad} = T_{BB} \cdot (1 - \exp(-\tau)) \,, \tag{4.15}$$

with the optical depth $\tau = \int \alpha ds$ which is a commonly used number to classify plasma conditions with respect to ECE measurements. In the complex geometries of fusion related experiments the radiation transport equation is often solved numerically to obtain information about τ. Then the electron temperatures can be derived from power measurements. For TJ-K, one-dimensional numerical integration of the absorption coefficient for the second harmonic α_2 (see eq. (4.7)) from the emission region outwards to the position of the antenna is performed to obtain the optical depth. For the modeled density profile of section 4.2.3, the actual absolute magnetic field strength and $k_BT_e = 10\,\text{eV}$ the calculation results in $\tau \approx 2 \cdot 10^{-3}$ when the path is approximated as perpendicular to the magnetic field. Variation of the thermal energy shows an approximate proportionality in the range relevant for TJ-K. When the integration is continued inwards and out again, an effective optical depth for multiple passes through the plasma can be calculated that would be valid for an ideal (no losses at reflections) multipass emission. The effective optical depth then increases linearly with the number of passes reaching the optically thick case ($\tau \geq 1$) after 230 passes for the second harmonic X-mode.

The radiation transport equation (4.8) was integrated one-dimensionally for TJ-K parameters at an outer port for the region around $R = 0.63\,\text{m}$ and $z = 0$, where the second harmonic ECE radiates at 14 GHz and the third harmonic at 21 GHz. As soon as multiple reflections in the vessel or various orientations of the magnetic field vector in a stellarator are considered, the electron cyclotron emission is a mixture of mass shift broadened and Doppler-broadened radiation and a mixture of X- and O-polarization, although the emission is mainly in X-polarization. Nevertheless, the propagation along the major torus radius R was approximated to be perpendicular to $\vec{B}$, such that the angular dependence in the emissivity and absorption were neglected. The integration is performed with ideal reflections at the vessel walls. The intensity is evaluated each time when the position at the low-field side where the antenna is positioned in the experiments is reached, defined as the pass number. The second harmonic ECE intensity over the thermal energy is shown for different numbers of passes in figure 4.2.

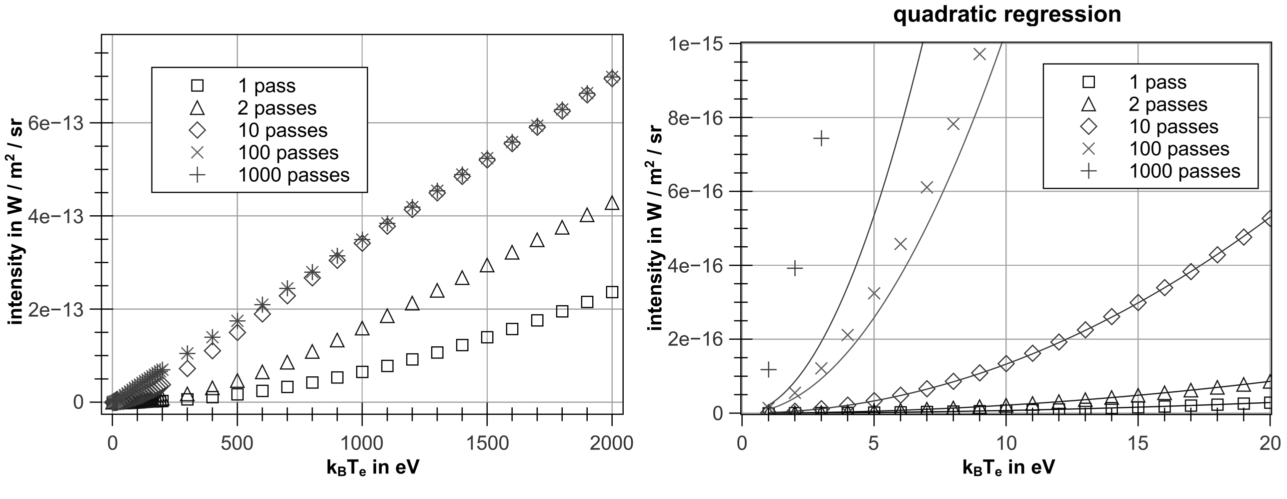

Figure 4.2.: Intensity from one-dimensional integration of the radiation transport equation in TJ-K for different thermal electron energies and numbers of passes through the plasma. The right graph shows a zoom into the TJ-K relevant range with quadratic regression curves.

For thermal energies in the keV range, the linear behavior that is predicted by the Rayleigh-Jeans law with the correction for the radiation temperature via the optical depth, eq. (4.15), can be seen. At even higher energies, the curves converge showing no different intensities for the pass numbers. For low numbers of passes or low thermal energies, the curve is not linear. The graph on the right-hand side in the figure shows a zoom into the temperature range that is typical for TJ-K plasmas. In this range, the intensity is quadratic in the thermal energy for pass numbers up to several dozens as the solid regression lines demonstrate. This behavior is expected when the emission of the second harmonic ECE is not accompanied by significant absorption, as then the intensity is dominated by the emissivity j_2 as given in equation (4.6). Therefore, the temperature dependence of the ECE power from TJ-K plasmas is expected to be quadratic as long as the number of reflections is limited although no report of another experiment with this type of ECE evaluation was found in the literature. However, this dependency is not expected for the usual optical depths which are even in optically thin plasmas orders of magnitude higher than in TJ-K. When the second harmonic ECE intensity is dominated by the emissivity, the measured signal power is not only proportional to the squared electron temperature but it is also proportional to the electron density as equation (4.6) shows. In the evaluation of electron temperatures from ECE measurements in section 4.6.4 this dependence will be used. In contrast, the black body power does not depend on the density but only on the temperature.

The harmonic power ratio has also been calculated. It starts at $P_3/P_2 \approx 1.1 \cdot 10^{-4}$ for a single pass, which is 4 times larger than the estimate listed in table 4.1. The difference is due to the more detailed description of the optically thin TJ-K plasmas in the calculation here. Both values prove that the frequency overlap of second and third harmonic cannot significantly disturb the measurements. When the radiation passes many times through the plasma, both the second and third harmonic intensity increase towards the black body level with a stronger increase of the third harmonic. Large numbers of passes of the order of several hundreds to thousands show a linear increase of the harmonic ratio. Still, even for twenty thousand passes, the third harmonic intensity is still only about $5 \cdot 10^{-3}$ of the second harmonic. As the results do not vary much for the frequencies relevant for TJ-K, the emission of the third or higher harmonic cyclotron radiation can be neglected completely.

4.2 Simulation of microwave propagation in the vacuum vessel

For diagnostic purposes, the microwaves that are emitted by gyrating electrons in the plasma have to reach the ECE antenna. In general, electromagnetic waves in plasmas can experience various resonances and cutoffs, that are described in detail for example by Stix [72], resulting from the magnetic field strength and the electron density profiles. At a resonance, the electromagnetic wave is absorbed while at a cutoff it is reflected. To propagate through a magnetized cold plasma, a wave with a linear polarization parallel to the background magnetic field needs a frequency above the electron plasma frequency f_{pe}. For the typical density profile in TJ-K, the plasma frequency is lower than 7 GHz, significantly below the second harmonic ECE as can be seen in figure 4.3 that shows the resonance and cutoff frequencies near the ECE frequencies at an outer port of TJ-K along the major radius R.

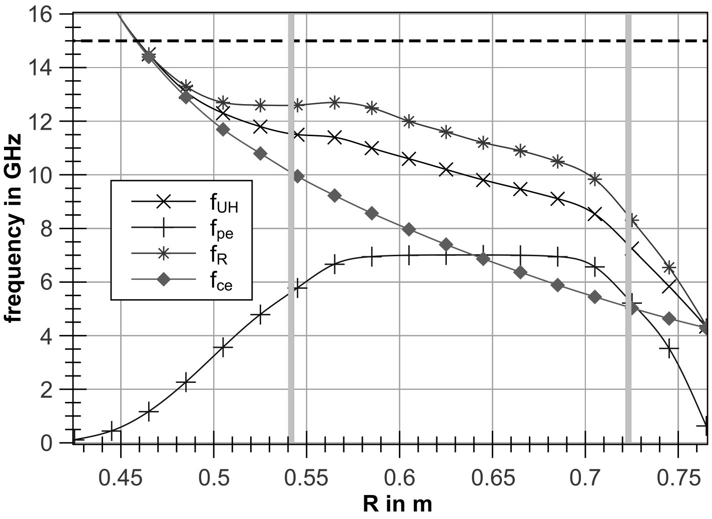

Figure 4.3.: Resonance and cutoff frequencies in the ECE frequency range at the central line of an outer port of TJ-K. The edge of the confinement region is indicated by gray lines and the employed ECE frequency of 15 GHz as black dashed line.

For a wave with a linear polarization perpendicular to the background magnetic field, a resonance at the upper hybrid frequency $f_{UH} = \frac{1}{2\pi}\sqrt{\omega_{pe}^2 + \omega_{ce}^2}$ appears. Circularly polarized waves that propagate parallel to the background magnetic field experience different effects depending on the sense of rotation. Waves with right circular polarization have a cutoff at $f_R = \frac{1}{4\pi}(\sqrt{\omega_{ce}^2 + 4\omega_{pe}^2} + \omega_{ce})$ which is above the plasma frequency while the cutoff for left circular polarization is below the plasma frequency. Because the plasma frequency decreases outside the last closed flux surface, f_R and f_{UH} converge with the cyclotron frequency towards low R. 15 GHz is reached approximately at the same major radius of about 46 cm where the plasma density is low. The cutoff frequency for waves with left circular polarization, the lower hybrid resonance frequency and the ion plasma frequency are all below the electron cyclotron frequency and thus not of interest for the second harmonic ECE frequencies. Precursor simulations have shown that the upper hybrid resonance shows significant influences on the microwave propagation for frequencies below 14 GHz. For higher frequencies, no influence is visible because of the very low plasma density allowing for the wave to transit the resonance layer undisturbed as it would also occur without a plasma. Therefore, 15 GHz is chosen as the frequency for ECE investigations at TJ-K.

For localized temperature measurements, it is important to know the place of origin for the power that is measured at each frequency. Ideally, the antenna only receives ECE from a small volume with constant temperature but when the microwaves reach the ECE antenna the measured power contains no information about the path of the microwaves. As soon as the signal comes from several flux surfaces with different temperatures, the evaluation will result in a weighted average temperature. This happens already for realistically broad viewing angles and widths of the field of view of the antenna but is extremely complex when the microwaves undergo multiple complicated reflections in the vessel. Microwaves with a frequency in the second harmonic ECE range of TJ-K can be efficiently reflected at the walls of a steel vessel [73]. Therefore, it is important to investigate the ECE propagation in TJ-K in order to understand the signals and optimize the ECE diagnostic. Investigations of the ECE origin are commonly done in fusion-related plasma experiments, usually by means of ray tracing simulations, for instance with TRAVIS [23], TRECE [25] or ECRad [24]. In these cases, the plasmas are optically thick or at least close to optically thick. Then the ray tracing simulations can be used to reconstruct temperature profiles from frequency spectra along lines of sight with only very few passes or even a single pass through the plasma. In the optically thin case of TJ-K, few passes do not suffice to explain the radiation temperatures that are measured but investigations in the entire plasma are needed. This cannot be handled in emission calculations since then the paths from all possible electron positions to the antenna need to be considered. Backward calculations with the reconstruction of the temperature profiles along a set of rays dividing the visual field of the antenna will end up in extremely long paths and need to be highly resolved to account for the low width of the emitting layers and the curved geometry of reflective surfaces. Using the Finite Difference Time Domain (FDTD) method for Maxwell's equations the microwave propagation can be simulated. This method is employed to investigate the field of view and the sensitivity region of the ECE diagnostic. Afterwards, cyclotron emitting regions are identified and used to evaluate the FDTD results concerning geometry effects on the field of view.

4.2.1 Finite difference time domain method for Maxwell's equations

At the IGVP a three-dimensional full-wave Finite Difference Time Domain (FDTD) code named IPF-FD3D [74] has been developed. This program is employed for the ECE investigation at TJ-K. Maxwell's equations (4.1) are solved on a 3D Cartesian grid including the influence of a 3D modeled plasma density and the 3D magnetic field in TJ-K. The application of IPF-FD3D for TJ-K was started in the master thesis of L. Bock [75] with the basic vessel geometry and a first plasma model and has been continued and extended for the final ECE simulations presented here. Electromagnetic waves are described by Maxwell's equations (4.1) that relate the derivatives of the wave electric field $\vec{E}_1$ and the wave magnetic field $\vec{B}_1$ and the current density $\vec{j}$. The temporal change of the electric and magnetic field are calculated using the Faraday equation and Ampère's law, which read in their general form [76]:

$$\begin{aligned} \frac{\partial \vec{B}_1}{\partial t} &= -\nabla \times \vec{E}_1, \\ \frac{\partial \vec{E}_1}{\partial t} &= \frac{1}{\mu_0 \varepsilon_0} \nabla \times \vec{B}_1 - \frac{1}{\varepsilon_0} \vec{j}, \end{aligned} \tag{4.16}$$

where ε_0 is the vacuum electric permittivity and μ_0 is the vacuum magnetic permeability. The current density $\vec{j}$ in the plasma is included neglecting the ion response because the ions are too inert to respond to the frequencies investigated. From the fluid equation for electrons the time evolution of the current density in the form

$$\frac{\partial \vec{j}}{\partial t} = \varepsilon_0 \omega_{pe}^2 \vec{E}_1 - \omega_{ce} \vec{j} \times \frac{\vec{B}}{|\vec{B}|}, \tag{4.17}$$

where $\vec{B}$ is the background magnetic field, can be derived [74] and used in equation (4.16). Electromagnetic waves in matter or vacuum can be simulated when the medium specific parameters are inserted. Solving these equations on a three-dimensional grid with the structure shown in figure 4.4 was introduced by K. Yee [77].

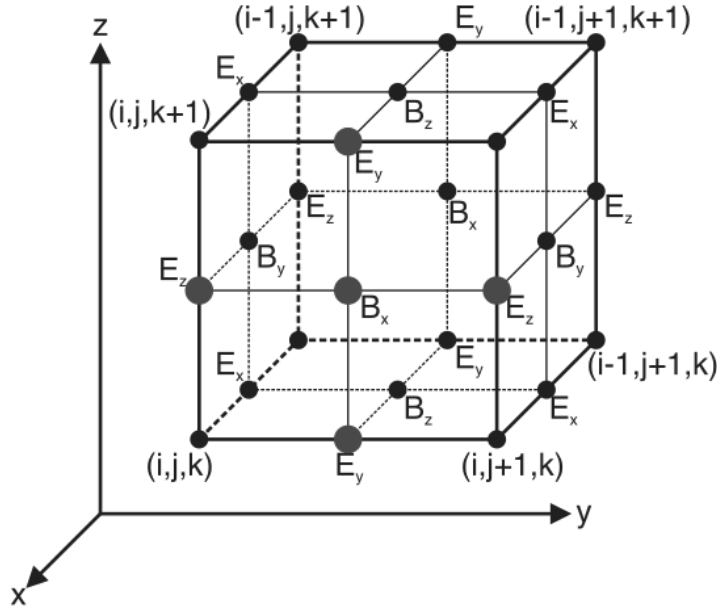

Figure 4.4.: Illustration of the grid setup in the Yee algorithm [78]. The values needed for the calculation of B_{1x} at grid point (i, j, k) are enlarged.

Compared to the solution of the wave equation for either the electric or the magnetic field this is a more robust algorithm that can also account for singularities in either the magnetic or electric field only [76]. The arrangement in the Yee grid accounts for the fact that the calculation of the change in a field needs the curl of the other field. By having the needed information at neighboring locations, the differentiations deliver the result at the desired grid point accurately. For example, the temporal change of the x-component of the magnetic field is, according to equation (4.16),

$$\frac{\partial B_{1x}}{\partial t} = -\left(\frac{\partial E_{1y}}{\partial z} - \frac{\partial E_{1z}}{\partial y}\right). \tag{4.18}$$

Since the fields that enter the calculations are not available analytically, the differentiations are performed numerically with spatial difference quotients. Furthermore, the time is discretized to time steps Δt in order to be able to store the information in a computer. Together, this leads to the computation at the grid point with indices (i,j,k)

$$\frac{\Delta B_{1x}^{(i,j,k)}}{\Delta t} = -\left(\frac{E_{1y}^{(i,j,k+1)} - E_{1y}^{(i,j,k)}}{\Delta z} - \frac{E_{1z}^{(i,j+1,k)} - E_{1z}^{(i,j,k)}}{\Delta y}\right). \tag{4.19}$$

As shown in figure 4.4, the information to calculate $B_{1x}^{(i,j,k)}$ is placed directly at the adjacent grid points. Therefore, the result of the difference quotients is valid exactly at the location where it is needed. All other steps to calculate the time evolution of equations (4.16) are computed analogously. The finite difference time domain (FDTD) iteration step to update the x-component of the magnetic field is then

$$B_{1x}^{(i,j,k)}(t + \Delta t) = B_{1x}^{(i,j,k)}(t) + \frac{\Delta B_{1x}^{(i,j,k)}}{\Delta t} \cdot \Delta t. \tag{4.20}$$

For physically correct results the grid resolution has to be fine enough to represent the geometry and the wavelength accurately and the time step needs to be small enough to resolve the frequency. The refraction and reflections are automatically handled by the FDTD method since basically Maxwell's equations are solved. Losses can be easily implemented as a damping term in the appropriate equation. For example, an effective collisional damping in the plasma can be modeled by a damping factor in the current density $\vec{j}$. Also, the geometry of the vacuum vessel can be included quite easily: the metal wall is modeled as a high-density plasma that automatically includes the reflections at the metallic walls and a reflection coefficient can be also modeled by damping the current density of the wall. Complex geometries and complicated reflections at arbitrary surfaces can, therefore, be simulated without decomposition of a beam in sub-beams and calculation of normal vectors as this would have to be done in geometrical optic approaches [79].

4.2.2 Antenna reciprocity theorem

A useful tool in the investigation of antennas is the antenna reciprocity theorem that relates the emission of an antenna to its reception of electromagnetic waves. It is based on the reciprocity theorem for electromagnetic waves and can be seen as the generalization of Kirchhoff's laws for electric circuits [80]. A derivation and formulation very suitable to the simulation of microwave propagation in TJ-K was provided by W. Dällenbach [81] and is summarized and applied here: for a fixed frequency, Maxwell's equations directly lead to the reciprocity of the electric field for anisotropic (and therefore also isotropic) media as long as the material constant tensors are time-invariant and symmetric at each point in the medium. This means that the conductivity tensor $\boldsymbol{\sigma}$ needs symmetric entries, $\sigma_{ik} = \sigma_{ki}$, as well as the magnetic permeability and electric permittivity have to be symmetric. Furthermore, the entries may not depend on the external field strengths. Then the amplitude and phase of an emitter and a receiver can be interchanged. For antenna systems this means that:

- exchange of sending and receiving antenna in a setup swaps the emitted and received signals and
- sending and receiving patterns of an antenna are equal.

Linearity and symmetry of the conductivity tensor are, however, not strictly fulfilled because of the magnetic field term in equation (4.17). Therefore, the reciprocity is in general violated when magnetic fields are present in gas discharges [81] or any ionized media [82]. An extension of the reciprocity theorem to ionized media with magnetic fields is possible if also the background magnetic field is reversed when the receiver and sender are swapped [83]. The electron density, the electron temperature and the background magnetic field are constant on the time scale of the ECE periodic times, which is about 67 ps for 15 GHz, and on the time scale of the entire simulation, which is below 190 ns for all cases considered in this work. Therefore, the material constants can be regarded as time-constant for the simulations and the conditions of the extended antenna reciprocity theorem are fulfilled.

The equality of sending and receiving pattern is employed in section 4.3.1 and 4.3.2 where the ECE antenna and a mirror are designed with full-wave simulations of emitted microwaves although both components are used as a receiving diagnostic in the experiment. Swapping a sender and a receiver if they have different antenna characteristics [82, 84] is the basis for the 3D full-wave simulations of the microwave propagation in TJ-K in section 4.2 where the ECE diagnostic's antenna is used as an emitter instead of simulating the emission of single electrons. This way, the computational effort is reduced substantially as a single simulation delivers the information for all electrons. The emitted waves are reflected in the vacuum vessel, travel around the torus and a standing wave pattern forms. When the wave field in the torus has reached its equilibrated state, the signal at a specific position is interpreted as the sensitivity of the diagnostic at this point because the reception there can be swapped for an ECE radiating electron. The distribution of the electric field in an equilibrated simulation with the ECE antenna as emitter can be understood as the amplitude sensitivity of the ECE antenna and tells about the cyclotron radiation emitting electrons that contribute to the measurement signals. Because of the oscillating nature of the electric field in a standing wave pattern, the squared electric field is time-averaged which also accounts for the fact that the diagnostic measures powers and not amplitudes. Furthermore, the electrons radiate independently such that there are random phase relations between all of them, their positions vary over time and also the frequencies differ locally due to the magnetic field gradients. Therefore, signals with a variety of amplitudes, frequencies and phases meet at the antenna aperture. In the antenna, the different waves are superposed and forwarded to the spectrum analyzer where they are squared and the signal power is displayed which is the sum of the power of all input signals in the measurement bandwidth (for a derivation see appendix A.2). For the interpretation of the simulations, this means that the measurement signal of the ECE diagnostic is the superposition of the contributions of emitting electrons weighted by the local squared electric field as obtained from full-wave the simulations.

4.2.3 Mapping of densities and temperatures

The electron density of a plasma fundamentally determines plasma physics in various ways: together with the temperature it forms the plasma pressure, the microwave propagation is influenced by its role for the refractive index, the emission of cyclotron radiation depends directly on the density of electrons and also the electric currents in the plasma are formed mostly by electrons. In many cases, the equilibrium density distribution in TJ-K is already sufficient but still not directly accessible in the entire vacuum vessel. The full three-dimensional geometry of TJ-K and of its plasmas are therefore modeled for numerical simulations. Because charged particles move fast on flux surfaces and perturbations of the velocity distribution relax on them, it can be assumed that equilibrium electron temperatures and densities are constant on flux surfaces [54]. Therefore it is possible to calculate typical densities and temperatures for the entire confinement region without performing measurements in the complete volume by mapping one-dimensional Langmuir probe measurements to entire flux surfaces.

The density profile shape was measured in the plasma of shot #12151 with 2.4 kW heating power at the standard fundamental frequency of 8.256 GHz and a neutral argon pressure of approximately 6.5 mPa. Langmuir probe data was acquired with the 2D-movable probe for $z = 0$ along the major radius starting close to the magnetic axis at $R_0 \approx 0.639\,\mathrm{m}$. The probe was moved in steps of 1 cm outwards into the outer port O6, acquiring current-voltage characteristics at each step which were used to obtain the electron density profile. Afterwards, the shape of this one-dimensional profile was approximated by two half super-Gaussian functions. For the mapping algorithm, the density function at port O6 is composed of the peak amplitude $\hat{n}_e$ and the shape function $\kappa(R)$:

$$n_e(R) = \hat{n}_e \cdot \kappa(R) \approx \begin{cases} \hat{n}_e \cdot \exp\left(\left(\frac{|R-R_0|}{w_1}\right)^{a_n}\right), & R \in [63.9\,\mathrm{cm}, 72.3\,\mathrm{cm}] \\ \hat{n}_e \cdot \exp\left(\left(\frac{|R-R_0|}{w_2}\right)^{a_n}\right), & R \in [54.2\,\mathrm{cm}, 63.9\,\mathrm{cm}[\end{cases} , \tag{4.21}$$

with $R_0 \approx 0.639\,\mathrm{m}$, $a_n \approx 5.75$, $w_1 \approx 0.094\,\mathrm{m}$ and $w_2 \approx 0.111\,\mathrm{m}$. The peak amplitude $\hat{n}_e$ can be set afterwards in order to adjust the profile to the required conditions. For simulations in this work, $\hat{n}_e = 6.09 \cdot 10^{17}\,\mathrm{m}^{-3}$ is used which is the average peak density obtained from the first 100 different plasma discharges of the ECE measurements for this work. The resulting one-dimensional density profile is shown in figure 4.5.

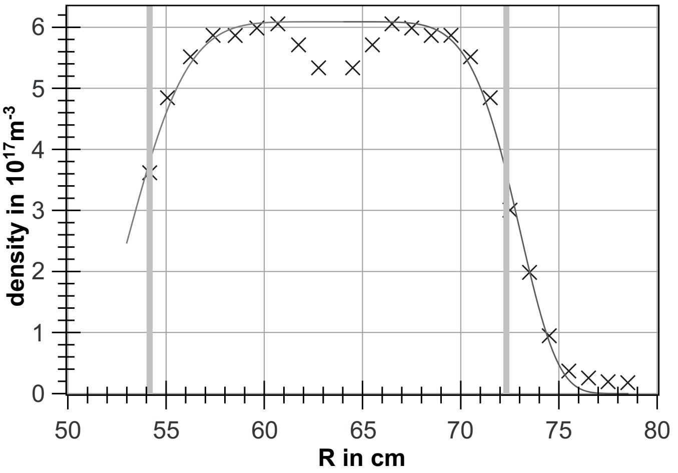

Figure 4.5.: 1D density profile from Langmuir probe measurements with fitted super-Gaussian approximation shown as solid line. The crosses above $R_0 \approx 0.639\,\mathrm{m}$ are the measurement results and the crosses below were mapped. The vertical bars indicate the position of the last closed flux surface.

To generate a three-dimensional density model from the measured profile, the nested flux surfaces in TJ-K are calculated and mapped by field line tracing using the Magnetic Confinement Code (MCC[1]) by Mirko Ramisch to port O6 where the density was measured. At $z = 0$ the density is obtained from the super-Gaussian regression, equation (4.21), and assigned to the entire flux surface. This is repeated for all calculated flux surfaces. For arbitrary points in the 3D confinement region, the density can be obtained by the following algorithm: The two flux surfaces that are closest to the point of interest are searched in its poloidal plane. The density at the point of interest is then set by linear interpolation of the densities that were assigned to these two flux surfaces. This method is used to generate 3D density grids of the confinement region for full-wave simulations of microwave propagation in TJ-K.
The model for the density distribution outside the last closed flux surface cannot be obtained from mapping techniques. Even if flux surfaces exist, the intersections of them with the vessel disturb the density and temperature on them because the metallic vessel can collect the electrons. Therefore, the density outside the confinement region is modeled as a function of the distance to the vessel with a vanishing density at the wall. This distance d is calculated in the poloidal plane along rays from the magnetic axis and is normalized to the distance between LCFS and vessel along each ray. As an example, the resulting distribution for port O6 is shown in figure 4.6.

---

[1] working title, unpublished. The code was benchmarked against the Gourdon code [85].

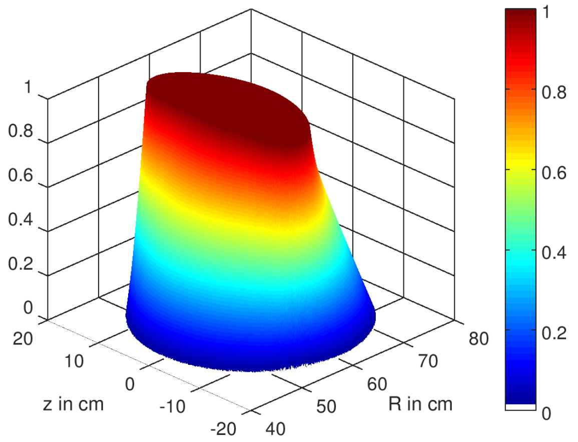

Figure 4.6.: Relative distance to the vessel wall measured from the LCFS and evaluated along rays from the magnetic axis. The value in the confinement region was fixed at $d = 1$.

In the confinement region, the density is calculated as described above. Outside the confinement region, the electron density is calculated by evaluation of equation (4.21) at $R = R_{vessel} - d \cdot (R_{vessel} - R_{LCFS})$, where $R_{vessel} = 0.775\,\text{m}$ is the edge of the circular poloidal cross-section at $z = 0$ and $R_{LCFS} \approx 0.723\,\text{m}$ is the outer LCFS point in that plane. This means that the radial coordinate outside the last closed flux surface is scaled according to the distance between the confined plasma and the vessel wall. The resulting density shape in this poloidal plane is shown in figure 4.7.

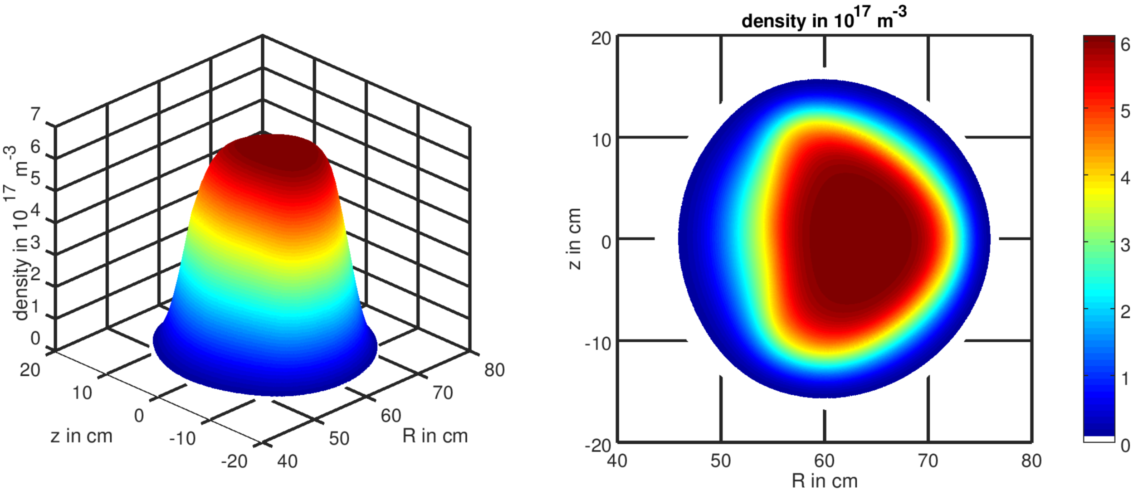

Figure 4.7.: Density distribution in the poloidal plane at port O6 modeled from Langmuir probe measurements as used for simulations shown as surface plot (left) and contour plot (right).

For flux surface calculations starting from the inner port 1 at $z = 0$ and $R \in [63.625; 63.702]\,\text{cm}$ magnetic islands [43] were found for the standard current ratio of 57 %. This small region of radii is omitted in the density modeling and the densities in between are determined by linear interpolation. The final 3D density model is continuous, models the confinement region based on the magnetic surfaces, provides a decaying density outside the confinement region and is zero at the vessel wall.

Simulations and theoretical considerations for the ECE diagnostic do not require detailed 3D temperature models. However, the same algorithm as for the density can also be used to obtain a 3D temperature model. Measured one-dimensional thermal energy profiles like in figure 4.8 show that the plasma center has a flat region with increasing temperatures towards the last closed flux surface.

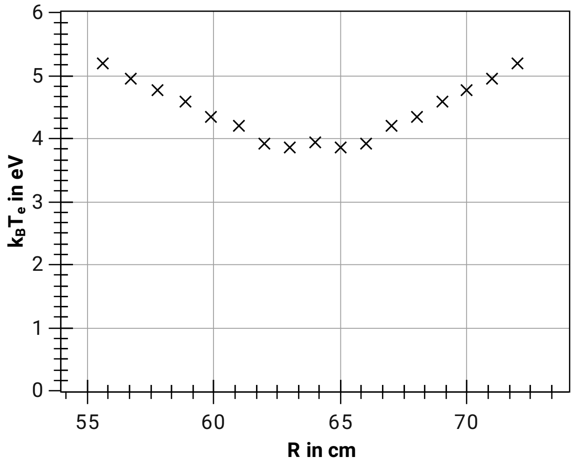

Figure 4.8.: Typical 1D profile of the thermal electron energy measured with a Langmuir probe in plasma #12151 using argon as working gas. Points below $R = R_0 \approx 63.9\,\text{cm}$ were mapped.

Typical values for TJ-K plasmas range from $k_B T_e = 1\,\text{eV}$ to $k_B T_e = 25\,\text{eV}$ depending on the plasma conditions like heating power, neutral gas pressure and gas type.

4.2.4 3D full-wave simulations for the ECE diagnostic at TJ-K

3D full-wave simulations for ECE in TJ-K were performed using IPF-FD3D [74, 86]. For these simulations, the vacuum vessel is modeled as an ideal torus. Except for a single cylindrical outer port with the radius of 125 mm further extrusions like the pump port or windows are neglected. Through this port, a Gaussian wave with beam parameters from the antenna optimization (see section 4.3.1) is injected. The wave propagation is calculated on two staggered three-dimensional rectangular grids with a resolution of $a = 700\,\text{m}^{-1}$ grid points in each direction. This corresponds to 14 electric field values and 14 magnetic field values per component and wavelength at 15 GHz. After 80000 time steps (2859 wave periods at 15 GHz) the calculations are stopped in a state that is well equilibrated. Waves that re-enter the antenna port are absorbed which models an ideal antenna. Full-wave simulations are performed for 15 GHz which is also the frequency mainly used in the measurements, as well as 14 and 14.9 GHz. For the investigation of its influence, simulations with the electron density from the model that was introduced in section 4.2.3 and with vacuum were performed. The beam parameters for the respective frequencies from the antenna optimization simulations are used as listed in table 4.3. For the aperture plane, the beam width and curvature of the wavefront are calculated from the beam waist values because this recreates the fields that are obtained in the antenna optimization. Furthermore, the influence of a concave-concave reflecting mirror opposite the antenna was investigated by simulating the propagation with and without the mirror. The shape of the mirror was modeled based on the curvature radii as will be described in section 4.3.2. Extending earlier simulations [75], the full 3D geometry of TJ-K including the actual beam parameters of the antenna and actual positions of the antenna and the mirror are used. Furthermore, the density model is extended to the region between the last closed flux surface and the vessel wall. Together with an increased resolution from 500 to 700 grid points per meter the simulation evaluation uses the resonant surfaces of the electron cyclotron emission and includes the bandwidth of the diagnostic. The small rotation of mirror and antenna with

respect to the horizon are neglected in the calculations.
These 3D full-wave simulations for TJ-K use the highest grid resolution that can be calculated both at the IGVP or the bwUniCluster [87]. For more details see appendix A.4.

4.2.5 Results of the full-wave simulations

The resulting patterns from microwave propagation simulations in TJ-K are plotted using VisIt [88] which can handle the large three-dimensional data. In figure 4.9 two-dimensional toroidal midplane cuts show the sensitivity pattern of the ECE diagnostic from the FD3D simulations with a 15 GHz wave with and without a mirror. A poloidal plot of the same data is shown in figure 4.10.

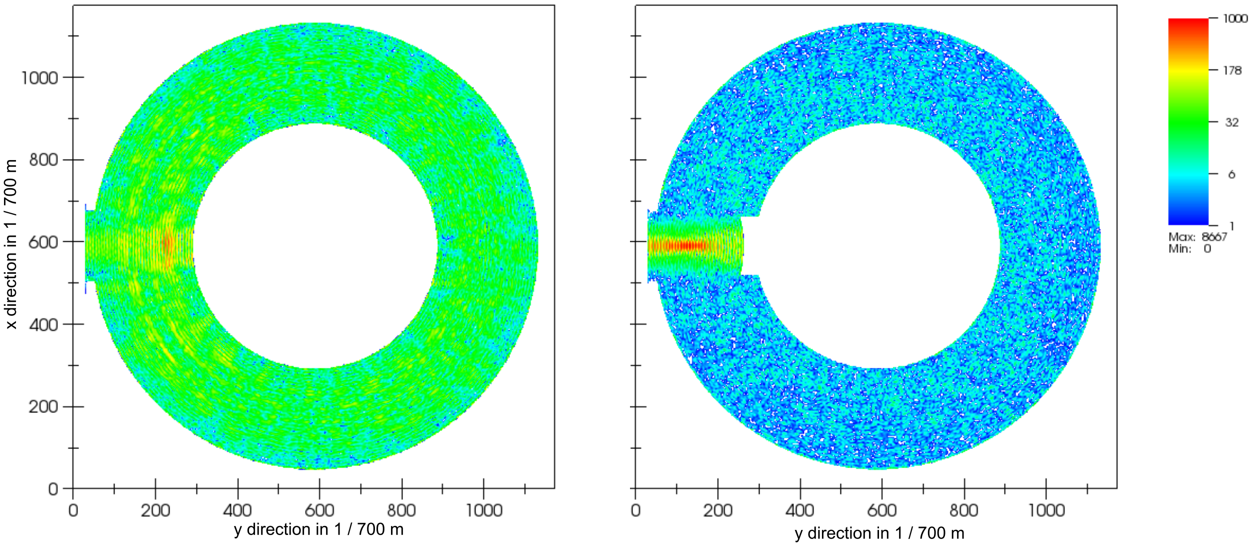

Figure 4.9.: Distribution of the time-averaged squared electric field in the toroidal mid-plane for a 15 GHz microwave that is injected from an outer port, determined in a 3D full-wave simulation for TJ-K without (left) and with mirror (right).

It can be clearly seen that the mirror restricts the volume that is visible to the antenna as much less electric field energy is distributed in the torus. Especially in the poloidal cross-sections that are shown in figure 4.10, a vertical and toroidal restriction of the microwave propagation can be seen in the case shown on the bottom of the figure where the mirror is used. For a quantitative evaluation, the time-averaged squared electric fields in the antenna region, defined as a cylindrical prolongation of the port up to the inner wall, are summed and normalized by the sum over the entire torus. Since ECE with a fixed frequency is only emitted around the resonant surface for this frequency, the results are limited to this surface using the shape function Φ_2 from eq. (4.5). Furthermore, only regions with electrons contribute to the signals, such that the resonance layer is additionally weighted with the local electron density. The resulting local contributions $Q^{(i,j,k)}$ at grid point (i, j, k) to the total Q, defined by

$$Q := \sum_{i,j,k} \underbrace{\langle E^2 \rangle_T \, n_e \int_{f-b/2}^{f+b/2} \Phi_2(f') \mathrm{d}f'}_{=:Q^{(i,j,k)}}, \tag{4.22}$$

are shown in figure 4.11 for a receiver bandwidth of 1 GHz.

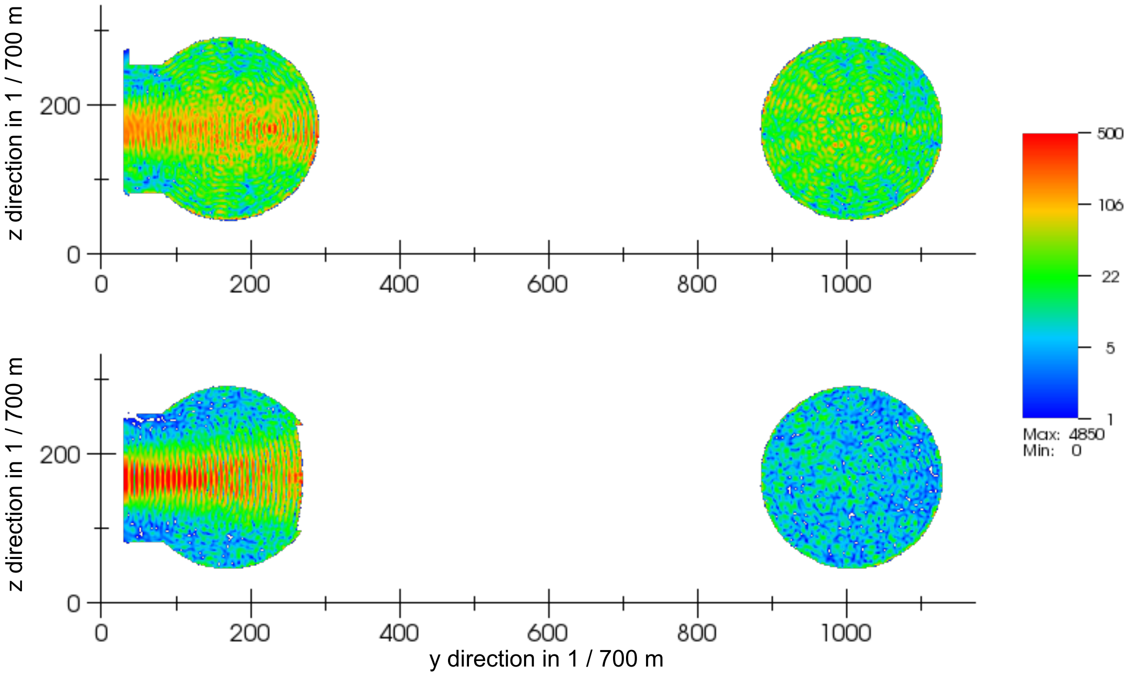

Figure 4.10.: Distribution of the time-averaged squared electric field in the poloidal plane at $\phi = 90°$ and $\phi = 270°$ for a 15 GHz microwave that is injected from an outer port, determined in a 3D full-wave simulation for TJ-K without (top) and with mirror (bottom).

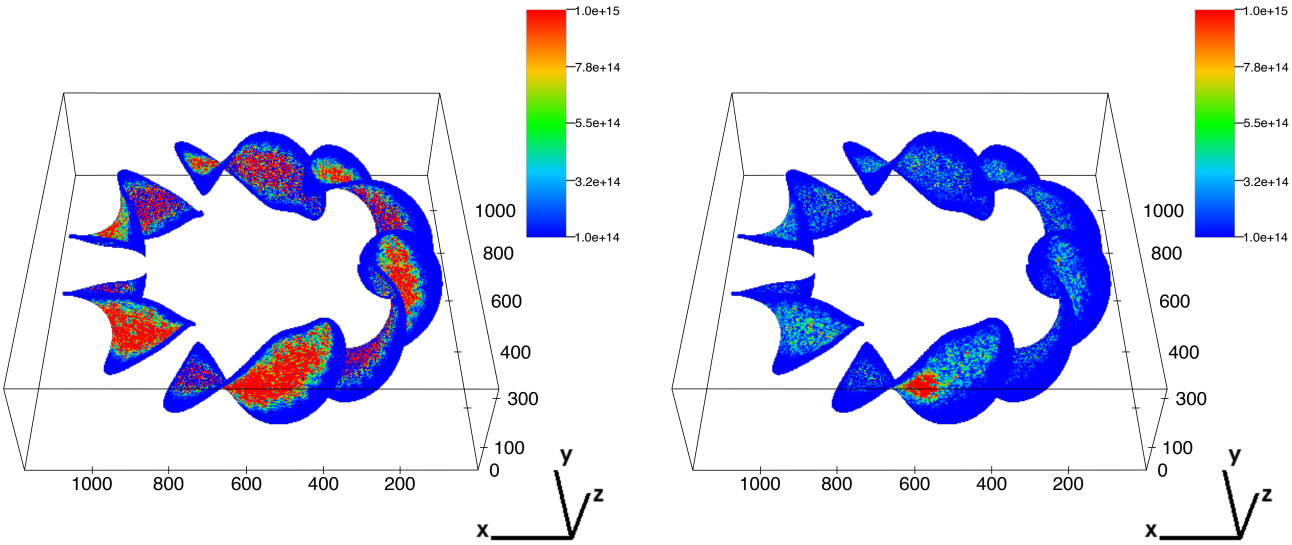

Figure 4.11.: Perspective 3D view on the contributions $Q^{(i,j,k)}$ to the ECE signals in arbitrary units as calculated in 3D full-wave simulations for 15 GHz. The axes' tick labels are in grid point units, where 700 grid points correspond to 1 m. In the foreground, the contribution directly in front of the antenna located in the center of the xz-plane is shown. On the left, only the toroidal vessel with realistic density and magnetic field was used while on the right the concave-concave mirror opposite the antenna was added.

The resonant surfaces appear, due to the six windings of the helical field coil, as six surfaces with a twisted chip-like shape. There is no connection between the surfaces and they are extremely thin: depending on the temperature and the measurement bandwidth, the shape function (equation (4.5)) and the magnetic field gradient determine their width. As there is an upper limit to the simulation resolution at 700 grid points per meter, a bandwidth of at least 100 MHz has to be used for the TJ-K magnetic field in the evaluations to get surfaces of Q that are resolved in the simulations. The measurement bandwidth of only 3 MHz is too small to be examined in the simulations. Therefore, evaluations are done for the cases of the minimum required bandwidth for the simulations, $b = 100\,\text{MHz}$, and as reference the approximate bandwidth for measurements with a microwave diode, $b = 1\,\text{GHz}$. With these two bandwidths, it is possible to see whether b influences the results strongly. Without a mirror all six resonant surfaces contribute significantly to the measurements as can be seen in the left plot of figure 4.11 where all surfaces are mainly red (values above $8 \cdot 10^{14}$ a.u.) with blue rims (below $3 \cdot 10^{14}$ a.u.). When a reflecting mirror opposite the antenna is used that changes the wall curvature from convex-concave to concave-concave, strongly enhanced localization can be seen. The red regions in the right plot are not only restricted to the surface between mirror and antenna but predominantly to its center. Table 4.2 lists the numerical results of the evaluation for the different simulation setups and diagnostic bandwidths with the sum for the entire torus Q_{tor} and the portion in the cylindrical continuation of the port Q_{ant}.

f in GHz	mirror	$\frac{Q_{ant}}{Q_{tor}}(b = 100\,\text{MHz})$	$\frac{Q_{ant}}{Q_{tor}}(b = 1\,\text{GHz})$
14.0	☑	25.5 %	21.0 %
14.0	☐	7.2 %	6.8 %
14.9	☑	23.7 %	19.6 %
14.9	☐	7.4 %	7.2 %
15.0	☑	21.1 %	17.4 %
15.0	☐	7.6 %	7.1 %
15.0 (vac)	☑	34.0 %	29.7 %
15.0 (vac)	☐	11.2 %	10.8 %

Table 4.2.: Ratio of the signal contributions Q from the volume between antenna and inner wall compared to the entire torus for different frequencies and geometries with (☑) and without (☐) mirror.

The fraction $\frac{Q_{ant}}{Q_{tor}}$ quantifies the localization of the measurement signal in front of the antenna. As expected, all variants show an increased localization when a mirror is used. For 15 GHz the improvement factor is about 2.8, for the other simulations about 3. An influence of the evaluation bandwidth can be seen for the cases with the mirror but without a mirror the bandwidth plays a less important role. When the results with $b = 100\,\text{MHz}$ are considered in comparison to 1 GHz, in each case a decrease of the localization with increasing bandwidth can be seen. Although 15 GHz and 14.9 GHz are close together, the simulation results are as different as between 14 and 14.9 GHz. This shows that the actual ratio depends strongly on the position of maxima and minima in the standing wave pattern compared to the resonance layer of the ECE frequency and therefore also on the position of the mirror and antenna. The bottom rows (“vac”) of the table show the results for propagation without a plasma. The formal evaluation for vacuum propagation is from a cyclotron emission point of view pointless as

no emitting electrons are present but it can be used to estimate the effect of the beam broadening and curvature distortion (compare section 4.3.2) due to the plasma. The 15 GHz case shows that the plasma significantly accounts for the distribution of the beam into the torus by broadening the beam. This leads to a drop from 34 % to only 21 % in the case with a mirror.
Overall, with plasma only about 7 % of the measurement signal is expected to come from the plasma in front of the antenna which can be increased to about a fifth to a quarter when a mirror is installed. Therefore, despite the simplification of the vessel shape of the TJ-K model the simulations are of great value since the beneficial effect of a mirror has clearly been demonstrated. The design of a microwave mirror for TJ-K's ECE diagnostic is described in section 4.3.2. In an iterative process, the data of the mirror optimization and of the antenna optimization from section 4.3.1 was used in the simulations presented here. Still, this evaluation neither includes absorption, emissivity and radiation transport nor the influence of density fluctuations due to turbulence. A further possibility to increase the localization is addressed in section 4.3.3 where the mirror is used for the setup of a diagnostic resonator.

4.3 Design of microwave components

4.3.1 Optimization and characterization of an ECE antenna

In applications with frequencies higher than 1 GHz [80] horn antennas are often used to couple freely propagating waves to waveguides or the other way around. Very common is the use of rectangular waveguides operated only with the fundamental mode meaning that half a wavelength fits into the longer direction of the rectangular waveguide while not even half a wavelength fits into the shorter direction. A horn antenna can be described as a waveguide that is gradually opening such that the wave in emitting operation is gradually guided to free space until the end of the horn. Simple horn antennas use a constant opening angle along the propagation axis. Such a horn antenna is easy to manufacture as all parts can be made out of metal planes. In TJ-K, microwaves from the plasma are collected using a radially symmetric horn antenna that ends in a circular waveguide. Compared to rectangular horns, such an antenna can be easily manufactured with a variable opening angle which is used to create a very pure mode. The ECE horn shape has been optimized using the simulation package PROFUSION [89] for maximum purity of the Gaussian mode in broadband operation, where the purity is defined as the ratio of the power in this mode compared to the total power. This means that the emission of the antenna is simulated and its field distribution in the aperture is compared to a Gaussian distribution. In an optimization scheme [90], the difference between the present field and the desired one for all simulation frequencies is used in the cost function. This cost function is minimized in the optimization by variation of the parameters of Chebysheff polynomials that model the antenna radius along the propagation axis. The antenna is connected to a monomode rectangular WR62 waveguide with dimensions 1.58 cm × 0.79 cm that is attached to the antenna after a transition. Because of the waveguide mode and the small circular diameter after the rectangular-to-circular transition, at this end a TE11 waveguide mode is the only possible mode at the antenna flange. The shape of the electric field lines of this mode is illustrated in figure 4.12. The TE11 mode has a vertical polarization and an elliptical shape of the absolute electrical field like shown in figure 4.13.

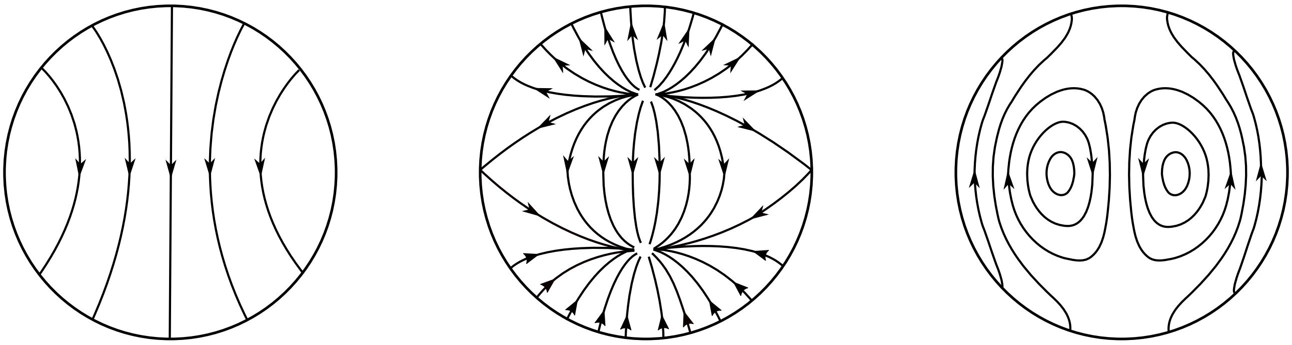

Figure 4.12.: Electric field line structure of the TE11, TM11 and TE12 (from left to right) circular waveguide modes, reproduced after [91, 92].

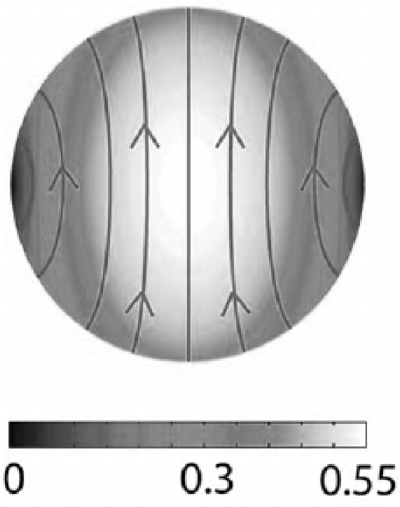

Figure 4.13.: Electric field lines and absolute electric field in arbitrary units of the TE11 circular waveguide mode, from [92].

By variation of the antenna radius a part of the wave is converted to other modes. The optimization scheme ensures that the mainly generated modes are an appropriate fraction of the TM11 mode, a small part of the TE12 mode and sufficiently low fractions of other modes. Already a comparison of the field line patterns of the TE11 and TM11 mode in figure 4.12 shows that the combination of them works towards a Gaussian field because the upper and lower end of the ellipsoidal field are reduced.

In the case of the ECE antenna, the frequency range from 10 GHz to 20 GHz, a full octave, is used for the optimization to cover the frequency range of the second harmonic ECE at an outer port of TJ-K as listed in table 4.1. The resulting emission beam pattern implicates a Gaussian weighting in the antenna aperture of incoming microwaves as sending and receiving antenna characteristics are equal [81](see chapter 4.2.2). For comparison, an optimization for a narrow bandwidth antenna is performed. As a constraint, the length of the horn antenna is limited to the length of an outer port of TJ-K plus a port extension tube, in total 28.0 cm. The resulting reference antenna that is optimized only in the $12 - 13\,\text{GHz}$ range, has a higher mode purity up to 12.5 GHz but for frequencies above it performs much worse than the broadband ECE antenna as can be seen in figure 4.14.

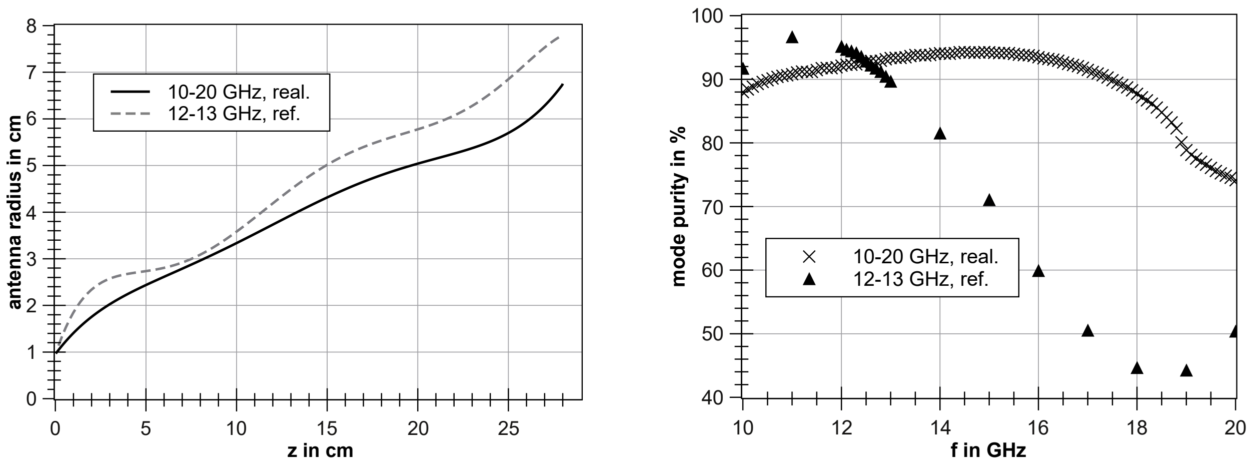

Figure 4.14.: Optimized shape of the ECE antenna (solid line) and a reference antenna optimized in the 12-13 GHz range (dashed line) on the left and simulated mode purity on the right.

The ECE antenna shows in the simulations a broadband mode purity above 90 % from 10.6 up to 17.4 GHz, peaking at 14.7 GHz with 94.3 % purity. The resulting antenna with the shape shown in figure 4.14 was finally manufactured at the IGVP workshop. Further drawings and antenna data are available in figures A.1 to A.2 in the appendix. The front which is facing the plasma is made from non-magnetic stainless steel (1.4429) that can stand heat loads from TJ-K plasmas and does not perturb the magnetic field significantly. For weight reduction and easier manufacturing the rear part with its minimum radius of 9.68 mm that is connected to a commercial circular-to-rectangular waveguide transition (FLANN 17643) is made out of aluminum. From the rectangular WR75 port of the transition, the waveguide size is reduced to a rectangular WR62 waveguide with dimensions 1.58 cm × 0.79 cm using a taper to fit the subsequent waveguide setup.

PROFUSION also delivers the parameters of the Gaussian beam that the antenna emits. This includes the size and position of the beam waist for each simulated frequency both in the vertical and horizontal plane of the emitted wave as listed in table 4.3.

f in GHz	$w_{0,hor.}$ in cm	$w_{0,vert.}$ in cm	$z_{0,hor.}$ in cm	$z_{0,vert.}$ in cm
14.0	3.67	3.89	-11.97	-19.89
14.9	3.61	4.00	-13.22	-20.51
15.0	3.60	4.03	-13.36	-20.61

Table 4.3.: Beam parameters as obtained from the antenna optimization and used in the full-wave simulations. The beam waist in horizontal direction (perpendicular to the emitted $\vec{E}$) $w_{0,hor.}$ and vertical direction (parallel to the emitted $\vec{E}$) $w_{0,vert.}$ and the distances of the waist from the aperture $z_{0,hor.}$ and $z_{0,hor.}$ along the propagation axis are shown. All beam waists are within the antenna.

This information was used to investigate the ECE propagation and the antenna sensitivity regions in section 4.2.1. After manufacturing, the antenna field was measured in transmitting operation in order to test its performance. A Wiltron 68337B signal generator was used to feed the antenna via a short rectangular coax-coupler, a waveguide taper and the rectangular-to-circular transition. The emitted microwaves were then detected with a small rectangular microwave horn at a sweeping arm with a distance of 137 cm between the ECE antenna aperture and the center of the receiver antenna. Angular sweeps with parallel polarization directions of the receiving antenna and the emitting ECE antenna were performed with 1° angular resolution in the horizontal plane for 10-18 GHz in 2 GHz steps. The signal power at the receiver horn was measured with an HP70001A spectrum analyzer that consists of an HP70600A preselector, HP70905B radio frequency section, HP70900A local oscillator, HP70902A intermediate frequency section and an HP70206A displaying unit. For all frequencies, the antenna patterns shown in figure 4.15 have a clearly dominant lobe centered at 0° which is directly along the antenna axis.

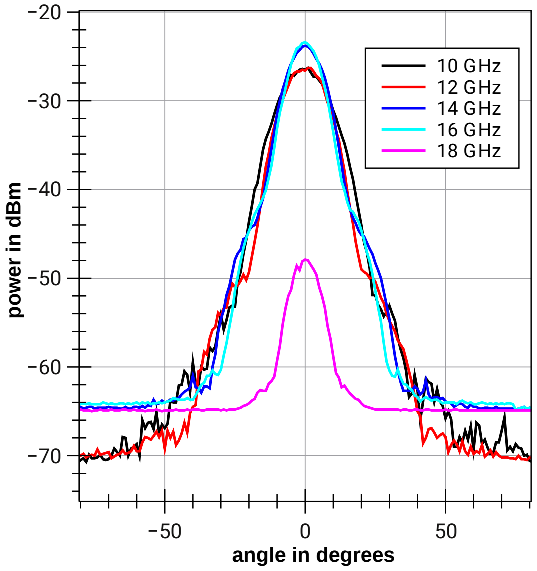

Figure 4.15.: Measured ECE antenna patterns in the horizontal plane.

Until far more than 10 dB below the main lobe no significant deviations from Gaussian behavior are seen. The behavior for 10 and 12 GHz is similar as well as the results for 14 and 16 GHz while the pair at higher frequencies shows a narrower angular distribution with a higher peak. The peak powers and lobe widths are listed in table 4.4.

f in GHz	peak power in dBm	FWHM
10	-26.5	16.8°
12	-26.3	14.7°
14	-23.9	12.6°
16	-23.4	10.9°
18	-48.0	10.4°

Table 4.4.: Main lobe power and width of the ECE antenna at different frequencies.

The beam width measured as FWHM decreases with increasing frequency at about 1° per GHz for 10 to 16 GHz. For 18 GHz the antenna performs much worse showing low power signals and less angular symmetry. The power at 0° was measured in a wider frequency range from 8 to 19.5 GHz in smaller steps. As can be seen in figure 4.16, from 10 to 16 GHz the antenna performs well but above 16.5 GHz a strong decrease of the signal power in the center is present, with its minimum at 18 GHz.

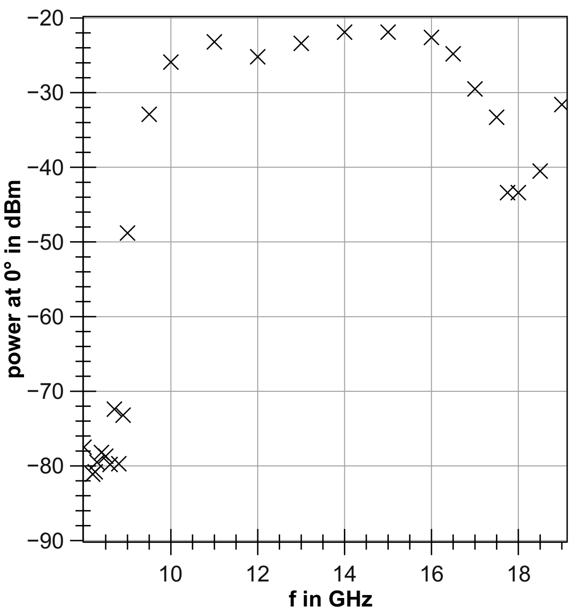

Figure 4.16.: Maximium power of the main lobe for different frequencies measured with parallel polarization of the ECE and receiving antenna.

Also frequencies below 10 GHz show much less power down to the detection limit of -80 dBm for frequencies around 8 GHz. In this range not only the circularly symmetric antenna has to be considered but the waveguide components connected to the antenna contribute substantially to the frequency trends. The rectangular waveguides are designed for usage in the frequency band from 12.4 to 18 GHz at the coaxial coupler (WR62) and 10 GHz to 15 GHz at the circular-to-rectangular coupler (WR75). Therefore, the suppression of signals below 10 GHz and above 16 GHz is expected.

In total, the measurements suggest the usage of the ECE antenna system between 10 and 16 GHz since in this range the angular symmetry is maintained and the main lobe power does not vary with the frequency. Furthermore, the suppression of 8.256 GHz signals compared to the operation range is more than 55 dB which makes it possible to use this system with its dynamic range for the operation at TJ-K with heating power at 8 GHz in the kilowatt range and second harmonic ECE in the femtowatt to picowatt power range. Note that the suppression of low frequencies is likely to be even much stronger since the low-frequency results are all at the sensitivity limit of the measurement equipment.

In another setup, the polarization selectivity of the ECE antenna with the attached waveguide was tested. A linearly polarized wave was emitted by a horn antenna and the signals received by the ECE antenna were measured in polarization parallel to the emitting antenna and perpendicular to it. The received signal power differed by more than 30 dB between the two orientations. Thus the polarization selectivity of the combination of antenna and monomode waveguide is suitable for polarization measurements. The remaining signal in the perpendicular case can easily be caused by alignment inaccuracies, ambient reflections and polarization mixing in the sending and receiving antenna.

4.3.2 Optimization of an in-vessel mirror

The results of the full-wave simulations (section 4.2.5) show that a mirror at the inner vessel wall can change the convex-concave curvature (compare figure 3.3) of the reflecting surface at the high-field side to a concave-concave curvature in a way that the localization of the ECE measurements is improved by a factor larger than 2.8. In order to adapt the mirror curvature to the operation in TJ-K with plasma which influences the propagation of electromagnetic waves resulting in a change of the phase fronts of a microwave beam, 2D full-wave simulations are performed. The Gaussian mode that is emitted by the optimized antenna (section 4.3.1) is simulated for five frequencies in the second harmonic ECE range in the plane of the electric field of the wave and the plane of the magnetic field with their individual beam waists and waist positions. Despite the small 14° tilt of the magnetic field compared to the horizon in the experiment (see also section 3.3), the E-plane is approximated by the vertical poloidal plane and the H-plane by the horizontal toroidal plane in this simplified model. Simulations are performed once in a vacuum and then with a simplified plasma model: in the poloidal plane, the plasma is modeled with circular symmetry while in the horizontal plane the plasma is implemented as slabs disregarding the slight toroidal curvature in the experiment. Both profiles have a Gaussian density distribution that drops to exp(−1) of its peak value of $\hat{n}_e = 7 \cdot 10^{17}\,\mathrm{m}^{-3}$ at a radius of 11 cm. For reference, the curvature radii of the Gaussian beam are also calculated analytically at the mirror position for the case of a vacuum propagation. Contour plots of the electric wave field of the results like those shown in figure 4.17 were used to estimate the curvature radii from the full-wave simulations.

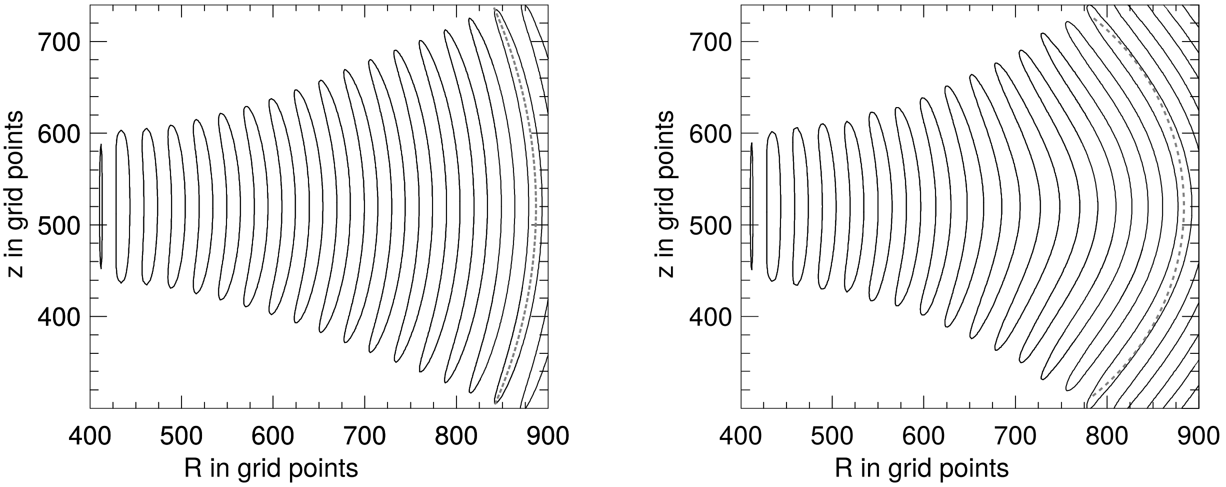

Figure 4.17.: Electric wave field contour plot showing the wavefront curvature at the mirror position in the vertical plane with adjusted circles (dashed) for the evaluation. Simulation in vacuum (left) and with plasma (right).

As indicated with dashed lines the wavefront curvature was approximated circularly. For vacuum propagation the wavefront curvature is circular but with plasma, the shape is noticeably changed. Therefore, only an intermediate estimate of the radius can be given as the curvature radius is then a very local variable. Because the strongest fields are in the beam center, this region needs to be weighted more strongly in the approximation. The dashed lines in figure 4.17 show that with plasma agreement is only possibly very close to the center. For the simulated frequencies and planes, the results are summarized in the graphs of figure 4.18. Analytical and numerical results are in good agreement and in the horizontal plane also the curvature radii with plasma show no strong influence of the plasma because the slab geometry in this plane produces no lens effect. In the poloidal plane much stronger curvatures occur in the beam center, i.e. the curvature radii between 0.27 m and 0.45 m are smaller than in the horizontal plane.

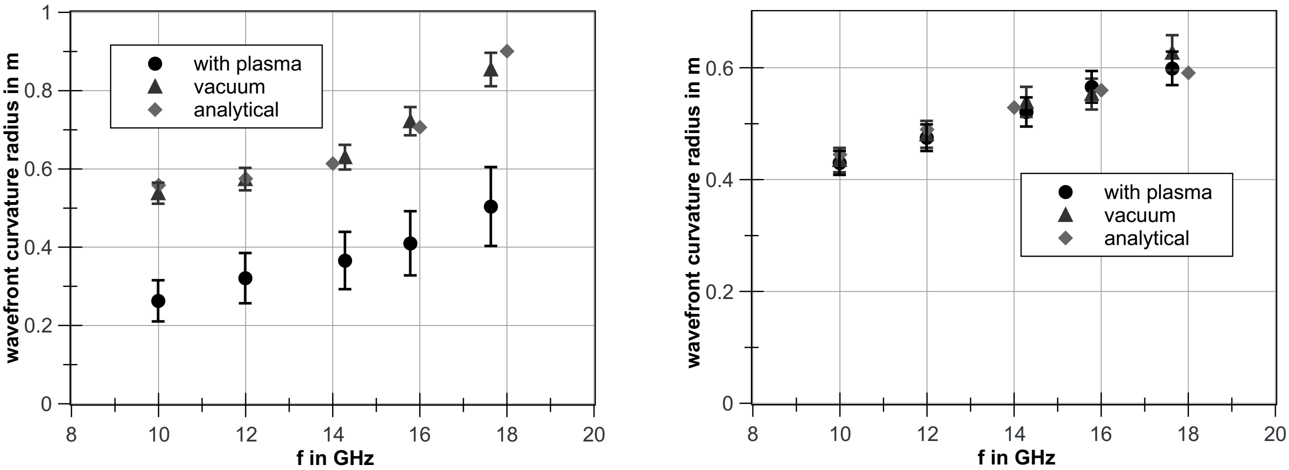

Figure 4.18.: Phase front curvature radii resulting from full-wave simulations in the vertical (left) and horizontal (right) plane with analytical calculation as a reference for the vacuum case.

As the mirror is supposed to work well with various electron densities and ECE frequencies, the intermediate vertical curvature $R_{vert} = 45\,\text{cm}$ and horizontal curvature $R_{hor} = 50\,\text{cm}$ are chosen for the construction of the mirror. For the capture of a large amount of radiation from the plasma, the mirror diameter should be chosen as large as possible. The space between the plasma and the vessel wall limits the diameter as the mirror should not disturb the plasma. Because of the flexible current ratios that can be used at TJ-K a range of plasma positions is available that should all be compatible with the diagnostic system. As mirror diameter, 20 cm was chosen to account for all plasma positions including a safety margin. The mirror with the two optimized curvatures has been constructed, built from non-magnetic stainless steel and installed in the TJ-K vessel. A schematic of the mirror and antenna installed in the vessel is shown in figure 4.19. Engineering drawings are attached as figure A.4 to A.5 of the appendix.

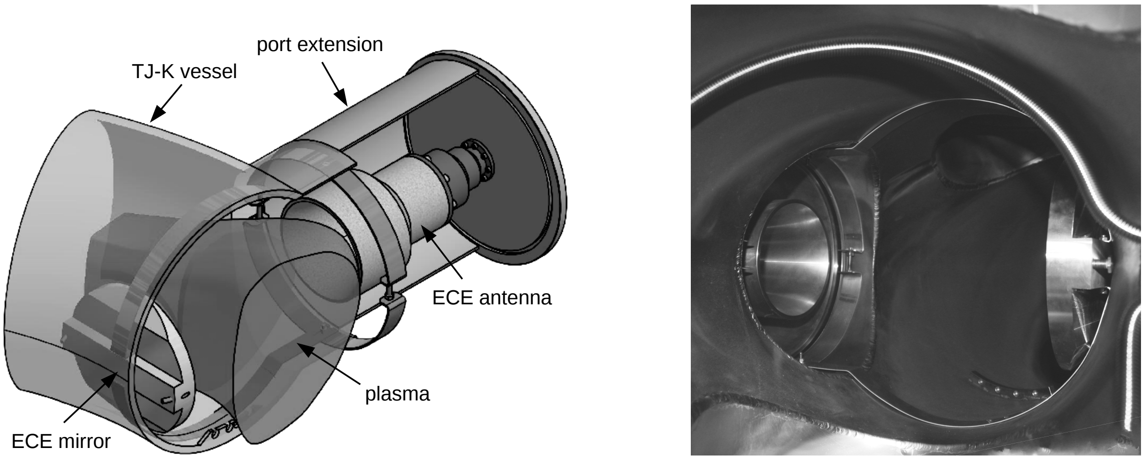

Figure 4.19.: Schematic view of the in-vessel components of the ECE diagnostic system at TJ-K shown in a torus section. On the right, a photograph of the diagnostic is shown.

The mirror is installed with a tilt angle of −14 ° which accounts for the tilt of the magnetic field on the magnetic axis at the center of an outer port in TJ-K. No modification to the vacuum vessel was needed due to a flexible clasp mount fixing the mirror in the port and the toroidal vessel. A repositioning of the ECE diagnostic to another outer port is therefore easily possible. Three screws at the back of the mirror mount can be used for alignment in the vessel.

4.3.3 Design of a tunable resonator

Although the results of the full-wave simulations in section 4.2.1 have shown that the localization of the ECE measurements is improved when the in-vessel mirror is used, still only 21 % to 26 % are expected to originate in front of the antenna. A further enhancement is possible by means of a resonator setup that leads to multiple passes of the ECE through the region between mirror and antenna. The coupling to and from the toroidal vessel stays the same for each pass but in the toroidal vessel the losses for the microwaves are much larger than in the resonator due to the long paths and many reflections. Thus the field enhancement in the resonator can lead to an enhanced localization of the measurements. As the space in the vessel is limited, a tunable resonator with a reflector outside the vessel is designed which has the benefit that it can be tuned during the operation of TJ-K. The setup used as a resonator for measurements is sketched in figure 4.20.

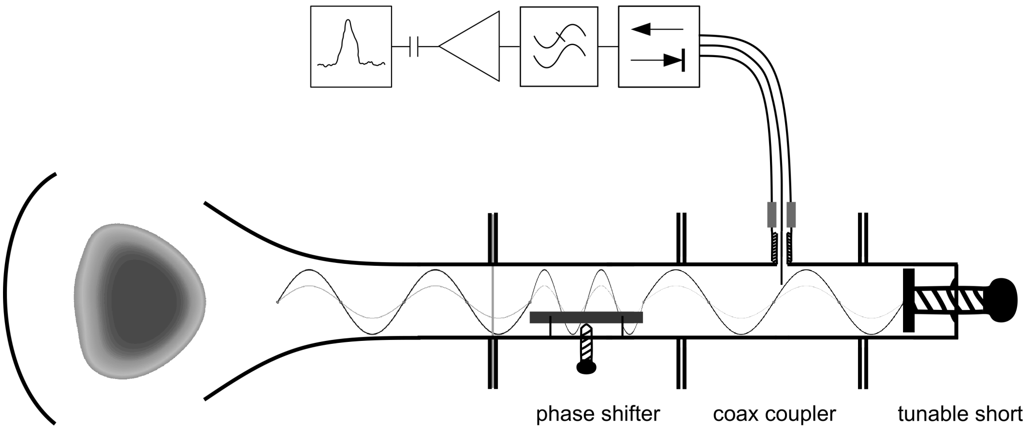

Figure 4.20.: Schematic vertical cut of the tunable resonator setup with mirror left from the plasma, antenna on the right, followed by a vacuum window, phase shifter, the coax coupler and the tunable short. In the waveguide, the standing wave pattern is shown that is formed by the incoming and reflected wave. The coaxial cable leads to the isolator, the low pass filter, followed by amplifiers and the spectrum analyzer.

The effective resonator length needs to be tunable in order to reach resonance for the frequency that is currently measured. At the same time, the coupling from the resonator to the measurement equipment has to be adjusted to set the power extraction at this point which in turn partly determines the resonator quality. The designed resonator works as follows:

In the vessel, the ECE mirror already reflects the microwaves and thus acts as one end of the resonator. At the other end, the efficiently coupling commercial waveguide-to-coax adapter is replaced by a partly reflecting component to increase the reflections and complete the resonator. A tunable coupler was constructed for this purpose. As schematically shown in figure 4.21, it consists of a tunable short, which is basically a movable reflecting plate, and a pin that probes the electric field in the waveguide and is connected to a coaxial cable.

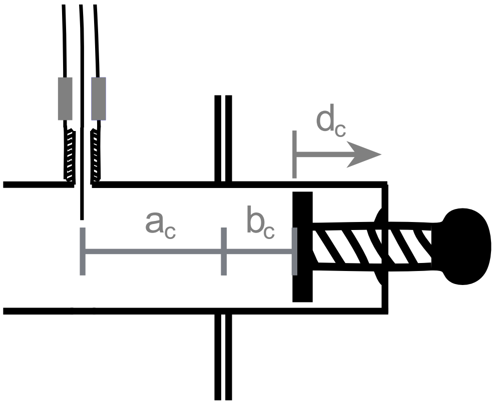

Figure 4.21.: Schematic of the tunable coupler. The distance from coupling pin to flange is $a_c = 1.78\,\text{cm}$ and the distance from the neutral position of the movable wall to the flange is $b_c = 5.27\,\text{cm}$.

By moving the tunable short the distance between reflecting wall and coupling pin is changed. Therefore, the location of the coupling pin with respect to the standing wave pattern that is generated by the superposition of incoming and reflected wave is changed. Commercial couplers are optimized for a good coupling from the waveguide to the cable (and backward). With a distance of a quarter of the wavelength in the waveguide λ_{wg} between coupling pin and the final wall of the waveguide, incoming and reflected wave have a difference in traveling distance of $\lambda_{wg}/2$. The resulting phase shift from the path length difference is π. Additionally, a reflection at a wall comes with a phase shift of π, resulting in a total shift of 2π which leads to constructive interference at the pin and maximal coupling to the coaxial cable. In practice, the distance between pin and wall of a commercial coupler is optimized for the entire frequency band that the waveguide is designed for and therefore the distance is only approximately $\lambda_{wg}/4$ for the used frequency. The tunable short can be used to adjust the distance such that the field at the pin is set. Therefore, coupling and reflection can be selected.

A setup with an antenna fed by the Wiltron 68337B generator is used to measure this tunable coupler. The microwaves are captured with an antenna and the signals that are coupled to a coaxial cable are measured with the HP70001A spectrum analyzer. Compared to a commercial ATM 62-251A-6 coupler, -20dB are detected when the pin is in the node of the standing wave pattern. The maximum of the commercial coupler is also reached with the tunable coupler when the pin is in the antinode of the standing wave. The tunable short is moved with a micrometer caliper with a 1/10 inch scale and 1/1000 inch subticks. Since the waveguide wavelength is 2.58 cm at 15 GHz in a WR62 waveguide, the subticks correspond to $9.8 \cdot 10^{-4} \approx 1/1000$ waveguide wavelengths allowing for fine tuning of the coupler. A minimal signal at the analyzer was found for the position $d_c = 0.280"$ at 15 GHz. In this case, the distance between wall and coupling pin is 7.83 cm which is the sum of the coupler position and the distance between pin and neutral position of the reflecting plate. This total distance corresponds to $3.03 \cdot \lambda_{wg}$. The phase shift between incoming and reflected wave is therefore $2 \cdot 3.03 \cdot 2\pi + \pi = 13.12\pi$ at the pin which is approximately 1 % away from the expected phase shift for destructive interference. The accuracy of this result is limited by the noise level of the analyzer which limits the minimum signal strength that can be measured. As the measurement of ECE needs signals above the noise power of the detection system, the short was tuned with a plasma until a signal of 10 dB above the noise was reached. This is found already at the position $d_c = 0.299"$ which is at $\Delta\varphi \approx 13.22\pi$ while the next maximum is expected at 14π.

The tunable coupler can be used to set the desired amount of reflection and coupling but it also changes the total length between the ECE mirror and the movable wall at the other end of the resonator. In order to adjust the total resonator length to the used frequency and reach the resonance, the change of the position of the wall needs to be compensated for. A Waveline 708c phase shifter is installed in the waveguide between vacuum window and coax-coupler to achieve this. It consists of a dielectric plate that can be positioned in the waveguide using an adjusting knob. The phase speed of the microwave in the waveguide is decreased by the dielectric dependent on the position of the plate. This shortens the effective wavelength in this region which makes it possible to tune the resonance frequency of the resonator. With this phase shifter, the effective length of the resonator can be finely tuned as the calibration in appendix A.5 confirms. For all frequencies in the range for the WR62 waveguide far more than 180° of phase shift can be reached which is enough to find both the resonant and destructive position in all cases. The phase shifter can also be used during a plasma shot to compensate for the change of the wavelength that is caused by the refractive index of the plasma.

In total, the resonator can be tuned in its degree of coupling and therefore loss using the tunable short and the resonance is tuned by the effective length that is adjusted with the phase shifter. Thus the resonator quality is mainly limited by the losses in the vessel like microwaves leaving the resonator due to the limited mirror diameter. As a resonator is sensitive also to small input signals, an isolator is used in the coaxial system. The isolator strongly damps any signal that is directed towards the waveguide system.

To estimate the losses due to the limited mirror size and antenna aperture as well as the mirror curvature three-dimensional simulations of the mirror and antenna as a resonator are performed. To simplify the simulations, the antenna is also modeled as a mirror at the antenna aperture with the antenna aperture as size and the curvature that corresponds to the phase distribution in the aperture. A 15 GHz wave is emitted right in front of the antenna and the power flow forward and backward is detected in front of both mirrors in this model with numerical directional couplers. With this method, it can be evaluated how much power is reflected by the mirror compared to the incoming power. In simulations without plasma, the ECE mirror reflects 88 % of the power. Because the microwave beam is smaller at the antenna aperture, the antenna can capture and reflect 95.5 % even though it is smaller than the ECE mirror. With these factors, the power decay in the resonator can be estimated by multiplication of the initial power with the reflection factors for each pass in the resonator. The power $P(i)$ after i passes is

$$P(i) = P(0) \cdot (88\,\% \cdot 95.5\,\%)^{i}\,, \tag{4.23}$$

when no power source is present. The power decay time can be estimated by consideration of the speed of light and the resonator length. In this model, the power in the ECE resonator decays to $\exp(-1) \approx 36.8\,\%$ in 5.5 passes which means after the sixth reflection at the ECE mirror. The corresponding decay time is 22 ns. When the 0.5 m of waveguide and the reduced waveguide group velocity [93] $v_g = c \cdot \frac{\lambda}{\lambda_{wg}}$ are taken into account, the energy decay time increases to 43 ns. In this model, the resonator decay time is governed mainly by the loss at the ECE mirror. Simulations with different mirror curvatures show only a minor influence on the resonator quality. Thus, a larger mirror is desirable but the space between the torus and the plasma is already exploited by the current mirror.

For experimental examination of the quality factor, the diagnostic resonator is placed on an optical table. Through a small hole in the mirror center, a small dipole antenna is inserted as sender. With the Wiltron signal generator and a microwave diode, the resonator's quality factor is investigated. The tunable coupler is set to the coupling position $d_c = 0.299"$ that is also used in the ECE measurements at TJ-K. By means of a fast square modulated signal from the generator, the decay time of the signal in the resonator can be measured. The resulting signal from the diode is shown in figure 4.22.

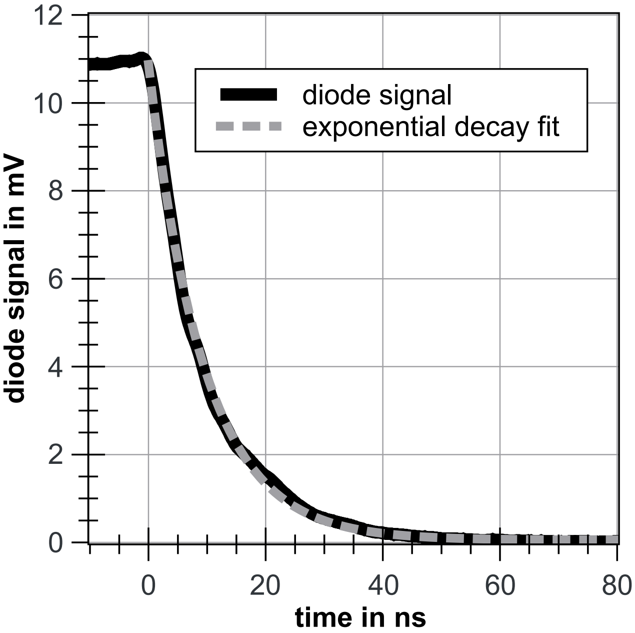

Figure 4.22.: Time trace of the diode signal from the diagnostic resonator with the coupler set to position $d_c = 0.299"$ when the input signal to the resonator is modulated. The signal is averaged over several modulation periods.

The exponential fit function that is also shown in the figure has the form

$$U(t) = U_A \cdot \exp\left(\frac{(t - t_0)}{t_{dr}}\right), \tag{4.24}$$

with the switching point t_0, amplitude U_A and the decay time $t_{dr} \approx 9.4\,\text{ns}$ for the diagnostic resonator. The measured power decay time of the diagnostic resonator is about 22 % of the time determined in the simulation. Consequently, the losses in the real resonator are larger which is expected because the waveguide components, phase shifter, tunable short and outcoupled signal as well as possible misalignments were not included as loss mechanisms in the 3D simulation.
From the measured decay time the diagnostic resonator quality factor q_{dr} is calculated as follows:

$$q_{dr} = t_{dr} \cdot \omega \approx 886. \tag{4.25}$$

In addition, the decay time in the vacuum vessel without the ECE diagnostic resonator is measured with two antennas at different windows of TJ-K. The measured time trace and an exponential fit are shown in figure 4.23. In this measurement, the decay is not monomode as the vessel acts as a multimode resonator. The exponential decay fit curve implies a decay time of $t_{TJK} \approx 65\,\text{ns}$ for the vacuum vessel. The quality factor of TJ-K is therefore about 6.8 times larger than the quality factor of the diagnostic resonator:

$$q_{TJK} \approx 6.1 \cdot 10^3. \tag{4.26}$$

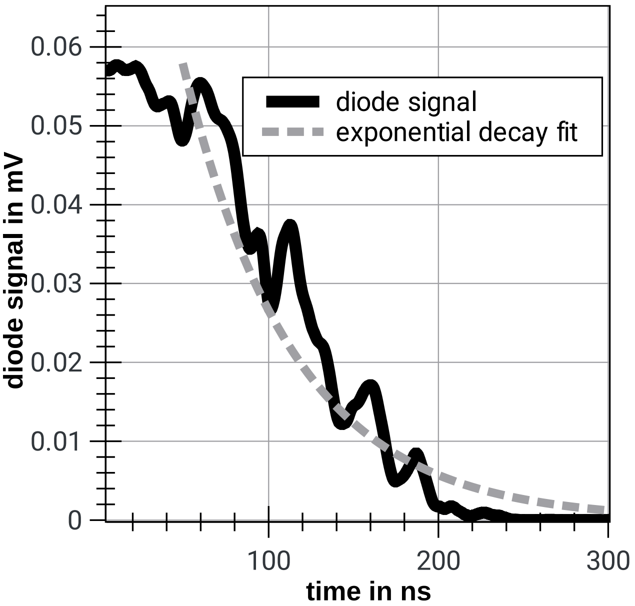

Figure 4.23.: Time trace of the diode signal from the vacuum vessel when the input signal is modulated. The signal is averaged over several modulation periods.

A model to calculate the order of magnitude of the quality factor of the vacuum vessel as resonator is described by Jackson [94]. The quality factor can be calculated from the energy storing volume, the entire torus volume

$$V_t = 2\pi^2 r_0^2 R_0 \approx 0.36\,\mathrm{m}^3,$$

and the energy dissipation volume which is modeled as the torus surface

$$A_t = 4\pi^2 r_0 R_0 \approx 4.15\,\mathrm{m}^2,$$

multiplied with the skin depth

$$\delta = \sqrt{\frac{2}{\mu\sigma\omega}}, \tag{4.27}$$

which is the depth that the electromagnetic radiation with angular frequency ω penetrates a wall with magnetic permeability μ and electric conductivity σ. For the stainless steel 316L that is used as wall material of TJ-K, the material constants are $\mu \lesssim 1.02 \cdot \mu_0$, with the vacuum permeability μ_0, and $\sigma \approx 1.35 \cdot 10^6\,\mathrm{S/m}$ [95] leading to a skin depth of about $3.5\,\mu\mathrm{m}$. The resulting quality factor is [94]:

$$q_{TJK} = \frac{\mu_0}{\mu}\frac{V_t}{A_t\delta}, \tag{4.28}$$

where an evacuated cylindrical geometry was assumed neglecting port openings and installations. The generalized formula for the quality factor includes a geometry factor that is of the order of 1 and therefore not relevant for the estimate of the order of the quality factor. For the vessel of TJ-K and a 15 GHz microwave a quality factor of about $2.4 \cdot 10^4$ is obtained which is approximately 4 times larger than the value obtained by the time measurement.

The resonator quality factors can be used to estimate the localization of the measurements. As the irregular pattern in the torus shown in figure 4.9 illustrates, the vessel is a multimode resonator that can be treated statistically. The number of modes in the torus with the measured quality factor $q_{TJK} \approx 6.1 \cdot 10^3$ is [96]

$$N_m = \frac{8\pi V_t}{\lambda^3 q_{TJK}} \approx 186. \tag{4.29}$$

Approximately two thirds of the modes, 124, are populated by ECE as it is emitted in the two dimensions perpendicular to the background magnetic field. The diagnostic resonator is a selective monomode resonator such that it can only couple to one mode efficiently. Consequently, only 1/124 of the ECE power from the torus contributes to the measurement signals. Local evaluation of $n_e \Phi_2$ with $b = 100\,\mathrm{MHz}$ (compare section 4.2.5) shows that only 5.3 % of the electrons emitting at 15 GHz are in the diagnostic resonator.

Furthermore, the power enhancement in the resonators has to be considered. In the diagnostic resonator, the resonance enhancement factor $\frac{P_{dr}}{P_0}$ can be calculated from the quality factor $q_{dr} \approx 886$ [97]:

$$\frac{P_{dr}}{P_0} = \frac{1}{(1 - r_{dr})^2}, \tag{4.30}$$

where r_{dr} is the effective reflection coefficient for one round trip in the diagnostic resonator and can be obtained from the quality factor by solving

$$q_{dr} = f T_{dr} \frac{\pi \sqrt{r_{dr}}}{1 - r_{dr}}, \tag{4.31}$$

with the round trip time $T_{dr} \approx 8\,\mathrm{ns}$. The resulting enhancement factor is

$$\frac{P_{dr}}{P_0} \approx \frac{1}{(1 - 0.655)^2} \approx 8.4. \tag{4.32}$$

In the multimode torus, the enhancement factor is calculated statistically. The average path length from the energy decay time in the torus, $c \cdot t_{tjk}$, compared to the typical length in the resonator $\sqrt[3]{V_t}$ results in the typical number of passes through the emitting region and thus the enhancement factor:

$$\frac{c \cdot t_{tjk}}{\sqrt[3]{V_t}} \approx \frac{19\,\mathrm{m}}{0.7\,\mathrm{m}} \approx 27. \tag{4.33}$$

When the resonance enhancement, the high number of modes in the torus and the number of emitting electrons in the volumes are considered, the fraction of the measured ECE power originating in the diagnostic resonator is given by

$$\frac{8.4 \cdot 5.3\,\%}{\frac{1}{124} \cdot 27 \cdot 94.7\,\% + 8.4 \cdot 5.3\,\%} \approx 68\,\%. \tag{4.34}$$

This localization is mainly caused by the selectivity of the monomode resonator that rejects most of the ECE from the multimode torus. Compared to the values for 15 GHz obtained from the simulations in section 4.2.5, the diagnostic resonator improves the localization by a factor of 3.2 over the geometry with ECE mirror and 9 compared to the case without mirror. With the diagnostic resonator the measurement signals are expected to be mainly determined by the local ECE.

All values in this section should be understood as estimates for the size of the quantities. Especially the statistical values, the enhancement in the torus and the number of modes, underlie several assumptions but even a uncertainty of 20 % would affect the calculated localization factor by only 5 percentage points. The conclusions drawn from the model used are insensitive to this degree of uncertainty.

4.4 Distinction from thermal bremsstrahlung

Microwave emission from TJ-K plasmas in the second harmonic ECE frequency range could in principle also be generated by thermal bremsstrahlung. The dominant mechanism contributing to the emission can be investigated by use of the different dependencies on the electron density and electron temperature that ECE and bremsstrahlung show. In the following, two different methods are introduced to investigate the origin of the microwave emission. Finally, measurements at TJ-K are presented that are used to identify the emission mechanism.

4.4.1 Methods to identify the electron cyclotron emission

Dependence of the emitted power on the electron temperature and density

The number of electrons that gyrate around the magnetic field lines directly affects the ECE power that is emitted as the electrons move and emit independently. Also, the electron temperature influences the emitted power in a frequency range: when the gyration of a single electron is modeled as two perpendicular periodic linear motions as described in section 4.1.1, higher temperatures lead to higher velocities that can be understood as a stronger current in two perpendicular dipoles. Therefore, the emitted ECE power increases with higher temperatures. In equation (4.6), the dependence on density and temperature can already be seen: the emitted power P_2 from the second harmonic ECE per plasma volume V in a frequency interval $\mathrm{d}\omega$ and a solid angle $\mathrm{d}\Omega$ is proportional to the density and the squared temperature:

$$\frac{\mathrm{d}^2 P_2}{V \mathrm{d}\omega \mathrm{d}\Omega} \sim n_e T_e^2. \tag{4.35}$$

Thermal bremsstrahlung is also emitted in the frequency range between 10 and 20 GHz when the electrons are deflected at ions. The spectrum of bremsstrahlung is limited by the kinetic energy of the electrons: photon energies up to the entire kinetic electron energy can appear. When the entire kinetic energy of the electron is converted to a photon, the maximum bremsstrahlung frequency is reached:

$$f_{max} = \frac{m_e v^2}{2h}, \tag{4.36}$$

where h is the Planck constant. Due to the frequency depending on the impact parameter, i.e. the virtual distance of a transit without deflection, the spectrum of bremsstrahlung is continuous and ends at the maximum frequency given by equation (4.36). For plasma diagnostics there is also a lower frequency limit given by the resonances and cutoffs shown in figure 4.3 since bremsstrahlung that is detected on the outside has to be transmitted through the plasma [3]. When a plasma with a Maxwell-Boltzmann velocity distribution (see also section 5.1.3) is considered, also a few very fast electrons can be present that extend the emission spectrum to high frequencies. But due to their low number, long collision times and the additional dependence on the impact parameter very low powers in this part of the spectrum are expected. Therefore, the interesting frequencies are in the bulk of the velocity distribution. For plasmas with thermal energies of 10 eV the most probable velocity is

$v_{th} \approx 1.9 \cdot 10^6\,\mathrm{m/s}$ which would lead to $f_{max} \approx 2 \cdot 10^{15}\,\mathrm{Hz}$. Because this frequency is far above the ECE range, emission by thermal bremsstrahlung in the measurements cannot be eliminated using this energy comparison. Hence, the density and temperature dependence of the emitted bremsstrahlung is examined and compared to the relation for the second harmonic ECE.
For bremsstrahlung, the emitted power P_b is proportional to the electron density because the number of encounters is determined by the number of available electrons. In the same way, the ion density understood as the number of deflection centers affects the emitted power. In singly ionized plasmas like in normal TJ-K operation, both densities are similar which can be expressed as a squared electron density dependence of the emitted power. The electron temperature also influences the bremsstrahlung by determining the collision time. The effective collision time for electron-ion encounters becomes longer with higher electron velocities which results in the emitted bremsstrahlung decreasing with the electron temperature. The resulting power dependence is given by [3]:

$$\frac{\mathrm{d}^2 P_b}{V \mathrm{d}\omega \mathrm{d}\Omega} \sim \frac{n_e^2}{\sqrt{T_e}}. \tag{4.37}$$

For small $\mathrm{d}\omega$ the detected power is approximated by the same dependence but for large bandwidths the power is proportional to $\sqrt{T_e}$ since then the integration over $\mathrm{d}\omega$ changes the behavior. By integration of the full power dependence with typical TJ-K parameters using the bandwidth of the ECE diagnostic $b = 3\,\mathrm{MHz}$, the temperature dependence for bremsstrahlung was investigated numerically. The results shown in figure 4.24 are in agreement with the $1/\sqrt{T_e}$ regression which is also plotted.

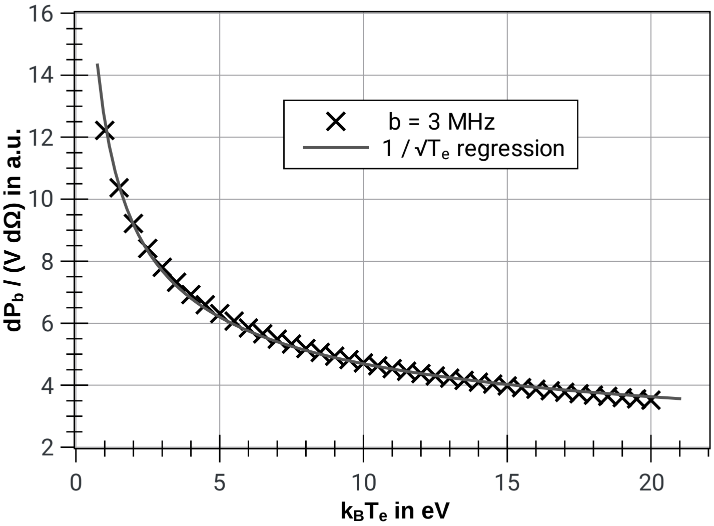

Figure 4.24.: Calculated temperature dependence of the power emitted by bremsstrahlung in the temperature range of TJ-K with 3 MHz bandwidth.

For a constant setup with a fixed measurement bandwidth $b = 3\,\mathrm{MHz}$ and a fixed antenna setup, the volume V, the frequency element $\mathrm{d}\omega$ and the angular element $\mathrm{d}\Omega$ can be omitted in proportionality considerations. Then the very different density and temperature dependencies of bremsstrahlung, $P_b \sim n_e^2/T_e^{1/2}$, and second harmonic ECE, $P_2 \sim n_e T_e^2$, provide a handy tool to discriminate between the two processes. Within the bandwidth of the ECE diagnostic, the power that reaches the antenna can be measured directly. In order to check experimentally the dependence, the electron density and temperature need to be obtained independently from the microwave power measurement by other diagnostics.

Heating power modulation experiments

As a second method for the identification of the microwave generation mechanism, heating power modulation experiments are employed. The signal from the function generator that feeds the klystron is modulated with an internal square wave in order to switch the microwave injected into the vacuum vessel on and off periodically. When the microwave is turned off, the plasma receives no further energy but losses due to collisions and radiation remain. Therefore, the temperature of the plasma decreases on the time scale of the energy confinement time τ_E. Also, the losses of particles due to recombination and diffusion remain while no new ionizations take place. Therefore, also the density of the plasma decreases on the time scale of the particle confinement time τ_n. For typical TJ-K plasmas the confinement times were shown by earlier measurements and simulations to be in the ranges [98]:

$$\tau_n \in [0.3; 1.6]\mathrm{ms}$$

$$\tau_E \in [10; 260]\mu\mathrm{s}.$$

Since the energy confinement time is much shorter than the particle confinement time it is possible to examine the temperature dependence of a diagnostic signal before the density changes by means of heating power modulation experiments. For a constant density, a decreasing temperature leads to a rapidly decreasing ECE due to its quadratic temperature dependence whereas the power from bremsstrahlung should increase by the $T_e^{-1/2}$ dependence.

4.4.2 Measurement results

Measurements of the emitted microwave power from a variety of plasmas were performed for a fixed frequency of 14.5 GHz with the ECE antenna and the concave-concave mirror. Simultaneous recordings of Langmuir characteristics at $(R = 61.6\,\mathrm{cm}, z = 0\,\mathrm{cm}, \phi = 30°)$, which is a position on the flux surface where the 14.5 GHz is emitted, and interferometer measurements provide information about the electron temperature and density, respectively. With this information, it is possible to investigate the relation between the emitted power and the electron temperature and density. Figure 4.25 shows the received power on a linear scale over the temperature and density dependence for ECE or bremsstrahlung. In the case of proportionality, the measurement data will be found on a straight line. The graphs include results from 71 different plasmas covering different gas types, heating powers and neutral gas pressures such that the generated electron densities range from $1 \cdot 10^{17}\,\mathrm{m}^{-3}$ to $1 \cdot 10^{18}\,\mathrm{m}^{-3}$ and the thermal electron energies are between $3.6\,\mathrm{eV}$ and $14.3\,\mathrm{eV}$. For both cases, a linear regression is shown as a black line.

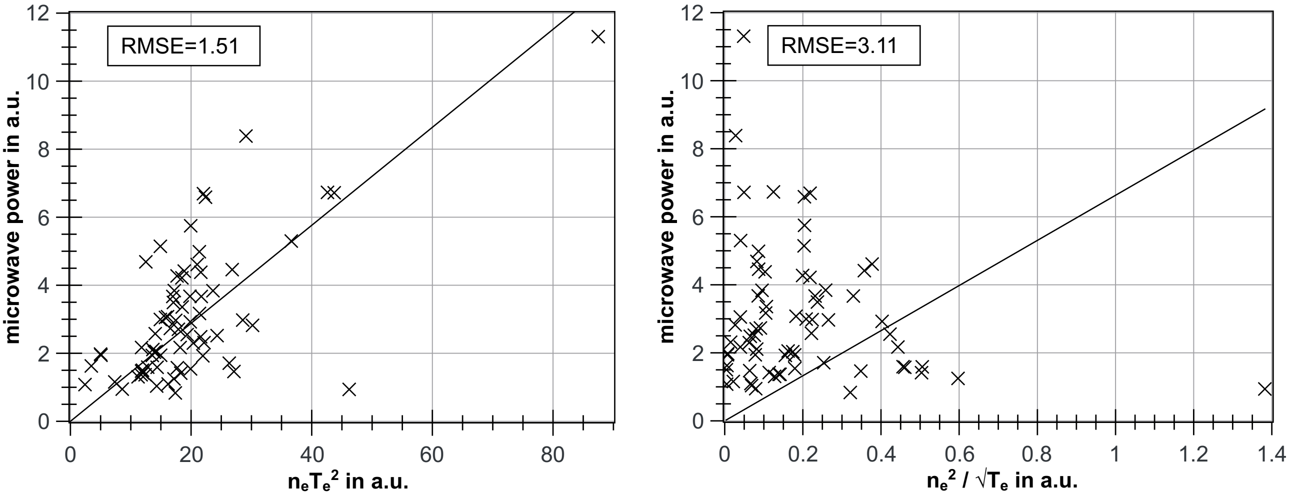

Figure 4.25.: Received microwave power at 14.5 GHz of 71 different plasmas over the density and temperature dependence as predicted for the second harmonic ECE ($P_2 \sim n_eT_e^2$, left) and bremsstrahlung ($P_b \sim n_e^2/\sqrt{T_e}$, right). Linear regressions are shown as black lines and the root mean squared error (RMSE) is indicated.

As the high number of evaluated plasma discharges leads to a dense cloud of measurement points the same data is shown in figure 4.26 represented as mean value with the standard deviation as error bars for intervals of the microwave power which makes it easier to see the scaling behaviors. The points without error bars represent single points within an interval where no deviation is defined.

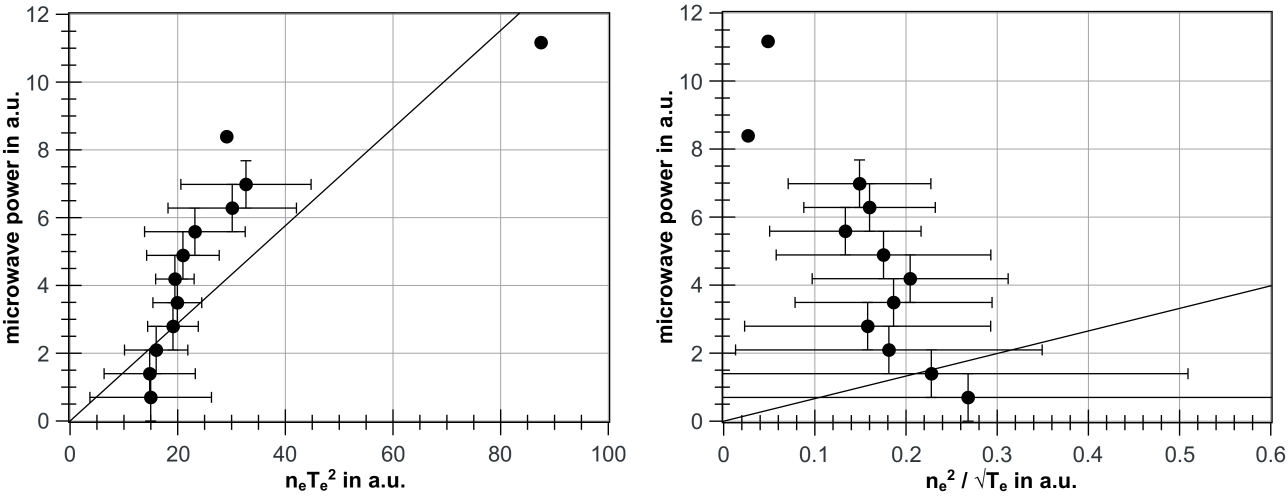

Figure 4.26.: Mean and standard deviation of the received microwave power at 14.5 GHz of 71 different plasmas over the density and temperature dependence as predicted for the second harmonic ECE ($P_2 \sim n_eT_e^2$, left) and bremsstrahlung ($P_b \sim n_e^2/\sqrt{T_e}$, right), evaluated in microwave power intervals.

No linear dependence on $n_e^2/\sqrt{T_e}$ can be seen whereas the results show a dependence close to $n_eT_e^2$. This is confirmed by a much lower root mean squared error (RMSE) between measurement and regression for second harmonic ECE than for thermal bremsstrahlung where the wide error bars also indicate the large deviations. Therefore, bremsstrahlung is not the dominant physical effect of the emission and as the only further emitting mechanism in this frequency range is ECE, the ECE nature is hereby confirmed. Nevertheless, the RMSE for ECE is still quite high as the results are scattered around the line in figure 4.25. The scattering is believed to be caused by the limited localization when only a mirror without the resonator setup as described in section 4.3.3 is used. The resonator setup was not yet available when these measurements were performed.

The temperature dependence of the microwave emission in the frequency range of the second harmonic ECE was also investigated in heating power modulation experiments. The microwave power of the klystron was modulated using a square wave with a repetition rate of 400 Hz. The signals of the interferometer, the ion saturation current, the microwave emission and the optical diode are recorded and evaluated for the investigation. The optical diode and the ion saturation current of a Langmuir probe at $(R = 0.66\,\mathrm{m}, z = 0\,\mathrm{m}, \phi = 30°)$ show the temperature behavior as long as the interferometer still confirms a constant density. As a typical example, the time traces recorded from shot #12450 are shown in figure 4.27.

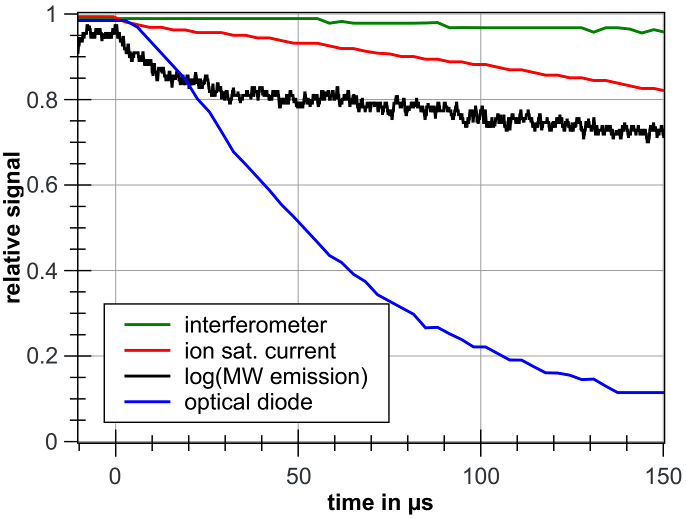

Figure 4.27.: The turn-off phase in the heating power modulated shot #12450 is plotted. Shown are the 15 GHz emission, the interferometer, ion saturation current of a Langmuir probe and the optical diode signal, all relative to their maximum value. Averaged over 256 modulation periods.

In the first $50\,\mu$s after the heating is turned off the interferometer signal does not change significantly, although the interferometer has a time resolution of about $10\,\mu$s. Therefore, the line-averaged density is constant but the ion saturation current, the optical emission and the microwave emission decrease notably. As a result, the emitted microwave power is shown to decrease with decreasing temperature as the diode and the ion saturation current indicate the fast decrease in the electron temperature during constant density. Compared to the emissivity of ECE (eq. (4.35)) and bremsstrahlung (eq. (4.37)) this means that the measured microwave emission cannot be generated by bremsstrahlung from the optically thin plasma because then the emitted power would have to increase at turning off.

Both methods, the power modulation experiments and the evaluation of the dependence on the electron temperature, confirm that the measured microwave emission is generated by second harmonic ECE rather than thermal bremsstrahlung.

4.5 Polarization of ECE

Electromagnetic waves emitted by a gyrating electron are linearly polarized: the direction of the radiated electric field is perpendicular to the background magnetic field, which is called X-polarization. Measurements of ECE directly propagating to the antenna, therefore, should show polarized signals and a polarization-sensitive receiver antenna should be aligned to it. Measurements of large volumes with different magnetic field directions or depolarizing effects can remove this property. Depolarizing effects are discussed for TJ-K in the following. As they depend on the propagation path in the vessel and plasma, the degree of polarization in the measurement signals can indicate the quality of localization of the measurements.

4.5.1 Theory of depolarizing effects in TJ-K

Electromagnetic waves traveling in a magnetically confined plasma experiment experience changing refractive indices, a variety of magnetic field orientations and many different metallic surfaces where the waves are reflected. A magnetic field in a plasma can cause a change of the polarization of an electromagnetic wave by the Faraday effect and the Cotton-Mouton effect [99]. The case with a magnetic field parallel to the propagation direction of the electromagnetic wave is called the Faraday effect which rotates the polarization around the propagation direction. A magnetic field perpendicular to the propagation direction is needed for the Cotton-Mouton effect that leads to an elliptization of the polarization. The Faraday effect and the Cotton-Mouton effect are only special cases of the general change of the polarization in matter with a magnetic field. In the most general case, the polarization components are elliptical and the propagation direction is arbitrary compared to the magnetic field. In this case the Faraday component of the polarization rotation and the Cotton-Mouton effect interplay due to the change of the projections of the electric field which are needed for either effect. When the linearly polarized cyclotron emission is described as a superposition of a left-handed and a right-handed elliptically polarized wave, the change of the polarization of the ECE can be understood. Different phase velocities for the left-handed and the right-handed component appear because of the different response of the electrons in a magnetic field leading to a phase shift. The shifted components result in a rotation of the polarization direction. A polarization ellipse with variable definitions is illustrated in figure 4.28.

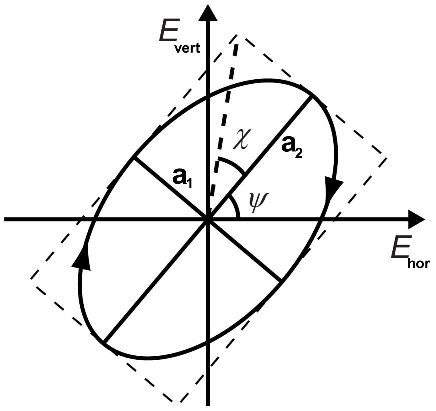

Figure 4.28.: Polarization ellipse with the definitions of the angles and axes. The electric field vector rotates on the ellipse perpendicular to the propagation direction. Modified from [99].

The polarization orientation is described by the angle ψ of the long axis of the ellipse with respect to the horizon on that the E-field vector rotates and the elliptization angle $\chi := \arctan(a_1/a_2)$, with the short semiaxis of the ellipse a_1 and the long semiaxis a_2. The ratio a_1/a_2 determines the degree of ellipticity. A general description of the development of the polarization is available when the polarization is expressed using the Stokes vector $\vec{u}$ that is defined as [99]

$$\vec{u} := \begin{pmatrix} \cos(2\chi)\cos(2\psi) \\ \cos(2\chi)\sin(2\psi) \\ \sin(2\chi) \end{pmatrix}. \tag{4.38}$$

The third component describes the ellipticity: when it vanishes the wave is linearly polarized ($\chi = 0$) and when the third component is ± 1 ($\chi = \pm\pi/4$) the wave is circularly polarized (+ right-hand, − left-hand). The other components determine the direction of the polarization: horizontal or vertical in the case of linear polarization or the alignment of the ellipse in the other cases. A plasma with its electrons and magnetic field rotates the Stokes vector on an abstract sphere, the *Poincaré sphere*, changing the type and direction of the polarization along the propagation path s according to [99]

$$\frac{\mathrm{d}\vec{u}}{\mathrm{d}s} = \frac{\omega_{pe}^2\omega_{ce}^2}{2c\omega(\omega^2-\omega_{ce}^2)} \begin{pmatrix} (B_x^2-B_z^2)/B^2 \\ 2B_xB_y/B^2 \\ 2(\omega/\omega_{ce})B_y/B \end{pmatrix} \times \vec{u}(s), \tag{4.39}$$

written for a wave propagating outwards along R central at O5 of TJ-K where y is the propagation direction. As a consequence, the field components perpendicular to the propagation direction influence the third component of the Stokes vector and change the ellipticity (Cotton-Mouton effect). The magnetic field along the major torus radius R changes the other two components of $\vec{u}$ which includes the rotation of the polarization as in the Faraday effect. A change in the polarization therefore is dependent on the direction of the magnetic field, its strength, the direction of the polarization, the frequency and the density. Especially the complicated magnetic field geometry but also the 3D density can rather be handled by 3D full-wave simulations than analytically. Different regions of the extended microwave beam experience different field vectors and densities such that their polarizations do not only rotate or become elliptical but the overall beam is no longer described by one common polarization. This reduces the degree of polarization and can finally lead to the complete depolarization of the radiation. Whether the Cotton-Mouton effect or the Faraday effect dominates depends on the details in the geometry and both can influence each other by changing the polarization themselves.

Another aspect that has to be considered concerning the polarization of microwaves in a vacuum vessel are reflections at walls [100]. The electric field of an incoming electromagnetic wave E_{0i} that is reflected at a plane wall can be decomposed into a linearly polarized component parallel to the plane of incidence (p-polarized) and a perpendicular one (s-polarized). After the reflection both reflected components E_{0r} stay in the original direction but their amplitudes change dependent on the angle of incidence according to the Fresnel equations with elimination of the refraction angle by insertion of the law of refraction:

$$\left(\frac{E_{0r}}{E_{0i}}\right)_s = \frac{N_1\cos\alpha - \frac{\mu_{r1}}{\mu_{r2}}\sqrt{N_2^2 - N_1^2\sin^2\alpha}}{N_1\cos\alpha + \frac{\mu_{r1}}{\mu_{r2}}\sqrt{N_2^2 - N_1^2\sin^2\alpha}},$$

$$\left(\frac{E_{0r}}{E_{0i}}\right)_p = \frac{N_2^2\frac{\mu_{r1}}{\mu_{r2}}\cos\alpha - N_1\sqrt{N_2^2 - N_1^2\sin^2\alpha}}{N_2^2\frac{\mu_{r1}}{\mu_{r2}}\cos\alpha + N_1\sqrt{N_2^2 - N_1^2\sin^2\alpha}}.$$

In general, the relative amplitudes of the p- and s-polarized part change and therefore the state of total polarization differs after the reflection. For a non-planar mirror or a non-planar wavefront, the angle of incidence is not constant along the wavefront. Therefore, the change of polarization and the change of direction of propagation are different for fractions of the original wave in a complicated manner. Complicated mirror shapes with curvatures or roughnesses that do not fit the shape of the phase front of the incident wave can hardly be predicted analytically but numerical investigations with full-wave codes can be used to solve the complex problem.

4.5.2 Estimation of the Faraday and Cotton-Mouton effect strengths in TJ-K

Numerical investigations are conducted estimating the influence of the Faraday and the Cotton-Mouton effect on the polarization of a microwave beam in TJ-K. To illustrate the direction dependence of the Faraday effect, first a simulation in a simplified 2D geometry is conducted: a background magnetic field directed in the propagation direction of a 15 GHz microwave beam is used. The magnetic field strength is Gaussian distributed along the propagation direction with a peak value of 5 mT. A constant plasma density of $1.4 \cdot 10^{17}\,\mathrm{m}^{-3}$ is used for this example. The wave is followed from the antenna through the plasma. It is reflected and passes the plasma again. The results are shown in figure 4.29.

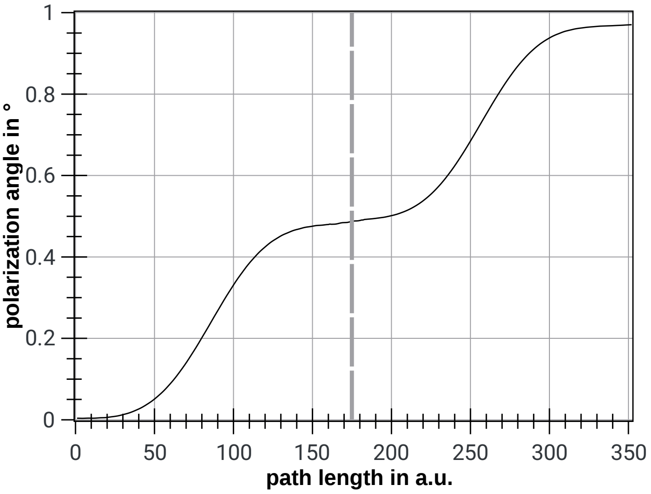

Figure 4.29.: Rotation angle of the polarization for a wave passing through a magnetized plasma and back again. The dashed vertical line indicates the reflection of the wave at 172 a.u.

The polarization vector is rotated as predicted for the Faraday effect. The change of direction on the way back does not compensate for the rotation from the initial transit but adds a further rotation in the same direction. Consequently, the rotation of the polarization in TJ-K can be expected to increase further due to multiple passes through the plasma as it occurs in the diagnostic resonator or for origins distant from the antenna. To estimate the strength of the Faraday effect in the 3D TJ-K geometry, a simulation with the density distribution and background field as introduced in sections 3.3 and 4.2.3 is performed. The simulated wave path travels along the center line of the outer port O5 which corresponds to the main path that ECE in the diagnostic resonator travels. The maximum rotation angle of the initially vertical polarized beam for one pass forth and back is only 2.9 °. The remaining electric field component in the original direction is still $\cos(2.9°) \approx 99.87\,\%$ and the measured power of a polarization sensitive diagnostic aligned to the initial direction 99.74 %. Thus, the Faraday effect is negligible for ECE in front of the antenna with only a few passes through the plasma in the diagnostic resonator. However, the effect accumulates for longer path lengths as it occurs for ECE from distant parts of the vessel.

The Cotton-Mouton effect is studied with a comparable setup launching a wave with a linear polarization with $\Psi = 45\,°$ which is a mixture of X-polarization perpendicular to the background magnetic field and O-polarization parallel to the magnetic background field. The wave is followed from the antenna along the center line of port O5 to the vessel wall. The resulting polarization ellipses are shown in figure 4.30 for ten equidistant positions along this path.

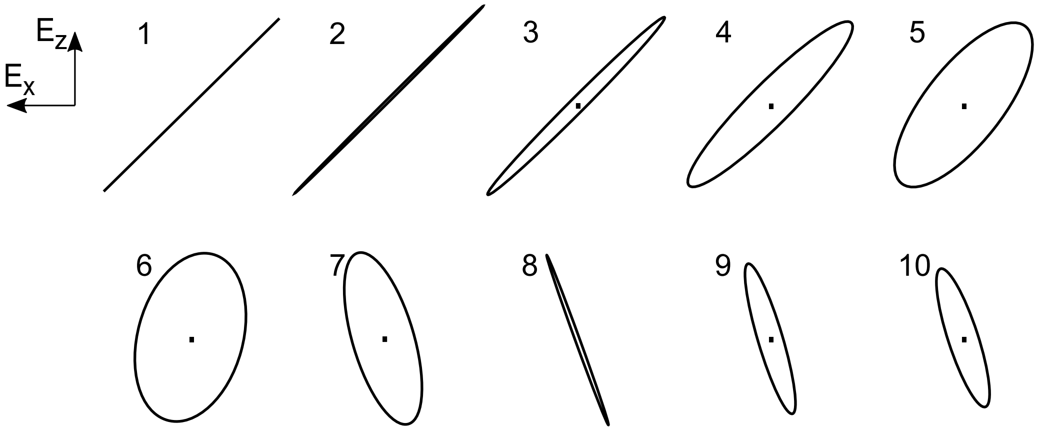

Figure 4.30.: Polarization ellipses at ten equidistant points along the path from the ECE antenna to the vessel wall. The sequence is plotted as seen from the antenna position.

The wave ellipticity starts at $\chi = 0$ when the wave is launched, reaches circular polarization with $\chi = \pi/4$ between the sixth and seventh position, passes another linear polarization and ends up with a medium ellipticity with $\chi \approx 0.07 \cdot \pi$ when the vessel wall is reached. The increased magnetic field strength towards the inner vessel wall results in a stronger change of the ellipticity seen for larger position indices. The simulation shows that the Cotton-Mouton effect is strong for the ECE frequencies in TJ-K. Nevertheless, the actual ECE originating from the diagnostic resonator in the experiment has no significant contribution of O-polarization, which is required for the Cotton-Mouton effect, such that this effect plays no role in this region.

However, the strengths of the Faraday effect and the Cotton-Mouton effect differ when the wave traverses the plasma under a different angle or at different locations. When the reflections at the vessel wall are considered, ECE that is not generated in the diagnostic resonator passes the plasma many times under different angles and with various polarizations. Therefore, together with the depolarizing effect of the reflections themselves, a complete depolarization for the ECE that travels around the torus is expected. As a consequence, details of the cyclotron emission like the directivity and polarization are concluded to be mixed for origins distant from the antenna. Especially in the experiment with ports and diagnostics inside the vessel the only polarized fraction of ECE can be expected from the plasma directly in front of the antenna. Even there, the magnetic field vector direction varies due to the twisted and curved magnetic field lines that are needed for a toroidal magnetic confinement setup.

Measurements of the polarization degree and orientation at TJ-K were performed by rotating the receiver polarization. No clear results where obtained which can be explained by the different propagation through the plasma with changed beam parameters when the waveguide that determines the polarization is rotated. Furthermore, a curvature mismatch at the ECE mirror occurs for the changed beam.

4.6 Measurement of electron temperatures from TJ-K plasmas

Finally, the designed ECE diagnostic is tested at TJ-K plasmas to obtain first electron temperatures. The final experimental setup, the calibration and the evaluation are described in the following sections.

4.6.1 Experimental setup

ECE measurements to obtain the electron temperature use the setup sketched in figure 4.20 where the optimized mirror is installed at the inner vessel wall opposite port O5. The optimized ECE antenna is positioned in port O5. The measured distance of 63.5 cm from the center of the ECE mirror to the polyimide vacuum window at the end of the antenna is in good agreement with the predicted distance of 63.3 cm, emphasizing the accuracy of the construction and installation. Microwaves that pass the antenna come to the vacuum window and are fed to a FLANN 17643 circular-to-rectangular transition that leads the microwaves from the radially symmetric antenna to the rectangular waveguides. The output from the transition is a type WR75 rectangular waveguide (see also table A.1 in the appendix). In order to protect the measurement equipment, the high power 8.256 GHz heating radiation has to be prevented from reaching the electronic components. Therefore, the waveguide is tapered down from WR75 to WR62. The cross-section of WR62 waveguides is rectangular with side lengths of $15.8\,\mathrm{mm} \times 7.9\,\mathrm{mm}$. The size of the waveguide leads to a cutoff frequency of about 9.5 GHz. This value allows the relevant frequencies of the second harmonic cyclotron frequency to be transmitted while the high power heating waves are blocked. The resonator setup is completed with the Waveline 708c phase shifter and the tunable coupler as described in section 4.3.3.

Directly at the beginning of the coaxial transmission an outer DC break INMET 8038 is used to shield the electronics from low-frequency fluctuating potentials of the vacuum vessel. The inner conductor is isolated because it ends in the waveguide air. Reflections or unwanted signals propagating from the coaxial system to the resonator in the vessel are suppressed by using an isolator directly behind the DC break. The isolator of type Quest Microwave Inc. SR0916T02 is basically a circulator that lets the measurement signal pass but diverts signals in the opposite direction to a load where they are absorbed. Isolation of at least 18 dB in the supported frequency range from 9 to 16.3 GHz is guaranteed. A low pass filter removing signals above 16 GHz has proven mandatory to suppress the second harmonic emission from the klystron which is very weak compared to the heating power (-80 dBc) but still more than 50 dB stronger than the microwave emission from the plasma. Not using such a filter leads to the saturation of the amplifiers of the ECE diagnostic and therefore falsified measurement signals also at different frequencies. Therefore, a low pass filter ZYSEN ZSLP15000-6SS that transmits signals from 0 to 15 GHz with an insertion loss below 0.9 dB but strongly damps higher frequencies follows in the measurement chain. It was constructed for TJ-K with the aim of at least 40 dB attenuation from 16.4 GHz upwards in order to filter out the second harmonic emission from the klystron. All results presented in this thesis were measured with the low pass filter in order to omit the saturation. The transfer function of the filter measured with the Wiltron 68337B generator and the HP70001A analyzer is shown in figure 4.31.

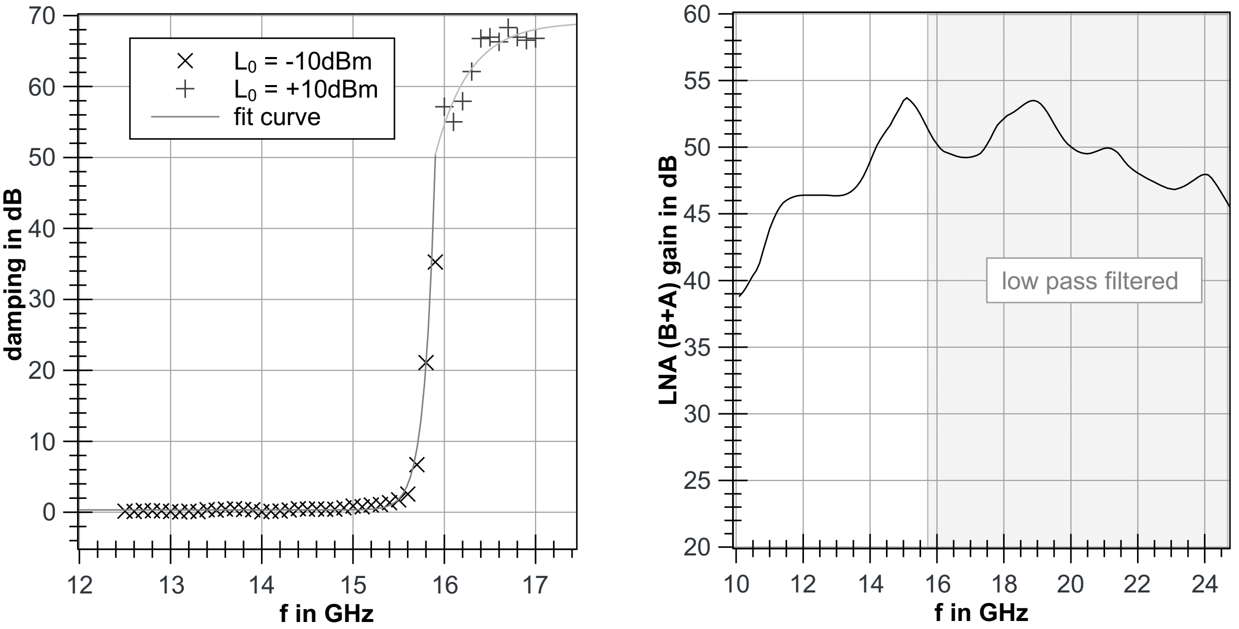

Figure 4.31.: Left: measured transfer function of the low pass filter ZYSEN ZSLP15000-6SS. The pluses were measured with a higher signal power than the crosses. The fit curve is only intended as a guide to the eye.
Right: measured gain characteristic of the cascaded LNA amplifiers. The region that will be filtered by the low pass filter in the experiments is shaded.

Up to 15.4 GHz, the damping of the low pass filter is below 1 dB but the steep region that follows leads to more than 65 dB damping for the 16.512 GHz peak from the klystron. With the low pass filter included no saturation effects of the amplifiers was observed.

The subsequent components are two low noise amplifiers LNA12g-26g by DG0VE that amplify in the frequency range in question by more than 40 dB (together), with a peak at 15 GHz with more than 53 dB amplification. The gain of these amplifiers is measured with the HP70001A spectrum analyzer and the Wiltron 68337B signal generator for both amplifiers in series with only a SMA adapter in-between. The full measured gain frequency characteristic is plotted in figure 4.31. The full width at half maximum of the highest peak is about 1 GHz which therefore is the approximate measurement bandwidth when a diode is used as detector instead of the spectrum analyzer. Finally, the amplifiers and the spectrum analyzer are separated by an INMET 8037 DC break and a 2 m Huber+Suhner SF104 cable. All used SMA to SMA adapters are $50\,\Omega$ RND 205-00455 gold-covered adapters that are rated up to 18 GHz. The HP70001A analyzer was set to measure with its maximum bandwidth of $b = 3\,\mathrm{MHz}$. A center frequency of 15 GHz is used with a span of 1 GHz and a 10 s sweep. The reference level was set to 0 dBm and the video filter set to its minimum bandwidth at 300 Hz which reduces the noise. Measurement data is acquired with a National Instruments system from the analog rear outputs of the HP analyzer[2]. The damping (insertion loss) of the measurement chain components, as well as their voltage standing wave ratios (VSWR) and amplitude reflection factors, are listed in table 4.5.

---

[2] The relation for the rear output $P_{meas}(U_{\mathrm{rear}}) = -(92.15 \pm 0.03)\,\mathrm{dBm} + (49.49 \pm 0.03)\,\frac{\mathrm{dBm}}{\mathrm{V}} \cdot \mathrm{U}_{\mathrm{rear}}$ is by a factor of 2 finer than for the front output.

component	model	VSWR	amplitude reflectivity	max. insertion loss
phase shifter	Waveline 708c	1.2	9 %	0.5 dB
isolator	Quest MW SR0916T02	1.3	13 %	0.5 dB
low pass	ZYSEN ZSLP15000-6SS	1.23	10 %	0.9 dB
DC breaks	INMET 8037 and 8038	1.35	15 %	0.5 dB
SMA cables	Huber+Suhner SF104, 2 m	1.25	11 %	2.6 dB
SMA adapter	RND 205-00455	1.125	6 %	1 dB

Table 4.5.: Insertion losses and reflection parameters of the resonator components.

Reflections at components or connections prevent an ideal standing wave in contrast to the tunable short in the resonator. Partial reflections only change the amplitude of node and antinode partly, expressed as their ratio in the VSWR. The power reflection coefficient is only 1 % when 10 % of the amplitude is reflected because of the squared dependence on the amplitude. Still, the need for the isolator is clear when the sensitivity of interference in a resonator is considered. From table 4.5 it can be estimated that up to 10 dB of losses are possible for the transfer from the coupler to the analyzer, including several cables and adapters.

4.6.2 Liquid nitrogen calibration

The measurement system is calibrated using two known temperatures. This is done using a microwave absorber as a black body once at room temperature and again floating on liquid nitrogen (LN2). The temperature of LN2 is known since it boils at approximately 77 K under atmospheric conditions. Since according to the Rayleigh-Jeans law the power emitted by a black body at a given frequency is proportional to its temperature T_{BB} the power measured by a receiver P_{meas} is given by [33]

$$P_{meas} = g \cdot (T_{BB} + T_{rec}) \,, \tag{4.40}$$

where g is the gain of the receiving system and T_{rec} is its noise temperature. When the emission is measured at two calibration points (LN2 and room temperature), the noise temperature and the gain factor of the receiver can be determined for the measured frequency. Afterwards, the same equation can be used to calculate radiation temperatures for signals of arbitrary origin. For calibration, the complete setup with the phase shifter, the coupler, the amplifiers, the cables and the analyzer is installed on a table. Instead of the ECE mirror, a plane mirror at 45° is used to get a view of the antenna into a canister with the microwave absorber. This canister is used in ambient air and afterwards filled with liquid nitrogen. As an example, the measured power in the range from 14.5 to 15.5 GHz for LN2 and room temperature is shown in figure 4.32. The coupler position $d = 0.299"$ that is used for the temperature measurements at TJ-K was used in this measurement leading to a low coupling factor for 15 GHz from the waveguide to the cable. The result can be seen in the graph as the difference of room temperature and liquid nitrogen power at precisely 15.0 GHz is only 0.26 dB (0.06 nW after amplification).

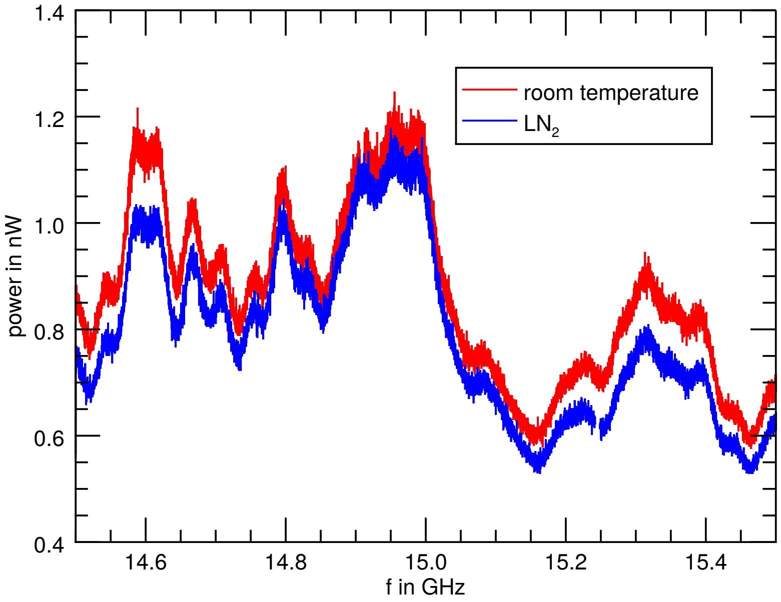

Figure 4.32.: Received power spectrum at the HP70001A analyzer after amplification from a liquid nitrogen cooled microwave absorber at 77 K (blue) and at room temperature at about 295 K (red) with coupler position $d_c = 0.299"$.

Uncertainties in the liquid nitrogen calibration due to reflections at the surface of the liquid forming standing waves [33] were not observed. This was tested by phase shifting as well as in long-time measurements at a fixed frequency. The results show no visible ($< 0.08\,$dB) influence of the effective resonator length in both cases.

In order to use this calibration, it has to be checked that the measurement system is linear in the entire range of operation [3], i.e. the output voltage U is proportional to the signal power P_{meas}. This was done using the Wiltron 68337B signal generator once for the spectrum analyzer and separately for the amplifiers. The linearity of the cascaded low noise amplifiers is validated from -100 dBm to -50 dBm input power showing 53 dB gain for 15 GHz. For levels below, the amplifiers are still linear but the noise contributes significantly to the measured powers. When the output voltage is converted to signal power and the hot-cold calibration is used to obtain the gain and system noise temperature, the radiation temperature can be calculated from the measured powers using equation (4.40). For an optically thick plasma, the radiation temperature equals the electron temperature of the plasma. In the case of optically thin plasmas, the electron temperature can be obtained from equation (4.15) when the optical depth is known. Both, for the linear evaluation using the optical depth and for the optically extremely thin cases with $P_{meas} \sim n_e T_e^2$, more information is needed which can be obtained from a reference plasma. A Langmuir probe that is positioned on the flux surface where the main contribution for the envisaged ECE frequency is emitted can deliver the electron temperature on this surface. Then the effective optical depth for the entire setup including the diagnostic resonator can be calculated as well as the prefactor for the evaluation with squared electron temperatures is available. With this last step, the calibration is complete for all plasma states that do not severely differ in the effective optical depth or resonator properties. To what extent this condition is fulfilled can be judged from the quality of the temperature results in section 4.6.4.

4.6.3 Procedure of the measurements

As a first step, a plasma with average parameters is generated. As a check, the coupler is set to the position $d_c = 0.280"$ where no coupling to the coaxial cable is expected as the coupling pin is then in the node of the standing wave pattern. This is checked by tuning the phase shifter without a change in the received signal power. Then the coupler is slightly moved to $d_c = 0.299"$ in order to produce measurable signals while the main amount of the radiation is reflected into the resonator. Afterwards, the phase shifter is adjusted to optimize the effective length of the resonator for 15 GHz measurements where the transfer function of the system has its maximum. That point is reached as soon as the signal with constant coupling reaches its maximum. A Langmuir probe in the 2D unit at port O6 is used simultaneously in order to measure reference electron temperatures that are compared to the temperatures from the ECE diagnostic. The probe is positioned at the intersection of the centerline of the port with the resonant surface for 15 GHz second harmonic ECE, at the point $(R = 60.7\,\mathrm{cm}, z = 0\,\mathrm{cm}, \phi = 30°)$. Therefore, at this location the same temperature as at the main spot of the ECE diagnostic's contribution volume should be measured. To probe for the operating regime of the ECE diagnostic, $u_{\mathrm{He}} = 27$ helium and $u_{\mathrm{Ar}} = 16$ argon plasma discharges with neutral gas pressures[3] between $p_0 = 7\,\mathrm{mPa}$ and $p_0 = 97\,\mathrm{mPa}$ for helium and between $p_0 = 1.3\,\mathrm{mPa}$ and $p_0 = 9\,\mathrm{mPa}$ for argon were examined. Heating powers from 1000 W to 2450 W were used.

The evaluation of electron temperatures from the electron cyclotron emission diagnostic requires the calibration parameters that were obtained from the hot-cold method in section 4.6.2. Furthermore, in optically thin plasmas a reference is needed that provides for the effective optical depth τ_{eff} in the linear temperature dependence case, or in the extremely thin case the prefactor of the T_e^2 dependence. Although the numerical integration of the radiation transport equation in section 4.1.2 already shows that TJ-K has extremely optically thin plasmas, the classical evaluation for optically thin plasmas using equation (4.15) is also executed for comparison. Furthermore, the quadratic evaluation is done once with a common prefactor for the measurements which means that an average value for the plasma density is used. With a separate prefactor for each shot using the corresponding value of the electron density as equation 4.6 suggest, the evaluation is repeated. From the comparison of the results, the necessity of density measurements for the ECE diagnostic can be concluded.

4.6.4 Resulting electron temperatures

As common reference plasma shot #12526 was chosen for all types of evaluation of argon plasmas and #12580 in the helium cases. The common choice improves the comparability of the results and is close to the procedure of measurements in routine operation of a diagnostic where only a single calibration should be required. By trying different reference plasmas care was taken that the different types of evaluation that are compared do not suffer significantly from this choice, i.e. an optimal choice for each evaluation would produce very similar results.

All temperatures obtained from the ECE diagnostic $T_{e,ECE}$ are compared to the temperatures $T_{e,Langm.}$ that current-voltage characteristics of the Langmuir probe deliver. As an indicator of the electron temperature deviation of the ECE measurements from the Langmuir probe results, the root mean squared error (RMSE) $\Delta(k_B T_e)$ is calculated as follows:

---

[3] Note that these are the values after the gas type correction and not the values displayed by the Pfeiffer Vacuum PKR 251 pressure gauge.

$$\Delta\left(k_B T_e\right) = k_B \sqrt{\frac{1}{u}\sum_{i=1}^{u}\left(T_{e,ECE,i} - T_{e,Langm.,i}\right)^2}, \tag{4.41}$$

where u is the number of evaluated discharges for the used gas type. The evaluations are done for helium and argon separately and the resulting temperatures are shown in figures 4.33. In all cases, the quadratic dependence on the temperature provides temperature results that agree better with the Langmuir probe results than the linear dependence using the optical depth. The linear evaluation has a RMSE of about $\Delta(k_B T_e)_{\mathrm{Ar}} \approx 1.7\,\mathrm{eV}$ for the argon series and $\Delta(k_B T_e)_{\mathrm{He}} \approx 24\,\mathrm{eV}$ for the helium series. The square evaluations for argon have an error compared to the Langmuir data of $\Delta(k_B T_e)_{\mathrm{Ar,n}} \approx 0.90\,\mathrm{eV}$ evaluating the density for every shot separately and $\Delta(k_B T_e)_{\mathrm{Ar}} \approx 0.76\,\mathrm{eV}$ disregarding the density influence, respectively. In the helium case the values are $\Delta(k_B T_e)_{\mathrm{He,n}} \approx 4.7\,\mathrm{eV}$ with density influence and $\Delta(k_B T_e)_{\mathrm{He}} \approx 4.3\,\mathrm{eV}$ without. The electron density varied by a factor of 5 in the measurements with helium and a factor of 4.3 for argon. However, taking the measured electron density for each plasma into account does not improve the results although the square evaluation shows much better results than the linear dependence for plasmas close to optical thickness. Consequently, the case in TJ-K with resonator seems to lie between the pure emissivity case with density influence and T_e^2 dependence and the optically thick case without density influence but T_e dependence.

Especially in the helium series most of the deviations are seen for high temperatures. Temperatures from the linear evaluation are even far above the expected thermal energy range for TJ-K at values up to 70 eV. The neutral gas pressures of the plasmas that produced these results were below the typical operating range at TJ-K and very close to regions where ionizing radiation appears.

4.7 Summary and discussion of the ECE measurements at optically thin plasmas

A diagnostic system for the temperature measurement from electron cyclotron emission for TJ-K was successfully designed, built and applied to TJ-K plasmas. The calibration of the system was done using the hot-cold method with liquid nitrogen and a Langmuir probe was used as a reference. With the tunable resonator setup, an agreement between Langmuir probe temperature measurements and the new ECE diagnostic was seen. Argon and helium plasmas with different heating powers and neutral gas pressures prove the ECE diagnostic suitable for temperature measurements in typical TJ-K parameter ranges despite the fact that the plasma is extremely optically thin. With the resonator setup, the agreement between ECE and Langmuir probe measurements was improved as the comparison of figures 4.25 and 4.33 shows. Simulations of the radiation transport equation have shown that for extremely low optical depths like in TJ-K, the temperature dependence of the emissivity is also present for the measured power. This knowledge was used in the evaluation and confirmed the simulation results as the evaluated temperatures using a $P_{meas} \sim T_e^2$ dependence agree well with the Langmuir reference temperatures.

Also, very low neutral gas pressures below the standard operating range show a strong increase in the measured temperatures when TJ-K is operated close to the x-ray emitting scenarios. Because electron

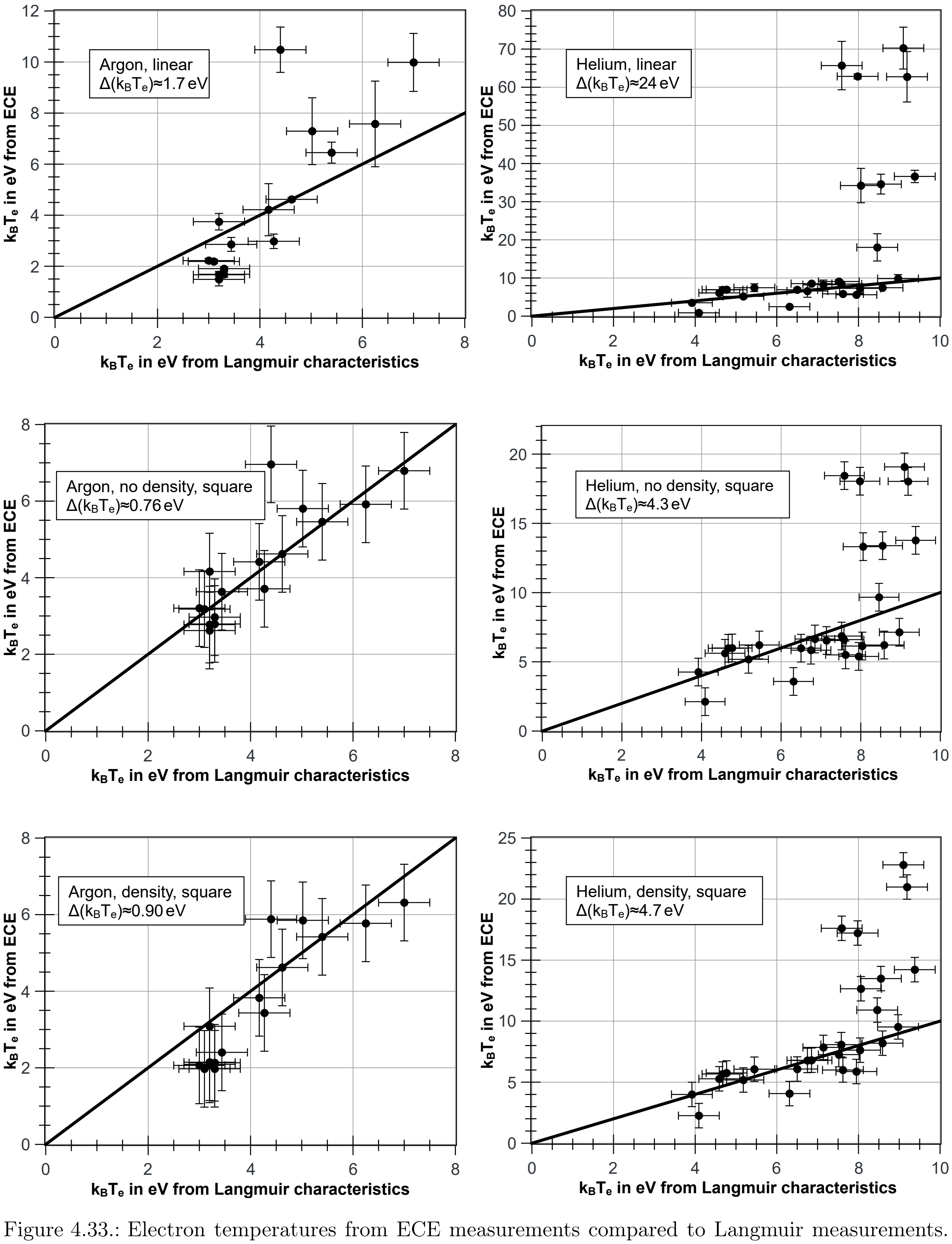

Figure 4.33.: Electron temperatures from ECE measurements compared to Langmuir measurements. Evaluation with T_e, with T_e^2 and $n_e T_e^2$ dependence for low optical depths are shown.

cyclotron emission diagnostics are known to show high intensities over a broad frequency range when superthermal electrons are present and especially in optically thin plasmas like in TJ-K superthermal electrons are known to have a strong impact on the emitted power [7,35], the ECE diagnostic indicates the existence of superthermal electrons and the operating parameters of TJ-K can be scanned to identify the ranges with and without superthermal electrons for future experiments. This supports the proposition that superthermal electrons are generated in low-pressure plasma discharges and produce the x-rays.

Even if the resonator and mirror cannot be ideally matched to all possible plasma conditions, the temperatures compare well to the Langmuir measurements. The agreement might be supported by temperature profiles that only shift between different discharges but have the same shape. Then the measurements do not need to be closely localized but also a spatially averaged measurement can provide useful temperature results. Furthermore, the measurement at 15 GHz corresponds to the plasma core where the temperature profile is flat as can be seen in figure 4.8. Therefore, the measurement over several flux surfaces does not compromise the results.

Altogether, it was shown that ECE diagnostics can operate successfully at extraordinarily low optical depths when the temperature dependence of the emissivity for the used harmonic is considered. The first curvature optimizing mirror and resonator setup to enhance the localization of the measurement were successfully employed and have been shown to improve the localization of the measurements by a factor of approximately 9. Additionally, the ECE diagnostic indicates the presence of superthermal electrons in TJ-K plasmas.

5 Simulation of electron drift orbits and toroidal net currents

Temperature evaluations using the ECE diagnostic show indications of the existence of superthermal electrons (see section 4.7). In this chapter, the generation of toroidal net currents by such superthermal electrons is examined.

Experiments with modulated microwave heating power were used in the past to investigate the presence of toroidal net currents in the plasmas of TJ-K. A toroidal current can be measured through the magnetic field that it generates. When the plasma is turned off, the current decays and a change in the magnetic field is generated that can be used to measure the current strength and direction with a diagnostic coil that surrounds the plasma, a Rogowski coil [37, 38]. As can be seen in figure 5.1, this kind of experiments has shown toroidal net currents with strengths from only a few Ampères up to almost 30 A in scenarios with two microwave heating frequencies [12].

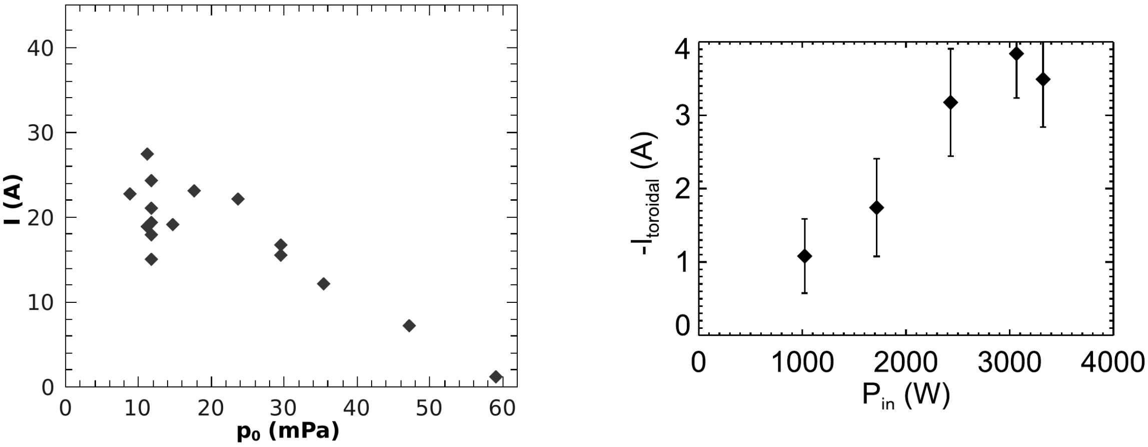

Figure 5.1.: Experimentally obtained absolute toroidal net currents in TJ-K for different neutral gas pressures with two microwave heating frequencies used simultaneously (left, [12]) and signed toroidal net current for different powers of the 8 GHz heating (right, [13]).

In these experiments, the toroidal net currents have been found to depend inversely on the neutral gas pressure and the currents have dropped when a Langmuir probe was introduced. In further experiments with a single and resonant microwave heating frequency [13] an increase of the currents with the microwave heating power was seen and the current found to be directed opposite to the magnetic field. With resonant heating, currents below 4 A were seen. Not a drift of the bulk electrons but superthermal electrons were proposed to be responsible for the observed currents [12, 39]. Larger neutral gas pressures are expected to reduce the number of superthermal electrons by impeding the acceleration of thermal electrons to higher speeds by shorter mean free paths. Also the observed disappearance of toroidal currents when a Langmuir probe was introduced is in accordance with the idea of fast electrons forming the current since the probe can act as an obstacle that helps in the thermalization process of the plasma. In the stellarator TJ-II, for example, a movable paddle is used to eliminate superthermal electrons [101].

Toroidal net currents were accompanied by the presence of ionizing radiation at WEGA [39] and TJ-K [12]. Such radiation can be generated when superthermal electrons collide with vessel components. At WEGA even a connection between the toroidal distribution of the radiation and the position of in-vessel components was found [39]. Measurement scenarios with the emission of x-rays were discontinued at TJ-K owing to the lack of remote operation and therefore missing protection from radiation. As mechanism behind the generation of toroidal net currents, a direction dependent loss mechanism of charges was put forward [39] that is based on the different trajectories of thermal and superthermal electrons in the magnetic cage depending on their propagation direction. The electrons move on drift orbits that are either larger or smaller than the flux surface, depending on the direction of motion and the magnetic field geometry. The direction dependence of the orbit may lead to a directivity of electron losses at the vessel wall due to large drift orbits. Simulations of the electron trajectories for different velocity distributions are therefore used to examine the drift orbits as possible sources of toroidal net currents in TJ-K as discussed in this chapter after the theoretical background is provided in the following subsections. As Langmuir probe characteristics have shown populations of electrons at energies of 30 eV, 500 eV and even 1.3 keV in 2.45 GHz heated plasmas [102], a wide range of energies of 10 eV, 100 eV and 1000 eV is covered in the simulations.

5.1 Theory of electron trajectory simulations

Trajectories of charged particles in background magnetic fields can be very complicated unless a strict and simple symmetry is present. The Lorentz force $\vec{F}_L = -e\vec{v} \times \vec{B}$ acts on motion perpendicular to the magnetic field $\vec{B}$ and diverts an electron with charge $-e$ perpendicular to its initial velocity $\vec{v}$ and to the magnetic field. For a homogeneous field strength, a circular motion around the field line, the gyration, results while the velocity component parallel to $\vec{B}$ is not affected. On the one hand, the radius of the circular motion, the Larmor radius ρ_L, is often very small (tens of micrometers for TJ-K) while on the other hand, the parallel motion can be of the order of the vessel circumference which covers several meters. For simulations, this means that toroidal turns need tens of millions of simulation steps when simultaneously the gyration has to be resolved. As a consequence, the simulation times are long and numerical errors can accumulate. Because of the need for large numbers of trajectories for the statistical simulation of velocity distributions the full trajectories cannot be considered for toroidal net current investigations. Fortunately, the full simulation of the gyration can be replaced in the simulations by the guiding center approximation that is explained in the following and leads to a considerable saving in computational effort.

5.1.1 The guiding center approximation

Particle trajectories are in general very complex such that analytical solutions of the equation of motion are usually only possible in highly symmetric cases. A simplification of the problem has to consider the envisaged scale of the simulation: a local (Taylor) expansion can be useful for short-time simulations of the gyration but when many gyration periods should be covered, another model is promising: the guiding center approximation splits the problem into the gyration with the Larmor radius ρ_L and the motion of the gyration center parallel to the magnetic field [103]. As long as the gyration of an electron in a magnetic field takes place on an orbit around the field line that is small enough to cover no significant change in the magnetic field strength, the gyration is circular and can be represented by the motion of its center with a set of drift equations. This condition can be written as

$$\rho_L = \frac{m_e v_\perp}{e|\vec{B}|} \ll \frac{|\vec{B}|}{\left|\nabla|\vec{B}|\right|} =: L_B, \tag{5.1}$$

where $v_\perp$ is the speed perpendicular to the background magnetic field. In TJ-K simulations using the guiding center approximation, the validity was checked with 1 % as the limit for the gyroradius compared to the gradient length L_B. For the center line of port O5, this is easily fulfilled as the gradient length is about $L_B = 0.27\,\mathrm{m}$ (see also section 3.3) and thermal plasmas have gyration radii of some tens of microns. Similar values can be expected in most of TJ-K's volume and plasmas. However, close to the magnetic field coils and in the case of fast electrons a recurrent check of this condition in simulations is reasonable because strong field gradients or large Larmor radii are possible in these cases.

The guiding center has a parallel motion along the field line and a perpendicular motion that is described by drift velocities. These drifts can arise from the magnetic field geometry or external forces. In a magnetic field $\vec{B}$ with an additional force $\vec{F}$ the equation of motion is:

$$m_e \dot{\vec{v}} = -e\vec{v} \times \vec{B} + \vec{F}. \tag{5.2}$$

Because of the vector product in the Lorentz force only the force $\vec{F}$ can act parallel to B. The perpendicular components are coupled differential equations which in a Cartesian system with B along the z-axis the differential equations are:

$$\begin{aligned} m_e \dot{v}_x &= e v_y B + F_x, \\ m_e \dot{v}_y &= e v_x B + F_y. \end{aligned} \tag{5.3}$$

Differentiation and combination of the equations yields the circular gyration around the magnetic field modified by a motion perpendicular to the external force $\vec{F}$:

$$\begin{aligned} v_x &= v_\perp \cos\left(\omega_{ce} t\right) - \frac{F_y}{eB}, \\ v_y &= - v_\perp \sin\left(\omega_{ce} t\right) + \frac{F_x}{eB}, \end{aligned} \tag{5.4}$$

where $v_\perp := \sqrt{v_x^2 + v_y^2}$ and $\omega_{ce} := eB/m_e$ is the electron cyclotron frequency. When the motion is integrated over a gyration period the gyration is averaged out due to the symmetry of sine and cosine and the drift velocity of the guiding center is obtained. In a general coordinate system, the drift velocity resulting from a force $\vec{F}$ is

$$\vec{v}_D = -\frac{\vec{F} \times \vec{B}}{e|\vec{B}|^2}. \tag{5.5}$$

Two drifts are relevant for the formation of electron drift orbits: the curvature drift and the gradient drift. The curvature drift occurs when the guiding center follows a locally curved magnetic field line. A centrifugal force $\vec{F}_{cf}$ in the electron's frame of reference occurs:

$$\vec{F}_{cf} = \frac{m_e v_\parallel^2}{R_c^2} \vec{R}_c, \tag{5.6}$$

where $\vec{R}_c$ is the curvature vector of the magnetic field line pointing from the curvature center to the electron. According to equation (5.5), the guiding center experiences the curvature drift $\vec{v}_D^c$ proportional to the kinetic energy of the electron parallel to the magnetic field $W_\parallel = 1/2 \cdot m_e v_\parallel^2$ [4]:

$$\vec{v}_D^c = -\frac{2W_\parallel}{e} \frac{\vec{R}_c \times \vec{B}}{R_c^2 |\vec{B}|^2}, \tag{5.7}$$

which can be reformed using the identity [54] $-\vec{R}_c/R_c^2 = \nabla_\perp |\vec{B}|/|B|$:

$$\vec{v}_D^c = \frac{2W_\parallel}{e} \frac{\nabla_\perp |\vec{B}| \times \vec{B}}{|\vec{B}|^3}, \tag{5.8}$$

where $\nabla_\perp |\vec{B}|$ is the change of the magnetic field strength perpendicular to the field vector.
Also the gradient in the field strength perpendicular to the magnetic field leads to a drift. Small gradients that allow for the use of the guiding center approximation according to condition (5.1) still result in small differences of the absolute magnetic field strength along the gyration of the electron. In regions with larger magnetic fields, the Larmor radius is slightly smaller than in the region with a smaller background field. Therefore, a drift of the guiding center perpendicular to the magnetic field results as it is illustrated in figure 5.2.

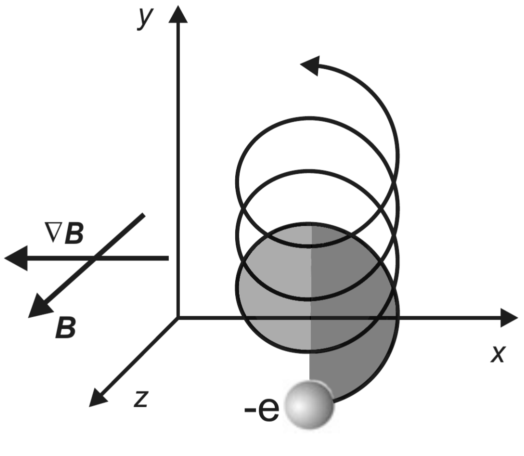

Figure 5.2.: Vertical drift of an electron in a magnetic field gradient directed to the left. The Larmor radius on the high-field side (light gray) is smaller than on the low-field side (dark gray) leading to a drift upwards in this geometry. Adapted from [54].

When a magnetic field gradient in negative x-direction is considered and the gradient is weak on the scale of a Larmor radius around the guiding center at the origin, the guiding center drift can be calculated from a first-order expansion of the field:

$$\begin{aligned} F_{L,x} &\approx -ev_y\left(B + \frac{\partial B}{\partial x}x\right), \\ F_{L,y} &\approx ev_x\left(B + \frac{\partial B}{\partial x}x\right). \end{aligned} \tag{5.9}$$

Since the gyration is to the first order circular, this results in:

$$\begin{aligned} F_{L,x} &\approx ev_\perp \sin(\omega_{ce}t)\left(B + \frac{\partial B}{\partial x}v_\perp/\omega_{ce}\sin(\omega_{ce}t)\right), \\ F_{L,y} &\approx ev_\perp \cos(\omega_{ce}t)\left(B + \frac{\partial B}{\partial x}v_\perp/\omega_{ce}\sin(\omega_{ce}t)\right). \end{aligned} \tag{5.10}$$

When the force is time-averaged over a gyration period the sin, cos and sin · cos terms vanish but the $\sin^2$ term yields:

$$\overline{F}_{L,x} \approx -\frac{1}{2}m_e v_\perp^2 \frac{1}{B}\frac{\partial B}{\partial x}. \tag{5.11}$$

For an arbitrary field gradient, the resulting drift velocity is obtained when the time-integrated force is inserted into equation (5.5) yielding [54]:

$$\vec{v}_D^\nabla = \frac{W_\perp}{e}\frac{\vec{\nabla}_\perp|\vec{B}| \times \vec{B}}{|\vec{B}|^3}. \tag{5.12}$$

Further drift velocities appear whenever additional forces act on the electron, for example in the presence of an electric field. Those effects are not considered here. The total drift velocity from the magnetic field curvature (equation (5.8)) and gradient (equation (5.12)) can be written as

$$\vec{v}_D = \left(W_\perp + 2W_\parallel\right)\frac{\vec{\nabla}_\perp|\vec{B}| \times \vec{B}}{e|\vec{B}|^3}. \tag{5.13}$$

In a simple case with a toroidal magnetic field and a magnetic field gradient that points along the major radius, the drift is purely vertical. In the more complex geometry of fusion experiments with twisted field lines, also a vertical component of the magnetic field is present which leads to a horizontal component in the drift velocity. The trajectories resulting from the drifts in a magnetic field are discussed in the next section.

Additional to the drift velocities that displace the guiding center, the kinetic energy is shifted between perpendicular and parallel motion when the charge moves to a region with a different magnetic field strength because the Larmor radius changes. The conservation of angular momentum implies that the perpendicular velocity has to compensate for the changed radius. As the conservation of energy demands, the energy of the perpendicular velocity is exchanged with the parallel kinetic energy.

The shift between perpendicular and parallel energy can even result in the reflection of an electron when the entire parallel energy is transferred to the perpendicular motion. Therefore, a geometry with a magnetic well can be used as a magnetic mirror. Reflections of this type depend on the magnetic field strength and the ratio of perpendicular and parallel velocity of the charge.

5.1.2 Electron drift orbits in TJ-K

The local drift velocities can change the entire trajectory of a charge because of the local changes in the magnetic field: due to the drift, a completely different geometry can be entered that changes the trajectory fundamentally. Figure 5.3 shows the evolution of the radial position R and the vertical position z of guiding center simulations performed with MCC in the 3D magnetic field geometry of TJ-K. The plot can be understood as a projection of the trajectories to a poloidal plane.

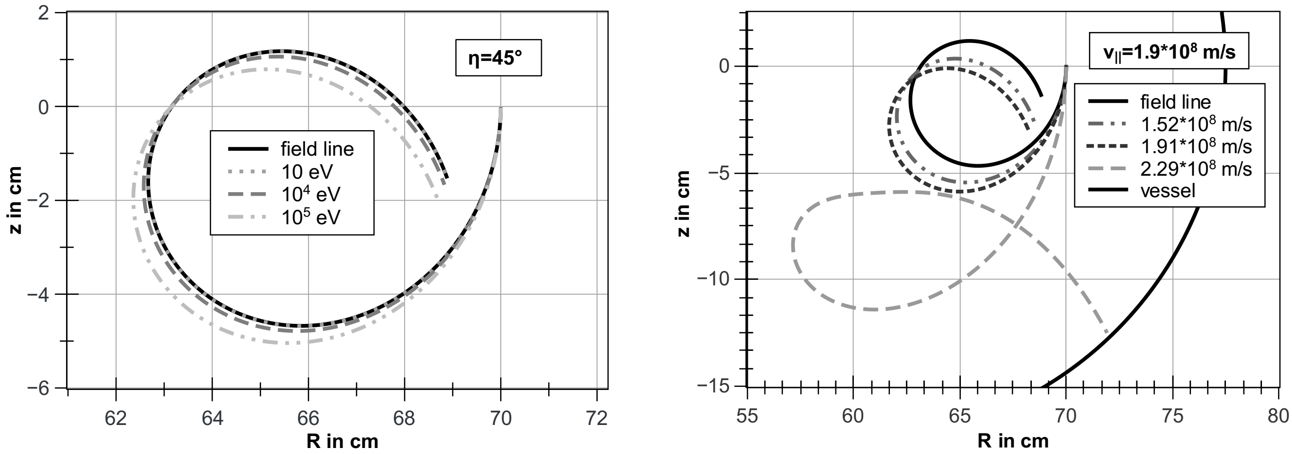

Figure 5.3.: Electron guiding center trajectories compared to the magnetic field line for various electron energies with constant pitch angle (left) and different perpendicular speeds (right).

On the left, the results from simulations for different electron energies with the initial pitch angle $\eta = \arctan\left(v_\perp/v_\|\right) = 45°$ are shown compared to the field line for 57° of toroidal movement. A drift away from the field line can be seen for high kinetic electron energies while for 10 eV ($1.9 \cdot 10^6\, \frac{\mathrm{m}}{\mathrm{s}}$) the field line and trajectory are congruent. On the right, simulations for different pitch angles with a constant $v_\| = 1.9 \cdot 10^8$ m/s are shown. A clear deviation from the field line can be seen (note the different scales of the left and right figure). For the highest speed, the trajectory is very different from the field line and leads to the loss of the electron at the vessel wall.

To illustrate the principles of the formation of drift orbits, a simplified geometry is considered: figure 5.4 shows a poloidal cross-section of a toroidal plasma with circular flux surfaces.

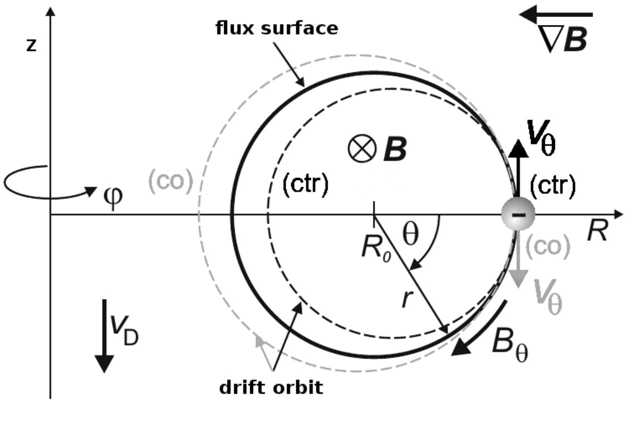

Figure 5.4.: Schematic illustration of the drift velocities that lead to drift orbits of an electron in a toroidal plasma, modified from [4].

An electron at the outermost point of a flux surface is considered in this geometry with a magnetic field mainly pointing into the plane and an absolute field gradient towards lower R. The winding of the magnetic field as it is required for toroidal plasma experiments is indicated by the poloidal field component B_θ, turning clockwise. The total drift velocity at the starting position according to equation (5.13) is directed downwards. At the electron position, the magnetic field line along positive $d\phi$ has a negative vertical component as the poloidal component indicates. When the electron moves into the plane, co-moving compared to the magnetic field, it follows this field line downwards and simultaneously experiences a drift velocity downwards. Therefore, the guiding center moves further down than the flux surface. Along its way around the torus, the electron trajectory departs from the flux surface as long as the drift velocity points away from the flux surface. When the electron reaches the upper half of this plot, the electron approaches the flux surface again because there the drift downwards is directed towards the initial flux surface again. Therefore, the electron trajectory finally meets the original surface again in this symmetric setup. The surface on which the electron moves with non-negligible drift velocity is called electron drift orbit.

In the case of a counter-moving electron, the drift direction is still directed downwards but the field line is directed upwards. Hence, a drift orbit is formed that is smaller than the flux surface. When the drift orbit is larger than the flux surface the electron possibly reaches regions outside the last closed flux surface or even hits the wall of the vessel. Due to the velocity dependence of the drifts the deviation from the flux surface increases with higher electron energies.

Simulations of the particle trajectories in the geometry of TJ-K have been performed using MCC. Figure 5.5 shows in the poloidal cross-section at inner port I1 the results of four simulations:

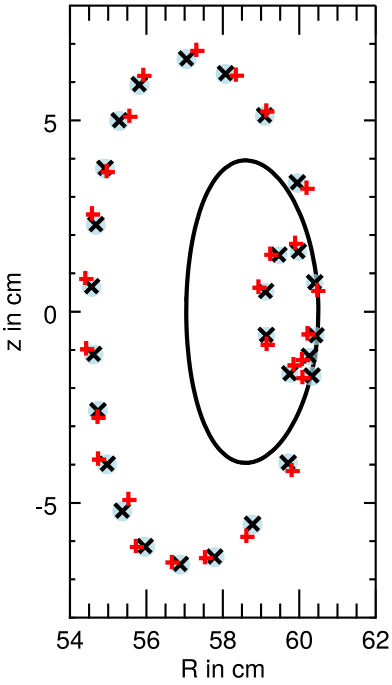

Figure 5.5.: Poincaré plot of a co-moving electron (larger orbit) and counter-moving electron (smaller orbit). Guiding center approximation (**x**) and the full trajectory (+) are shown. The solid line represents the flux surface that the electrons started on with $|\vec{v}| = 2.5 \cdot 10^8$ m/s $\approx 0.83 \cdot c$ and $v_\perp = 0.7 \cdot |\vec{v}|$. The shaded circles show the relativistic Larmor radius.

The trajectory of a very fast electron with $|\vec{v}| = 2.5 \cdot 10^8\,\mathrm{m/s} \approx 0.83 \cdot c$ is simulated from the same starting point first using the guiding center approximation and again with the full trajectory and both types of simulation are performed for a co-moving and a counter-moving electron. For the large perpendicular velocity of $0.7 \cdot |\vec{v}|$, the Larmor radius is, in this case, almost 7 mm large and shown in the graph as circles around the guiding center positions. Not only a large difference between the drift orbit and the flux surface on which the electron starts is visible but it can also be seen that the simulations of the full trajectory show electron positions that are within the Larmor radius around the guiding center results. This agreement shows that even for this very high velocity and relativistic case the simulation of the full trajectory can still be modeled using the guiding center approach. As a measure for the difference between the drift orbit and the flux surface, the horizontal distance of the points with minimal R in a poloidal cross-section like in figure 5.5 can be used. In the case shown this distance is about 2.6 cm for the co-moving electron and 2 cm when the electron moves in the opposite direction. This high velocity was chosen to demonstrate the effect with easily visible Larmor radii and drift orbit sizes. The typical thermal velocity in TJ-K is only about $1.9 \cdot 10^6\,\mathrm{m/s} \approx 0.006 \cdot c$ (at $k_B T_e = 10\,\mathrm{eV}$). Figure 5.6 shows for simulations from another starting point that the difference between the flux surface and drift orbit is much smaller for thermal electrons in TJ-K.

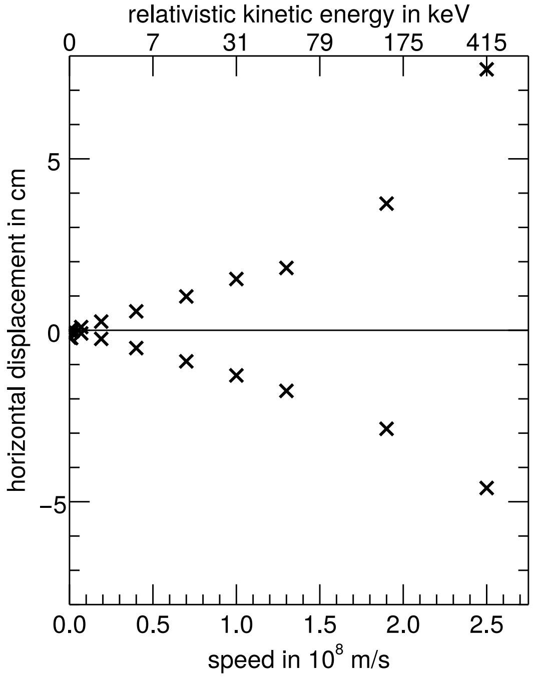

Figure 5.6.: Maximum horizontal distance between the flux surface and the drift orbit evaluated in a poloidal plane for electron motion in TJ-K parallel and antiparallel to the magnetic field with constant $v_\perp/|\vec{v}|$.

For $1.9 \cdot 10^6\,\mathrm{m/s}$, the distances are below 300 microns. Therefore, either fast electrons with larger distances from the flux surface or electrons at the edge of the confinement region are likely to collide with the walls due to the drift orbit size. As already indicated in figure 5.4, electrons that start in the opposite direction form a drift orbit that is not larger than the flux surface but smaller. Also for this case, the horizontal distance was evaluated for different speeds. The corresponding distances are shown as negative horizontal displacements in figure 5.6. In contrast to the case with larger drift orbits, orbits smaller than the flux surface have a natural limit for the difference as the orbit shrinks to a single point in the Poincaré plot. For this type of drift orbits, the electron trajectories cannot cross the plasma border and therefore the drift orbits do not lead to losses due to collisions with the vessel wall. The influence of the velocity components parallel and perpendicular to the magnetic field is visible when one of the two is varied but the other fixed. Both of these variants were simulated for motion parallel to the magnetic field ($\sphericalangle(\vec{B}, \vec{v}) < 90°$) with $1 \cdot 10^6\,\mathrm{m/s}$ for the fixed component. The resulting deviations of the drift planes compared to the flux surfaces, shown in figure 5.7, confirm that both components play a role in the formation of drift orbits.

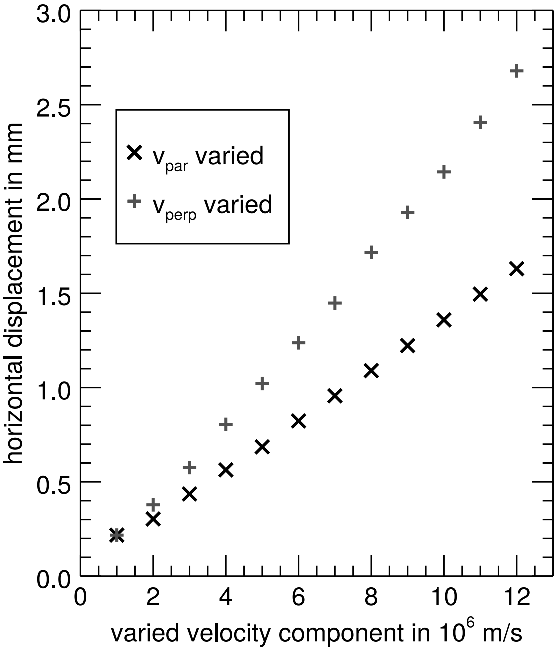

Figure 5.7.: Maximum horizontal distance between the drift surface and the flux surface in the $\phi = 0$ plane for variation of only one velocity component for each curve. The other component is fixed at $1 \cdot 10^6\,\mathrm{m/s}$.

According to equation (5.13), one would expect the parallel velocity component to contribute twice as much to the displacement compared to the perpendicular component. Nevertheless, a stronger influence of the increase of the perpendicular component is seen. This effect is attributed to the complexity of the 3D geometry of the confining magnetic field. The difference of drift orbits in the parallel and antiparallel case is notably increased by the fact that the rotational transform varies significantly in the stellarator geometry [104]. Furthermore, very different magnetic field strengths can be experienced and also the field line curvature due to the magnetic ripple can even exceed the contribution of the curvature from the toroidal shape [104]. Considerations deduced from the drift velocity equation (5.13) can therefore only be the basis for explaining potential deviations of the movement from the flux surfaces. Moreover, simulations of entire velocity distributions in the whole magnetic geometry are required to evaluate the influence of the complex stellarator geometry on the trajectories.

When the charge does not start on the right side in figure 5.4, the low-field side, but on the high-field side on the left, the relation between drift orbit size compared to the flux surface and the propagation direction is inverted. This becomes obvious when the already discussed trajectory (co-moving in figure 5.4) with a drift orbit larger than the flux surface is compared to an electron that starts at the opposite side of the plasma in the same picture. If the electron has the velocity that the first electron has at the same spot, it has to move on the same orbit as it is identical with the one considered first. However, the flux surface that intersects with this new starting point is now considered as reference. This surface is larger than the original reference and therefore the orbit is smaller than the flux surface. Because the electron is still co-moving it cannot be concluded that either parallel or antiparallel movement leads to orbits larger than the flux surface and causes particle losses due to collisions with the wall. Instead, the complexity of the process in the detailed geometry of the magnetic field and the particle density are addressed in numerical simulations.

5.1.3 Electron velocity distributions

Neither the investigation of single electrons is sufficient to understand the possible strength of toroidal net currents nor is it possible to simulate all the electrons within the plasma volume of TJ-K. Therefore, a statistical description of the electron velocity distribution and the density distribution are used for net current investigations. Electron velocity distributions cannot be measured from electron cyclotron emission measurements [6] which makes it necessary to assume a velocity distribution. The probability to find a particle of a non-relativistic ideal gas that is in thermodynamic equilibrium and has negligible quantum effects in an interval d^3v around the velocity $\vec{v}$ is given by the Maxwell-Boltzmann probability density function [105]

$$f_M(\vec{v}) = \left(\frac{m_e}{2\pi k_B T_e}\right)^{3/2} \exp\left(-\frac{m_e|\vec{v}|^2}{2k_B T_e}\right), \tag{5.14}$$

which is the product of three independent centered Gaussians with variance $k_B T_e/m_e$ and expectation value 0, each for a Cartesian velocity component [105]. A more intuitive form is reached when the direction of the velocity is ignored and only the speed is plotted. The probability $p(v)$ for an electron in a plasma with thermal energy $k_B T_e$ to have the speed v is obtained by transformation into spherical coordinates and integration over the angular components of the velocity. This results in

$$p(v) = 4\pi \left(\frac{m_e}{2\pi k_B T_e}\right)^{3/2} v^2 \exp\left(-\frac{m_e v^2}{2k_B T_e}\right), \tag{5.15}$$

and is illustrated for different thermal energies in figure 5.8.

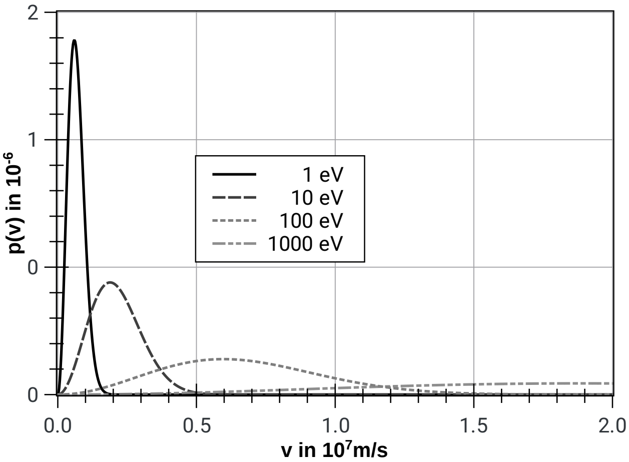

Figure 5.8.: Probability of different speeds in 3D Maxwell-Boltzmann distributed gases with different thermal energies.

The most probable speed of this distribution is given by the thermal velocity

$$v_{th} = \sqrt{\frac{2k_BT_e}{m_e}}. \tag{5.16}$$

For a typical thermal energy in TJ-K of $k_BT_e = 10\,\mathrm{eV}$ the most probable velocity is $v_{th} \approx 1.9 \cdot 10^6\,\mathrm{m/s}$. Numerically, a Maxwell-Boltzmann velocity distribution is generated by a Gaussian random number generator for all three components. The temperature is included in the variance of the Gaussian. The standard Gaussian density function $f_s(G)$ with expectation value 0 and variance 1 is generated using the Box-Muller method [106] from uniformly distributed random numbers u_1 and u_2 that are provided by the operating system via the C++ programming language. With this method a standard Gaussian random number G is obtained by calculating

$$G = \sqrt{-2\ln(u_1)}\sin(2 \cdot \pi \cdot u_2). \tag{5.17}$$

This number is transformed to a velocity component v_i of a Maxwell-Boltzmann distribution with temperature T_e:

$$v_i = T(G) = \sqrt{\frac{k_BT_e}{m_e}} \cdot G. \tag{5.18}$$

This linear transform $T(G)$ scales the abscissa and therefore modifies the width of the distribution. An arbitrary linear transform modifies the density function as follows [107]:

$$f(v_i) = f(T^{-1}(v_i)) \cdot \left|\frac{\mathrm{d}T^{-1}(v_i)}{\mathrm{d}v_i}\right|. \tag{5.19}$$

Therefore, the resulting density function is in the concrete case:

$$\begin{aligned} f(v_i) &= \frac{1}{\sqrt{2\pi}} \exp\left(-\frac{1}{2}\left(\sqrt{\frac{m_e}{k_BT_e}}v_i\right)^2\right) \cdot \sqrt{\frac{m_e}{k_BT_e}} \\ &= \sqrt{\frac{m_e}{2\pi k_BT_e}} \exp\left(-\frac{m_ev^2}{2k_BT_e}\right), \end{aligned} \tag{5.20}$$

which is a Gaussian with mean 0 and variance k_BT_e/m_e as desired for each velocity component.

As another type of velocity distribution monoenergetic populations are used. In this case, all electrons start with the same speed v_{mono} but random direction which is reached by normalization of all velocity components v_i by multiplication with $v_{mono}/|\vec{v}|$. Monoenergetic populations have the advantage that there is no probability of other velocities. Maxwell-Boltzmann distributions on the contrary only have a decaying probability for high velocities and extremely fast electrons are possible. Often the possibly long extent of the distribution is called "tail". For example, for $k_BT_e = 100\,\mathrm{eV}$ the possibility that an electron has a speed higher than $2 \cdot 10^7$ m/s is about $5 \cdot 10^{-5}$ resulting in statistically 750 electrons above that speed in populations of 15 million electrons. The dependence of the distribution's steepness on the temperature leads to a strong tail for hotter plasmas while the 10 eV case has only a weak tail with less than $4 \cdot 10^{-12}$ probability of a speed over $1 \cdot 10^7$ m/s for a single electron. Although the electrons in the plasma are not monoenergetic, such populations are simulated to check if the resulting currents are dominated by the tail of the Maxwell-Boltzmann distribution which might be possible especially for the simulation of $k_BT_e = 1\,\mathrm{keV}$ due to its large width that can be seen in figure 5.8.

5.1.4 Relativistic effects

For the thermal velocity in typical TJ-K plasmas with $k_B T_e = 10\,\mathrm{eV}$, the Lorentz factor γ is almost unity: $\gamma \approx 1 + 2 \cdot 10^{-5}$. The deviation from 1 is small enough to neglect relativistic effects but for fast non-thermal electrons with energies that are comparable to the electron rest energy relativistic effects come into play. The relativistic mass increase has to be taken into account leading to the Maxwell-Jüttner distribution function [108]. For the thermal velocity, a Lorentz factor of $\gamma \geq 1.01$ is reached when the thermal energy exceeds several thousand electron volts but since the Maxwell distribution has no upper limit for the speed, even for lower thermal energies relativistic electrons have a small but non-zero probability. Therefore, the influence of relativity on the guiding center simulations is sketched here. In order to use the guiding center approximation, it is essential to verify that no serious errors are introduced by this simplification. When relation (5.1) is obeyed, i.e. the magnetic field does not vary significantly on a Larmor radius, the guiding center approximation is valid. Due to the mass dependence of the Larmor radius this relation is influenced by the relativistic mass increase which has to be considered for fast electrons. The mass and hence also the Larmor radius increase proportional to γ. Therefore, in all cases the check for the validity of relation (5.1) is done considering the mass increase in the simulation. Furthermore, it is important to examine the derivation of the guiding center equation of motion for compatibility with relativistic cases. When the full trajectory is considered, the total electron speed is conserved if only a magnetic and no electric field is present. There is only a shift from parallel to perpendicular energy possible when regions with a different field strength are reached. Therefore, the Lorentz factor γ is conserved and only needs to be calculated once for each electron simulation. What remains is the check whether the guiding center equations of motion have to be modified for relativistic cases. The extension of guiding center equations from the classical to the relativistic case is easily understood when no time-varying or strong electric fields are present [103]. The classical derivation from the equation of motion of a charge including the Lorentz force, electrostatic force and arbitrary further forces (like gravitation) is simply extended to the relativistic case by replacing the momentum by the relativistic momentum. This is equivalent to the inclusion of the relativistic mass increase which means that $m_e = \gamma(|\vec{v}|) \cdot m_{e,0}$ with the electron rest mass $m_{e,0}$ is used. The further derivation of drift equations and the parallel motion yield complicated expressions in general but can be simplified depending on the time evolution of the magnetic and electric field [103]. In the electron motion simulations for TJ-K, only a magnetic field without time dependence is used and no electric field is present. In this favorable case, the equation of motion has exactly the same structure as in the non-relativistic case and only the mass has to be replaced by the relativistic mass. Therefore, even a program that does not consider relativistic effects could be used for the simulations as soon as the mass can be inserted manually.

Further details about the more general case that is not needed here are given by T. G. Northrop [103] and information about the time-dependent equations in different coordinate systems is provided by W. A. Cooper [41].

5.1.5 Collisions

The electrons, ions and neutrals in a plasma cannot move freely and independently but they interact through collisions. This is important for thermalization processes as well as particle trajectories in TJ-K. The typical times between collisions τ_{coll} depend on a variety of parameters like plasma temperature, particle velocity, particle densities and ion mass. The collision times and the mean free paths l_{coll} are calculated for typical plasmas and non-thermal electrons in TJ-K in this section. The mean free path will be used as a limit for the trajectory length in the simulations. It is calculated using the momentum relaxation times that describe the thermalization of the velocity in contrast to the energy relaxation time.

The momentum relaxation times are split into the ones parallel and perpendicular to the electron momentum. For the collision between electrons and electrons (index ee), the collision times parallel $\tau_{ee}^{\parallel}$ and perpendicular $\tau_{ee}^{\perp}$ are equal with [54]

$$\tau_{ee} := \tau_{ee}^{\parallel} = \tau_{ee}^{\perp} = \left(\frac{4\pi\varepsilon_0}{e^2}\right)^2 \frac{m_e^2 v^3}{8\pi n_e \ln(\Lambda)}. \tag{5.21}$$

When an electron collides with ions (index ei), the perpendicular collision time is twice as large as the parallel one:

$$\tau_{ei} := \tau_{ei}^{\parallel} = 2 \cdot \tau_{ei}^{\perp} = \left(\frac{4\pi\varepsilon_0}{e^2}\right)^2 \frac{m_e^2 v^3}{4\pi n_e \ln(\Lambda)}, \tag{5.22}$$

where singly ionized ions and $n_i \approx n_e$ are assumed.

The collision time of electrons with neutral atoms τ_{e0} in a gas can be expressed by the electron velocity v, the electron-neutral scattering cross-section σ_{e0} and the neutral gas density n_0:

$$\tau_{e0} = \frac{1}{n_0 v \sigma_{e0}} \tag{5.23}$$

The scattering cross-section is dependent on the gas type and the speed of the electron as shown in figure 5.9.

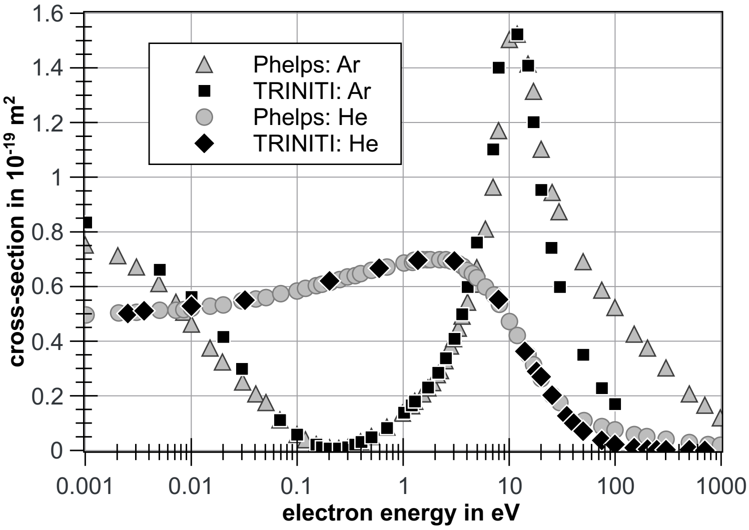

Figure 5.9.: Effective electron-neutral scattering cross-section in He and Ar, retrieved from LXcat [109].

The effective collision cross-sections for electron-neutral encounters include elastic and inelastic scattering which both affect the velocity, its direction or its direction and magnitude, respectively. The data was retrieved from the Phelps [110–114] and TRINITI [115,116] databases using LXcat from the Plasma Data Exchange Project [109]. The calculated values of the TRINITI database are not available for all needed electron energies but confirm the Phelps data over a wide range. At the border of the energies available from TRINITI differences to the measured scattering cross-sections from Phelps are visible. The reduction of the scattering cross-section at low energies is known as the Ramsauer effect [117]. The cross-sections used for the calculations in this work are listed in table 5.1. Those are the values from the Phelps database.

electron energy in eV	$\sigma_{\text{He,eff.}}$ in m^2	$\sigma_{\text{Ar,eff.}}$ in m^2
10	$4.7 \cdot 10^{-20}$	$1.5 \cdot 10^{-19}$
100	$4.8 \cdot 10^{-21}$	$3.5 \cdot 10^{-20}$
1000	$1.7 \cdot 10^{-21}$	$1.2 \cdot 10^{-20}$

Table 5.1.: Effective scattering cross-sections that are used for the calculation of the mean free path for electron trajectory simulations. Based on [109].

Note that these values only represent the order of magnitude and the collision times vary with experimental parameters like the gas type, pressure and individual electron energy. Combined collision processes are dominated by the fastest and the collision times add inversely:

$$\frac{1}{\tau_{coll}} = \sum_{\alpha} \frac{1}{\tau_{\alpha}}. \tag{5.24}$$

To calculate typical collision times for electron-neutral encounters for the gas types helium and argon that are used in this work first the typical neutral gas densities have to be determined. From the neutral gas pressure that is measured before the discharge is started the neutral gas density is estimated by the ideal gas law assuming room temperature. When the discharge is started a fraction of the neutrals is converted to ions and electrons. Thus the typical electron density is subtracted to obtain an estimate of the neutral gas density during the plasma operation.

The typical neutral gas pressures were 52 mPa and 5.2 mPa for helium and argon, respectively. The resulting collision times and the mean free path for helium are shown in table 5.2.

electron energy in eV	v_e in m/s	τ_{ee} in s	τ_{ei} in s	τ_{e0} in s	τ_{coll} in s	l_{coll} in m
10	$1.9 \cdot 10^{6}$	$5.0 \cdot 10^{-7}$	$2.0 \cdot 10^{-6}$	$0.9 \cdot 10^{-7}$	$0.6 \cdot 10^{-7}$	0.1
100	$5.9 \cdot 10^{6}$	$1.3 \cdot 10^{-5}$	$5.0 \cdot 10^{-5}$	$2.8 \cdot 10^{-7}$	$2.7 \cdot 10^{-7}$	1.6
1000	$1.9 \cdot 10^{7}$	$3.3 \cdot 10^{-4}$	$1.3 \cdot 10^{-3}$	$2.5 \cdot 10^{-7}$	$2.5 \cdot 10^{-7}$	4.7

Table 5.2.: Collision times and mean free paths for different thermal energies in TJ-K with ion and electron densities of $6 \cdot 10^{17}\,\text{m}^{-3}$ for helium.

The collision times for argon are calculated analogously. Only the electron-neutral collision time depends on the ion mass such that the values of τ_{ee} and τ_{ei} of table 5.2 also apply to argon plasmas. The ion mass dependent values for argon are listed in table 5.3.

electron energy in eV	v_e in m/s	τ_{e0} in s	τ_{coll} in s	l_{coll} in m
10	$1.9 \cdot 10^6$	$3.0 \cdot 10^{-7}$	$1.1 \cdot 10^{-7}$	0.2
100	$5.9 \cdot 10^6$	$4.0 \cdot 10^{-7}$	$3.7 \cdot 10^{-7}$	2.2
1000	$1.9 \cdot 10^7$	$3.7 \cdot 10^{-7}$	$3.7 \cdot 10^{-7}$	7.0

Table 5.3.: Collision times and mean free paths for different thermal energies in TJ-K with ion and electron densities of $6 \cdot 10^{17}\,\mathrm{m}^{-3}$ for argon.

Compared to argon, the lower scattering cross-section for helium above thermal energies of 5 eV (see figure 5.9) is overcompensated by higher neutral gas pressure leading to the shorter collision times listed in table 5.2. The listed collision times show that the encounters between electrons and neutrals dominate for the chosen parameters leading to very short mean free paths of only a few decimeters for 10 eV electrons up to several meters for fast electrons.

Compared to the electron-neutral collision times calculated here, shorter times are expected outside the confinement region due to the larger neutral gas density. Therefore, also electron-neutral collisions could act as a loss mechanism in addition to the collision with the vessel. The ionization degrees in the investigated argon and helium plasmas are only 4.8 % and 0.48 %, respectively. The collision times outside the confinement region, therefore, only decrease to 95 % and 99.5 % of the value inside the confinement region, respectively. Consequently, this effect is not expected to play a major role.

5.2 Simulation setup and procedure

Electron trajectories are simulated in the 3D magnetic field geometry of TJ-K by following their guiding centers with a step size of $5 \cdot 10^{-4}$ m using MCC. The mean free paths calculated in section 5.1.5 are used to investigate the distance that an electron travels toroidally until this length is reached along the trajectory. This distance is used as a limit for the trajectory simulations. To evaluate the toroidal net currents in one diagnostic plane, the electron velocity distribution is split in one half moving in the positive toroidal direction and the other half moving in the negative toroidal direction. Both halves are started at the toroidal angle that leads to one common plane where the trajectories end, the diagnostic plane at port O5.

To find the toroidal distances, an electron starting with the thermal velocity and $v_\perp = v_\parallel$ in the poloidal plane of port O5 is followed. The full trajectory is calculated until the length of the mean free path is reached. The toroidal angle that was traveled for this distance is evaluated. This procedure is repeated for starting positions on a grid with spacings of 1 cm for the entire confinement region in this poloidal plane. The average of the toroidal angles from these simulations is used as toroidal starting angle with respect to the diagnostic plane in the investigation of toroidal net currents, both in the positive and the negative direction. For the net current simulations, a symmetric geometry at the starting planes is needed to split the velocity distribution simply into two halves. Therefore, the next outer port from these positions is used such that the geometry at both starting planes is equivalent. The different mean free paths depending on the electron energy and gas type also result in different toroidal angles. For each velocity distribution, one representative toroidal angle is used to investigate the electron trajectories.

For the toroidal net current investigations, electron guiding centers are followed from an initially random distribution in the poloidal plane of the starting port with a velocity drawn from the velocity distribution. TJ-K is modeled as a toroidal vessel with the magnetic field generated from the ideally aligned field coils with a current of 1200 A and a current ratio of 57 %. The guiding center motion is followed and the position in the poloidal plane at the diagnostic port O5 and the velocity vector are used for the current calculation. Electrons that are reflected due to the magnetic mirror effect are excluded from the evaluations because they can pass the diagnostic plane several times in alternating direction. When more than 15 million guiding center trajectories have been simulated, the resulting velocities and positions are used to calculate the toroidal current of the final distribution. This large number of electrons is needed to sample the velocity distribution sufficiently fine for each point in the poloidal plane and has been found empirically by calculation of the toroidal current with more and more samples until the result saturates.

The toroidal electron velocities v_t obtained from the electron trajectory simulations can be used to calculate toroidal net currents by integration via weighting with the local electron density at the diagnostic plane as obtained from 2D mapping of the measured 1D density profile analogous to section 4.2.3 and with the electron charge $-e$ as

$$I = \int -e n_e \vec{v} \circ \mathrm{d}\vec{A} = \int -e n_e v_t \mathrm{d}A, \tag{5.25}$$

where dA is the area element. The numerical integration is executed by means of a rectangular grid. In each grid cell the resulting toroidal electron velocities are averaged over all electrons in the cell:

$$I = \sum_{\text{cells}} -e n_e \langle v_t \rangle \Delta A, \tag{5.26}$$

where $\langle v_t \rangle$ is the average of all toroidal electron velocities v_t in an evaluation cell and ΔA is the cell area. The size of the grid cells is optimized with respect to the accuracy of the resulting current. On the one hand, a large cell size leads to a coarse approximation of the density profile. On the other hand, small grid cells lead to a dilute electron population in the cells which in fact decreases the resulting value for the toroidal current as soon as too few electrons for statistical evaluations are present. This becomes clear in the extreme case when each electron has its own cell and smaller cells only lead to a smaller ΔA and more empty cells.

Three different Maxwellian velocity distributions and three more monoenergetic distributions with the (thermal) energies of 10 eV, 100 eV and 1 keV were used to study electron populations in the wide range of energies found in previous Langmuir probe investigations [102]. Velocity distributions with superthermal electrons are investigated by combining the results from the 10 eV Maxwellian distribution with samples drawn from the high-energy distributions which is possible because of the independence of the individual electron trajectories in this model.

5.3 Simulation results and calculation of toroidal net currents

The simulations to find the toroidal distance of the planes where the trajectory simulations are started result in the starting angles listed in table 5.4.

gas type	electron energy in eV	l_{coll} in m	toroidal distance in °	toroidal turns
He	10	0.1	10	1/6
	100	1.6	102	2/6
	1000	4.7	592	10/6
Ar	10	0.2	14	1/6
	100	2.2	143	2/6
	1000	6.9	820	14/6

Table 5.4.: Mean toroidal length of trajectories for given mean free paths and the resulting rounded fraction of toroidal turns for the simulations such that only outer ports are used.

As the mean free paths for He and Ar are similar in the cases of 10 and 100 eV, the same starting angles are obtained. Only for the distribution with 1 keV, separate simulations for He and Ar are needed because the mean free paths result in different starting ports. The electrons for 10 eV simulations are consequently started at the outer ports O4 and O6, from both ports traveling towards port O5. The same starting ports are used for the monoenergetic electron populations.

A grid with 950 cells both in R- and z-direction was found to be suitable to evaluate the toroidal net currents in the poloidal plane. The resulting maximal relative density difference between neighboring cells in the confinement region is only about 2 % and for simulations of 15 million trajectories, the population is on average 65 electrons per cell with no empty cells. The resulting toroidal net currents for the different simulation scenarios are listed in table 5.5 for Maxwellian velocity distributions and monoenergetic populations.

gas	k_BT_e in eV	I in A	I_{mono} in A
He/Ar	10	-7	-5
He/Ar	100	-46	-39
He	1000	-861	-601
Ar	1000	-828	-648

Table 5.5.: Toroidal net current from simulations for different Maxwellian velocity distributions and monoenergetic populations.

All currents have the same direction and they increase with the energy of the electrons as expected due to the increasing average velocity. Toroidal net currents resulting from simulations of monoenergetic populations are significantly smaller than the currents for the corresponding Maxwellian distributions. Since a Maxwellian distribution contains electrons with velocities above the thermal energy, larger drift orbits and more losses are possible which could explain the higher net currents in this case. The net current of -7 A that is expected for a typical electron temperature in TJ-K is of the same order of magnitude as the previously measured net currents in resonant discharges as shown in figure 5.1 on the right. The larger currents in non-resonant discharges as shown on the left in the same figure cannot be explained by the simulation of thermal or monoenergetic electrons in the 10 eV range. Visualizations of the current contributions from the single evaluation grid cells as shown in figure 5.10 and 5.11 reveal that there is a significant contribution from electrons that lie outside the confinement region.

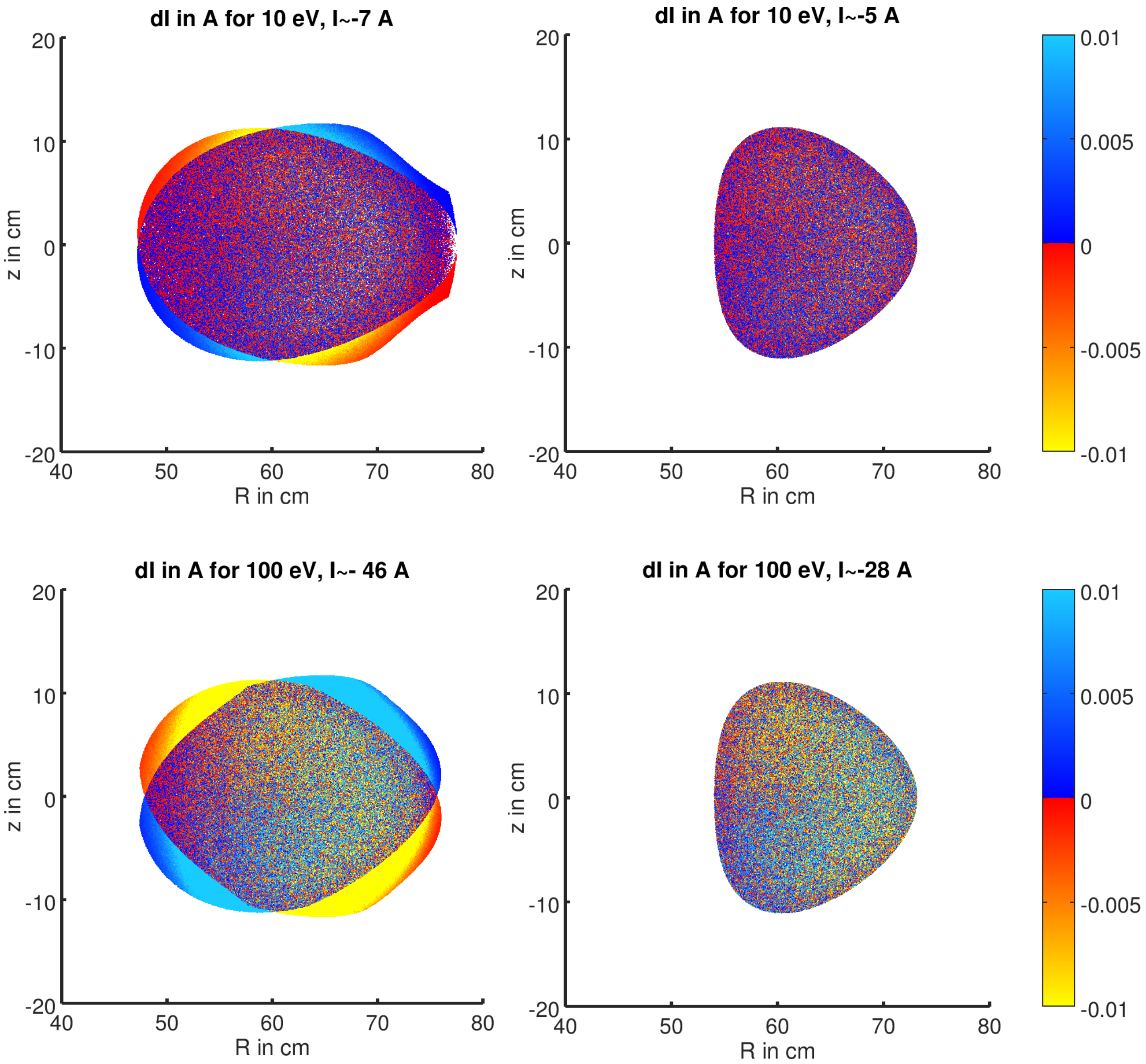

Figure 5.10.: Contributions dI to the total toroidal net current in the poloidal plane of the ECE diagnostic. Complete evaluation on the left and restriction to the confinement region on the right both for 10 eV and 100 eV.

These contributions can be attributed to electrons which not yet hit the vessel wall on their short toroidal path outside the confinement region. For long paths like in the 1 keV simulations, these contributions are strongly reduced because almost all electrons outside the confinement region travel far enough to be collected by the vessel wall. This can be seen when the results are compared with the evaluation restricted to the confinement region as shown in figure 5.10 and 5.11 in the right column. The currents for the confinement region only are listed in table 5.6. The fraction of electrons in the confinement region ("rel. electron count" in the table) shows that for low thermal energies, almost 40 % of the contributing electrons are outside the last closed flux surface while for the high energies this fraction decreases to a negligible number. Nevertheless, also for the high thermal energies, the absolute currents decrease significantly compared to the values in table 5.5 when the evaluation is restricted to the confinement region which shows that the electrons outside the confinement region play an important role for the toroidal net currents. This can also be seen in the structure of the contributions shown in figures 5.10 and 5.11 as large regions with a preferential current direction are visible whereas in the confinement region no large-scale structure is visible.

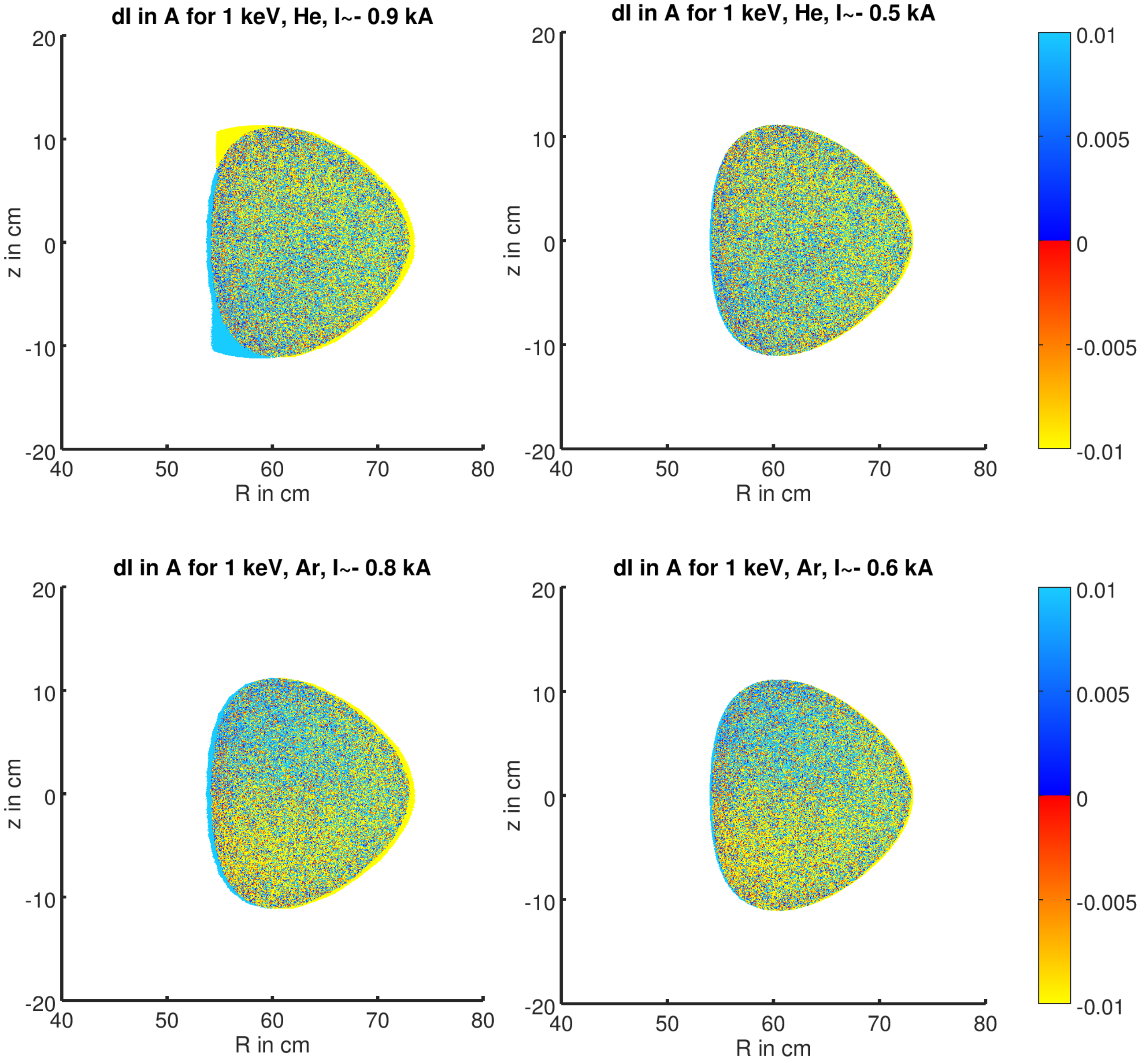

Figure 5.11.: Contributions dI to the total toroidal net current in the poloidal plane of the ECE diagnostic. Complete evaluation on the left and restriction to the confinement region on the right for 1 keV in Ar and He.

gas	$k_B T_e$ in eV	rel. electron count	I in A	I_{mono} in A
He/Ar	10	0.61	-5	-5
He/Ar	100	0.65	-28	-27
He	1000	0.97	-549	-474
Ar	1000	0.99	-588	-518

Table 5.6.: Toroidal net current from simulations for different Maxwellian velocity distributions and monoenergetic populations restricted to the confinement region.

In the case of $k_BT_e = 1\,\mathrm{keV}$, a slight directivity inside the confinement region can be seen: in the case of argon a more positive current is seen in the top region whereas for helium the directivity is opposite. When electrons finish on another flux surface than they started on it is possible that this changes the density distribution in the target plane and, hence, the toroidal net current. For this reason, an alternative approach for the evaluation of the density in the diagnostic plane is tested: the density in the evaluation cell is approximated by the average densities $\langle n_{e,s}\rangle$ of the cells where the electrons in the evaluation cell originate from. The net current is then calculated as

$$I = \sum_{\text{cells}} -e\langle n_{e,s}\rangle\langle v_t\rangle\Delta A, \tag{5.27}$$

where $\langle\cdot\rangle$ is the average over the evaluation cell. The resulting toroidal currents differ only by about 1 % from the values in table 5.5 with this method, showing no trend. Therefore, no significant change of the density profile is expected.

5.3.1 Toroidal net currents from superthermal electrons

Fast electrons are included in the simulations by modification of the input velocity distribution. As basis, the 10 eV Maxwellian distribution is used and electrons from the distribution of fast electrons are added until the desired fraction of fast electrons in the resulting distribution is reached. The normalization of the velocity distribution is anyway done using the electron density profile such that there is no need to renormalize the initial velocity distribution after adding superthermal electrons. Composed distributions with a bulk thermal energy of 10 eV and a fast component of either 100 eV or 1 keV are considered. The fast electrons are either from a Maxwellian or a monoenergetic distribution. The resulting toroidal net currents obtained from the simulations are shown in figure 5.12.

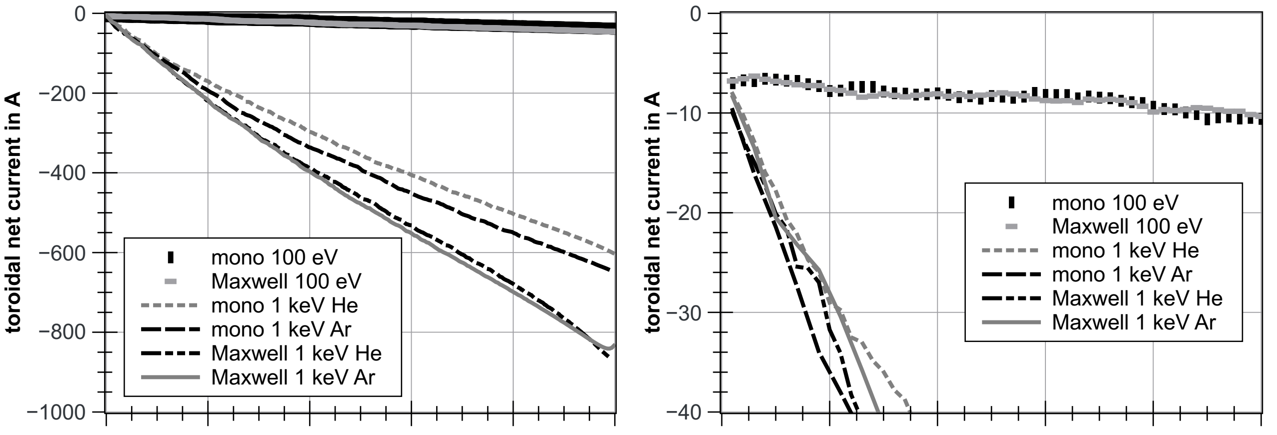

Figure 5.12.: Toroidal net currents for velocity distributions with a 10 eV Maxwellian background and a fraction of superthermal electrons. Combinations with 100 eV and 1 keV fast electrons are shown with Maxwellian and monoenergetic superthermal electron distributions.

As expected, the combinations with higher-energetic superthermals lead to stronger net currents as they increase the average velocity as soon as there is a preferential direction. In addition, the directivity may be enhanced since the drift orbits deviate more from the flux surfaces. Therefore, a higher probability of losses at the vessel wall is expected. Currents from monoenergetic superthermals are lower compared to the Maxwellian counterparts. Since Maxwellian distributions come with a significant high-energetic tail also a higher number of electrons lost due to their drift orbits intersecting with the vessel wall for only one direction with respect to the magnetic field is expected. An increased asymmetry and thus higher toroidal net currents are the consequence.

All resulting currents have a negative sign which means that the negatively charged electrons move on average in the positive x-direction at port O5 that is used for the evaluation. They move clockwise to lower ϕ and antiparallel to the toroidal magnetic field orientation. The same direction was found in the measurements that are shown in figure 5.1 on the right [13]. When the 2.45 GHz magnetron and the 8 GHz klystron were used simultaneously, magnitudes of up to 28 A were seen for low pressures (see figure 5.1). As the zoom on the right of figure 5.12 shows, 1 % of superthermals with 100 eV increases the net current only insignificantly and the current reaches -10 A when a tenth of the electrons are superthermal with 100 eV. According to the simulations, the high currents of $20-30\,\mathrm{A}$ can be generated by $1-2\,\%$ superthermal electrons with an energy of $1\,\mathrm{keV}$ with only slight differences between the gas type or distribution type. The fraction of fast electrons in previous Langmuir probe investigations [102] was 1 % to 10 %.

When a small fraction of fast electrons is added to the bulk plasma, only minor differences between a monoenergetic population of fast electrons or a Maxwellian distribution are seen. The impact of the population type becomes significant when large numbers of fast electrons are present.

5.4 Summary and discussion of the toroidal net current simulations

Simulations have shown for velocity distributions up to 1 keV that the guiding center approximation is valid in TJ-K. The curvature and gradient drift lead to a displacement of charged particle trajectories away from the magnetic field line that depends on the field geometry and the velocity vector at the starting point of the trajectory. When the resulting drift orbits are larger than the confinement region losses at the vessel wall can occur. The direction dependence has been shown in simulations of 15 million electrons of Maxwellian and monoenergetic velocity distributions to produce toroidal net currents that have been evaluated in the poloidal plane at port O5 where the ECE diagnostic is positioned. The direction of the simulated net currents complies with previous measurements. The current strength of measurements with a single resonant microwave heating frequency was reproduced already by simulation conditions of a thermal plasma with $k_B T_e = 10\,\mathrm{eV}$ corresponding to the temperature typically measured in TJ-K plasmas. As expected, distributions with higher velocities (larger $|\vec{v}|$ for monoenergetic distributions or larger T_e for Maxwellian distributions) result in stronger currents. Monoenergetic distributions have resulted in lower current strengths compared to the Maxwellian distributions with the same energy which is expected since the latter have high velocity contributions in the tail.

Large-scale structures with only one preferential direction have been found outside the confinement region. For longer propagation paths the regions outside the confinement region are reduced which can be explained by the trajectories intersecting with the vessel wall. In simulations with $k_B T_e = 1\,\mathrm{keV}$, a slight directivity also inside the confinement region was found. Because of the different sign depending on the toroidal length that was simulated this cannot be explained by Pfirsch-Schlüter currents which would also have a vertical structure in this plane but with fixed current directions. The importance of the edge region for the toroidal currents is in accordance with the observation in previous measurements that toroidal currents are strongly decreased when a Langmuir probe is introduced to the plasma edge. Here the probe may stop electrons and their drift away from the flux surface. Moreover, the distance of a drift orbit from the flux surface is more likely to cause an electron loss for outer flux surfaces as there the vessel is closer. Therefore, it is expected that the outer flux surfaces show a substantial contribution to the generation of toroidal net currents due to drift orbits.

The addition of superthermal electrons has shown an increase of the current strength in the simulations. Already low fractions of fast electrons were found to increase the toroidal net current significantly. Current strengths between 20 A and 30 A as they have occurred in previous measurements with non-resonant heating could be reproduced by only 1 % to 2 % of superthermal electrons with an energy of 1 keV. Compared to monoenergetic superthermals, the net currents are higher when the superthermals constitute an additional Maxwellian-distributed population.

Overall, the simulations have shown that the drift orbits in the 3D magnetic field geometry of TJ-K can generate the magnitude and direction of toroidal net currents as in the previous measurements. Furthermore, 1 % to 2 % of 1 keV electrons can generate the currents from heating scenarios with an additional non-resonant microwave heating and regions with a preferential direction outside the confinement region where identified. Therefore, the simulations support the explanation of toroidal net currents in TJ-K by electron drift orbits.

6 Summary and outlook

An electron cyclotron emission (ECE) diagnostic for the optically thin plasmas of the stellarator TJ-K has been designed, set-up, tested and employed for first successful temperature measurements of the second harmonic X-mode at a fixed frequency of 15 GHz. In comparison to other experiments using ECE as a diagnostic for electron temperature measurements, the plasma in TJ-K and the vacuum vessel exhibit a strong curvature with respect to the wavelength of the ECE. Furthermore, the plasmas are extraordinarily optically thin, imposing a challenge for the setup of the diagnostic at TJ-K. Theoretical considerations of the ECE mechanism and integration of the radiation transport equation have shown that the ECE power of the second harmonic X-mode in TJ-K is expected to scale with the temperature squared as opposed to the linear dependence expected for optically thicker plasmas. Investigations in the full three-dimensional geometry of the magnetic field and electron density using full-wave simulations have been performed to study the volume contributing to signals obtained from the diagnostic. For these simulations, an algorithm to map one-dimensional density and temperature profiles to the entire 3D geometry has been developed and applied. The results from the simulations illustrate that the curvature of the inner vessel wall is unfavorable for localized electron cyclotron emission measurements and that a mirror with optimized curvature can improve the localization by a factor of 2.8 or more. Nevertheless, the localization with such a mirror still does not exceed 26 % with plasma in the simulations. To improve the localization, the concept for the ECE diagnostic setup has been extended to use a diagnostic resonator. The microwave components, namely the receiver antenna, the ECE mirror and the diagnostic resonator have been designed, optimized with the help of simulations, constructed, built and surveyed. Restricted by the space that is available in the vessel of TJ-K, the size of the ECE mirror limits the diagnostic resonator quality factor to 10^3 but still a total improvement factor of the localization of approximately 9 compared to the purely toroidal vessel and a factor of 3.2 compared to the geometry with mirror have been reached. Measurements of the density and temperature dependence that the emitted power shows, as well as the temporal response to heating power modulated experiments, have proven that the measured signals are produced by second harmonic ECE and not by thermal bremsstrahlung. After calibration of the diagnostic with the hot-cold method, the typical ranges and their borders of neutral gas pressures and heating powers of argon and helium plasmas in TJ-K have been scanned in ECE measurements together with Langmuir probe measurements. The resulting electron temperatures from two models were compared: first a linear dependence between temperature and ECE power and second a square dependence. The latter corresponds to the model expected from the integration of the radiation transport equation. The temperature values obtained from the new ECE diagnostic have shown to be in good agreement with Langmuir probe measurements when the square dependence of the ECE power on the temperature is employed. In addition to the temperature measurements in the normal operating range of TJ-K, for very low neutral gas pressures the diagnostic shows high ECE powers which are expected when superthermal electrons are present. Therefore, the diagnostic is suitable to show the limits of the purely thermal operation regimes of TJ-K. The ECE diagnostic at TJ-K is the first account of using a curvature-optimizing mirror and a resonator for the measurements and of using the square temperature dependence of the second harmonic power at optically very thin plasmas.

Motivated by previously measured toroidal net currents and indications of the presence of superthermal electrons in the ECE measurements, the electron drift orbits of thermal and superthermal electrons in TJ-K have been investigated numerically. Starting from the basic drifts away from field lines depending on the electron velocity vector, the formation of drift orbits has been described and illustrated with simulations. Both, drift orbits larger and smaller than the flux surfaces have been shown to appear dependent on the electron's starting point and the orientation compared to the field line. For investigations of the generation of toroidal net currents due to losses from collisions of electrons on larger drift orbits with the vessel wall, the applicability of the guiding center approximation even for relativistic electron energies was checked and simulations of several millions of guiding center trajectories have been performed for Maxwellian and monoenergetic velocity distributions. The mean free paths for the different velocity distributions have been calculated and used to determine the starting points of the electrons in the simulations such that the trajectories end in the diagnostic plane. The calculation of toroidal net currents in this plane has yielded the same current orientation as observed in previous measurements. The current strength of measurements with a single resonant microwave heating system was of the order of 4 A which could be successfully reproduced in the simulations by thermal velocity distributions with $k_BT_e = 10\,\mathrm{eV}$ corresponding to the electron temperature previously measured in these experiments. Monoenergetic distributions result in smaller current strengths as it is expected due to the lack of a high-energetic tail as in a Maxwellian distribution. Visualizations of the local contributions to the toroidal net currents have confirmed that especially the edge and outer regions of the plasma where collisions with the vessel wall are more probable are important for the strength of the toroidal net currents. Furthermore, large-scale regions outside the confinement region with one preferential direction were found, especially for low temperatures. Larger toroidal net currents of 20 A to 30 A as observed in non-resonant heating scenarios have been successfully explained by a fraction of only $1\,\%$ to $2\,\%$ of superthermal electrons with an energy of 1 keV. Generally, also for the superthermal electrons larger currents form when they have a Maxwellian instead of a monoenergetic distribution. The ECE measurements that indicate the presence of superthermal electrons in TJ-K and the simulations of electron trajectories confirm that the previously measured toroidal net currents in TJ-K can be generated by electron drift orbits and superthermal electrons.

Possibilities to extend the setup that allow for the measurement of temperature profiles are of great interest. This can be achieved by using a low-reflection waveguide splitter in order to create tunable resonators for several frequencies extending the currently installed system consisting of a scanning spectrum analyzer with a resonator that can only be tuned to a single frequency. As investigations at TJ-K have a focus on turbulence, drift waves and temperature fluctuations, it is worth noting that ECE diagnostics can also be employed for temperature fluctuation measurements [118] and drift waves show features in ECE spectra [15]. As soon as TJ-K can be operated remotely, it becomes possible to measure the energy of the x-rays produced from fast electrons with differently thick lead shields which also provides information about the energy of the fast electrons. Simultaneous investigation of toroidal net currents and ECE measurements could shed more light on the interplay of fast electrons and net currents. It would be helpful to find a scenario with significant toroidal currents but without x-ray emission, i.e. electron energies that are low enough to prevent x-rays from leaving the vessel. Variation of the rotational transform to investigate the impact on drift orbits, and thus currents, as reported from WEGA [119] could improve the understanding of the geometry influence on the toroidal net currents.

The infrastructure for 3D full-wave simulations, their evaluation and electron trajectory simulations and their evaluation was built in the course of this work and can now be used for further investigations either of the same type with different input parameters or any other microwave or trajectory investigation in TJ-K. Also, the mapping of arbitrary one-dimensional profile to all 3D points in TJ-K on flux surfaces with or without a decay outside the last closed flux surface is now available for any simulations and evaluations of experimental data. Theoretical investigations toward the effects of different vessel geometries including for example different dimensions or the influence of parts like the interferometer mirror or limiters inside the vessel on the 3D density distribution could improve the accuracy of toroidal net current simulations even further.

With remote operation of TJ-K or shielding against ionizing radiation, it would be possible to combine systematic simultaneous measurements of ECE, x-rays and toroidal net currents. When the connection between toroidal net currents and increased ECE signals has been proven experimentally the ECE signals can be used to indicate superthermal electrons or toroidal net currents without the need for a periodic heating power modulation that the previous measurements with a Rogowski coil require. An interesting experiment would be the investigation of the change of the toroidal net current when an obstacle is placed in the regions that show a current contribution in the positive toroidal direction in the simulations compared to the regions where a negative current contribution is predicted.

Altogether, the first ECE diagnostic for extraordinarily optically thin plasmas with a square relation between electron temperature and ECE power has successfully been put into operation and provides temperatures at TJ-K non-invasively. Also, the previously measured toroidal net currents have been explained by simulations of electron drift orbits of thermal plasmas and superthermal electrons.

A Appendix

A.1 Rectangular waveguide properties

designation (IEC)	designation (EIA)	width in mm	cutoff frequency in GHz
R100	WR90	22.86	6.6
R120	WR75	19.05	7.9
R140	WR62	15.80	9.5
R180	WR51	12.95	11.6

Table A.1.: Dimensions and cutoff frequencies of the rectangular waveguides types around the ECE frequency range of TJ-K with the naming according to the IEC (International Electrotechnical Commission) and the EIA (Electronic Industries Association).

A.2 Superposition of measurement signals

The waves emitted by many electrons reach the ECE antenna at the same time. The result of their superposition is calculated for the example of three incoming wave electric fields $\tilde{E}_1$ to $\tilde{E}_3$. The received power P_{rec} is

$$P_{rec} \sim \left(\tilde{E}_1 + \tilde{E}_2 + \tilde{E}_3\right)^2 . \tag{A.1}$$

With slightly different angular frequencies ω_i, amplitudes $\hat{E}_i$ and different phases φ_i this results in

$$\begin{aligned} P_{rec} &\sim \left(\hat{E}_1 \cdot \sin(\omega_1 \cdot t + \varphi_1) + \hat{E}_2 \cdot \sin(\omega_2 \cdot t + \varphi_2) + \hat{E}_3 \cdot \sin(\omega_3 \cdot t + \varphi_3)\right)^2 \\ &= \hat{E}_1^2 \cdot \sin^2(\omega_1 \cdot t + \varphi_1) + \hat{E}_2^2 \cdot \sin^2(\omega_2 \cdot t + \varphi_2) + \hat{E}_3^2 \cdot \sin^2(\omega_3 \cdot t + \varphi_3) \\ &\quad + 2 \cdot [\hat{E}_1\hat{E}_2 \cdot \sin(\omega_1 \cdot t + \varphi_1) \cdot \sin(\omega_2 \cdot t + \varphi_2) \\ &\qquad + \hat{E}_1\hat{E}_3 \cdot \sin(\omega_1 \cdot t + \varphi_1) \cdot \sin(\omega_3 \cdot t + \varphi_3) \\ &\qquad + \hat{E}_2\hat{E}_3 \cdot \sin(\omega_2 \cdot t + \varphi_2) \cdot \sin(\omega_3 \cdot t + \varphi_3)]. \end{aligned} \tag{A.2}$$

After the receiver squares the incoming signal, a low pass filter averages it over time. The sine functions average out and the sum of the squared amplitudes remains in the measured power P_{meas}:

$$P_{meas} \sim \langle P_{rec} \rangle_t \sim \frac{1}{2} \cdot \left(\hat{E}_1^2 + \hat{E}_2^2 + \hat{E}_3^2\right) . \tag{A.3}$$

The prefactor 1/2 from the averaging of the squared sine functions and the general prefactor in the proportionality are then removed in the calibration of the spectrum analyzer. In the example above for three signals from gyrating electrons intermediate steps in the spectrum analyzer are neglected as they do not influence the principle. An actual spectrum analyzer shifts the signals down to lower frequencies by mixing with a local oscillator to analyze the signals in frequency ranges that are easier to cope with. For the shifted frequencies the described process leads to the same result which is also true when a larger number of signals is received.

A.3 Antenna simulation results

Supplementary to the data already shown in section 4.3.1, further frequency trends of beam parameters from the antenna optimization are presented here. The final ECE antenna was optimized for 10 to 20 GHz. As reference, an antenna with a narrow optimization band from 12 to 13 GHz is shown.

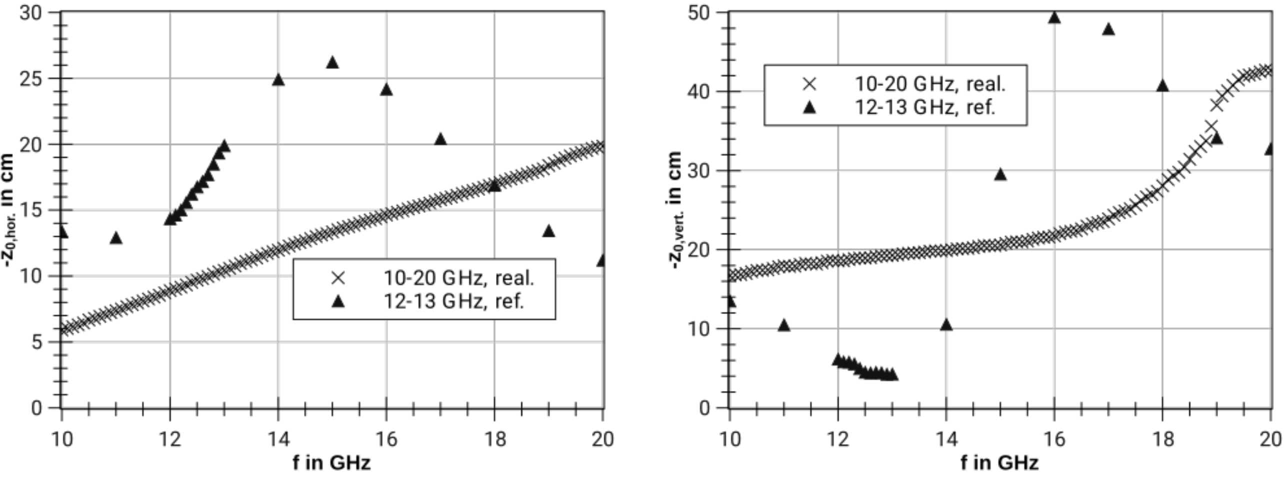

Figure A.1.: Frequency trend of the beam waist position compared to the antenna aperture.

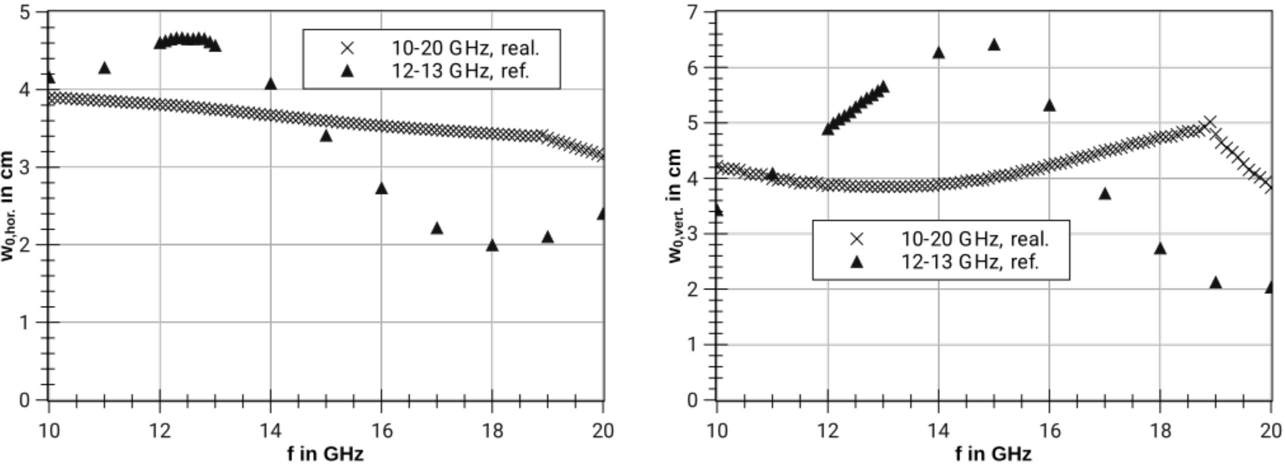

Figure A.2.: Frequency trend of the beam waist width.

A.4 3D full-wave simulation hardware requirements

Each of the simulations described in section 4.2.4 consumes more than 90 GB of RAM in the main loop and needs about 9 days of wall time on 40 threads at 3 GHz. The computational resources at the IGVP do not allow for higher grid resolutions regarding that the memory consumption of the

grid scales cubic in three-dimensional simulations. Reduced RAM needs could in principle be reached by using the limited computational accuracy of single precision floating point data types. But the longer calculation times on 64 bit CPUs for single precision could not be compensated significantly by the faster memory reading times in a test and the resulting data showed deviations from the double precision simulations. Therefore, double precision is preferable and was used for all simulations.
Also, the computational nodes of bwUniCluster [87] do not provide more resources [120] than the IGVP servers. Even a "fat node" of bwUniCluster would not speed up the calculations but at least provide the RAM to double the grid resolution. Unfortunately, this would lead to simulation times of several months on all cores. The current implementation uses openMP [121] for parallelization which requires shared memory and thus restricts the simulation to a single node. Thus the presented simulations show the highest precision that can be simulated in reasonable time on the powerful computational servers available today.

A.5 Phase shifter calibration

A graph of the phase change of the Waveline 708c phase shifter measured with an AB Millimetre MVNA 8-350 GHz Network Analyzer is shown for three different frequencies over the dial indicator position of the phase shifter in figure A.3.

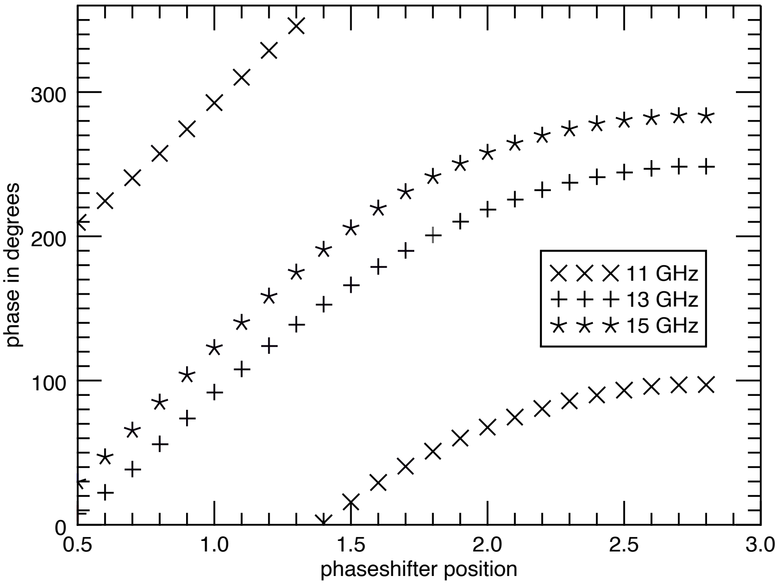

Figure A.3.: Phase shift of the Waveline 708c phase shifter measured with the AB Millimetre Network Analyzer.

As the 0.01 marks of the phase shifter dial can easily be read, the phase shift can be finely tuned.

A.6 Drawings of the ECE diagnostic

On the following pages the construction drawings of the ECE diagnostic are attached including a vertical cut through the antenna mounted in the port extension opposite the ECE mirror in figure A.4, the construction drawing of the ECE mirror in figure A.5 and a drawing that shows the clasp mount for the mirror in figure A.6.

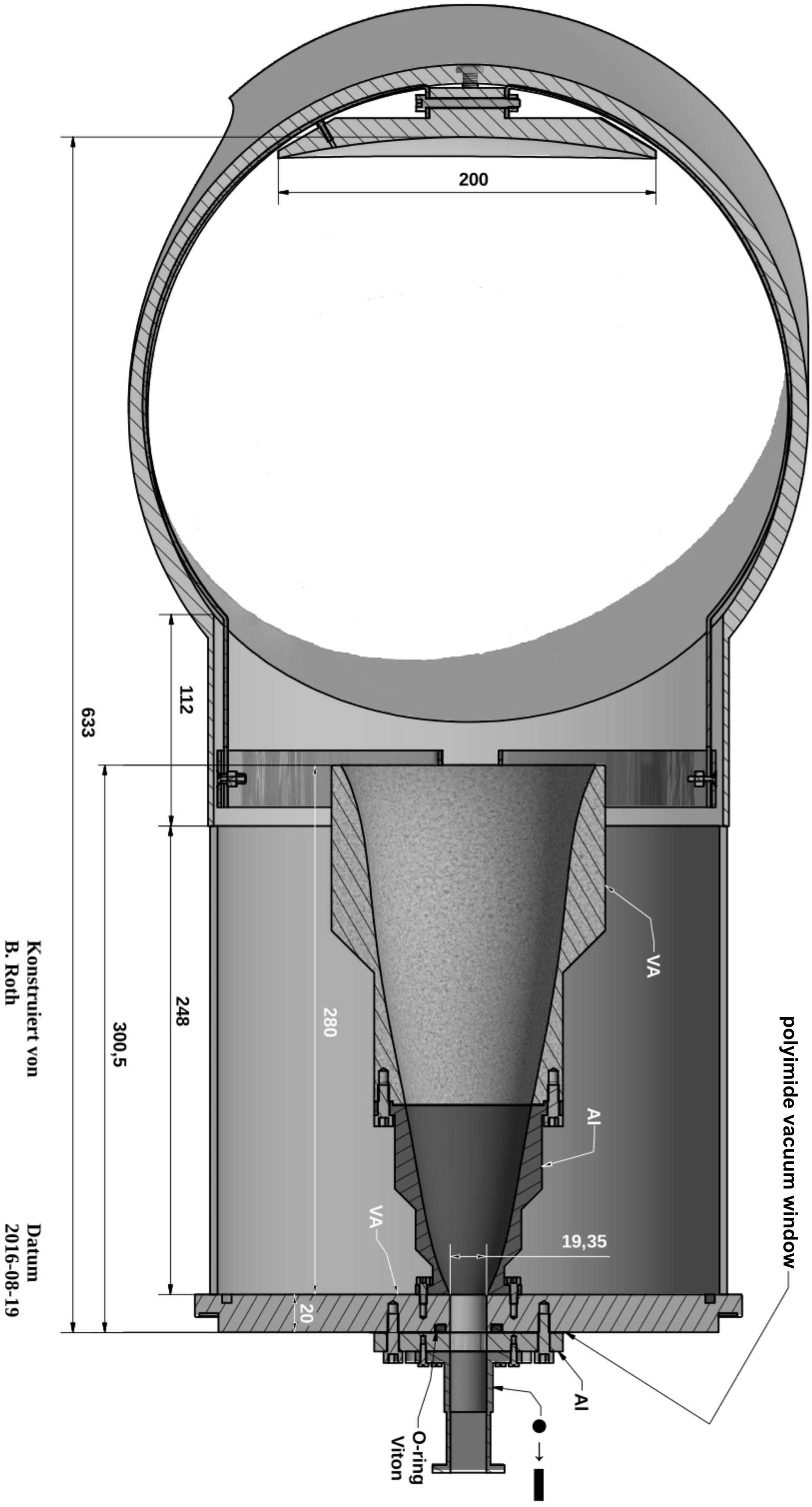
200
633
112
248
300,5
280
20
19,35
VA
Al
VA
Al
polyimide vacuum window
Al
O-ring Viton
Konstruiert von B. Roth
Datum 2016-08-19

Figure A.4.: Drawing of the antenna and the setup in the vacuum vessel in a poloidal cut. All lengths in mm.

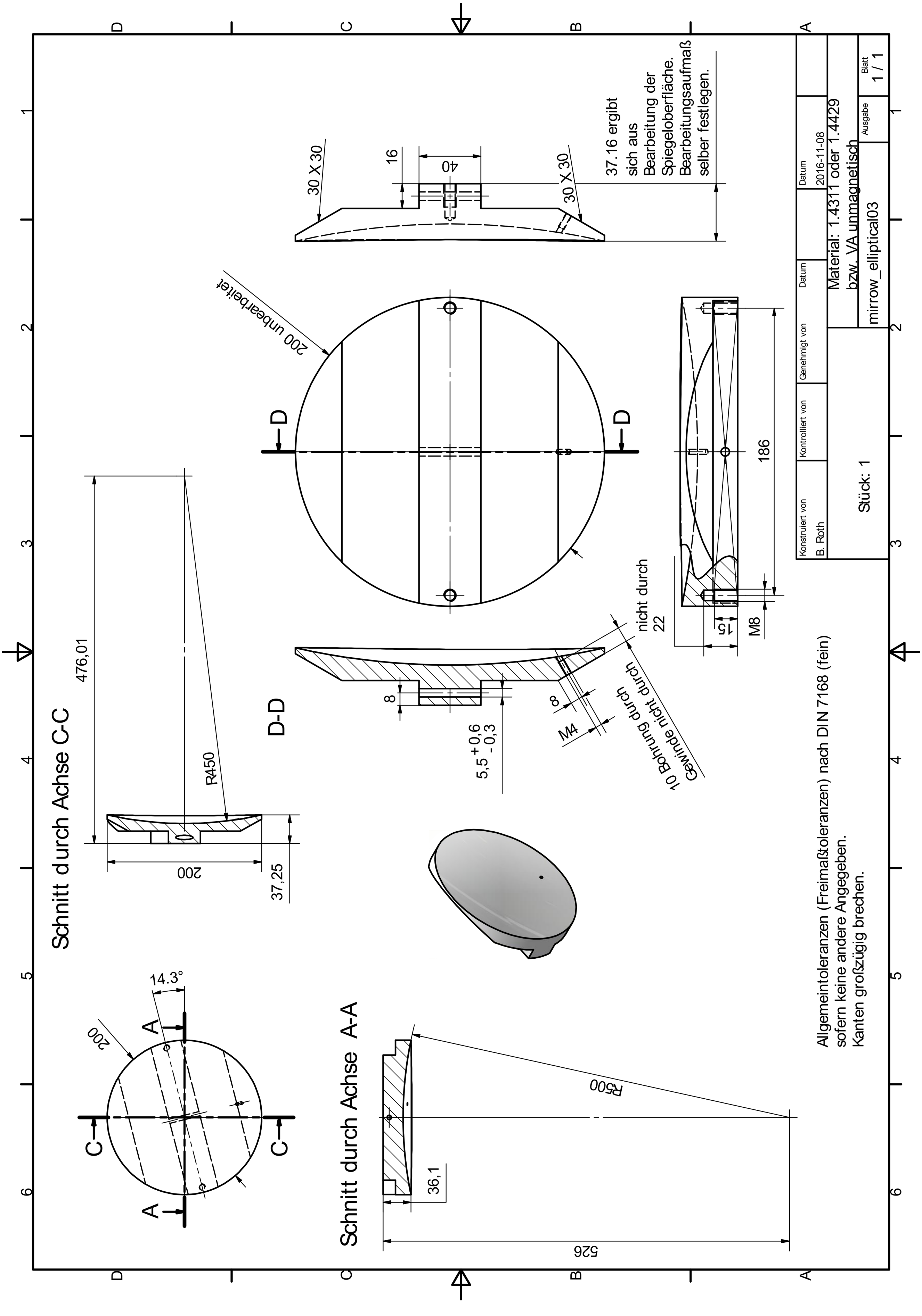
Schnitt durch Achse C-C
476,01
R450
200
37,25
D-D
8
5,5 +0,6 -0,3
8
M4
10 Bohrung durch
Gewinde nicht durch
nicht durch
22
15
M8
186
200 unbearbeitet
D
D
30 X 30
16
40
30 X 30
37.16 ergibt sich aus Bearbeitung der Spiegeloberfläche. Bearbeitungsaufmaß selber festlegen.
Konstruiert von
B. Roth
Kontrolliert von
Genehmigt von
Datum
Datum
Datum
2016-11-08
Material: 1.4311 oder 1.4429 bzw. VA unmagnetisch
Stück: 1
mirrow_elliptical03
Ausgabe
Blatt
1 / 1
Allgemeintoleranzen (Freimaßtoleranzen) nach DIN 7168 (fein) sofern keine andere Angegeben.
Kanten großzügig brechen.
14.3°
200
A
A
C
C
Schnitt durch Achse A-A
R500
36,1
526
A
B
C
D
1
2
3
4
5
6

Figure A.5.: Engineering drawing of the ECE mirror.

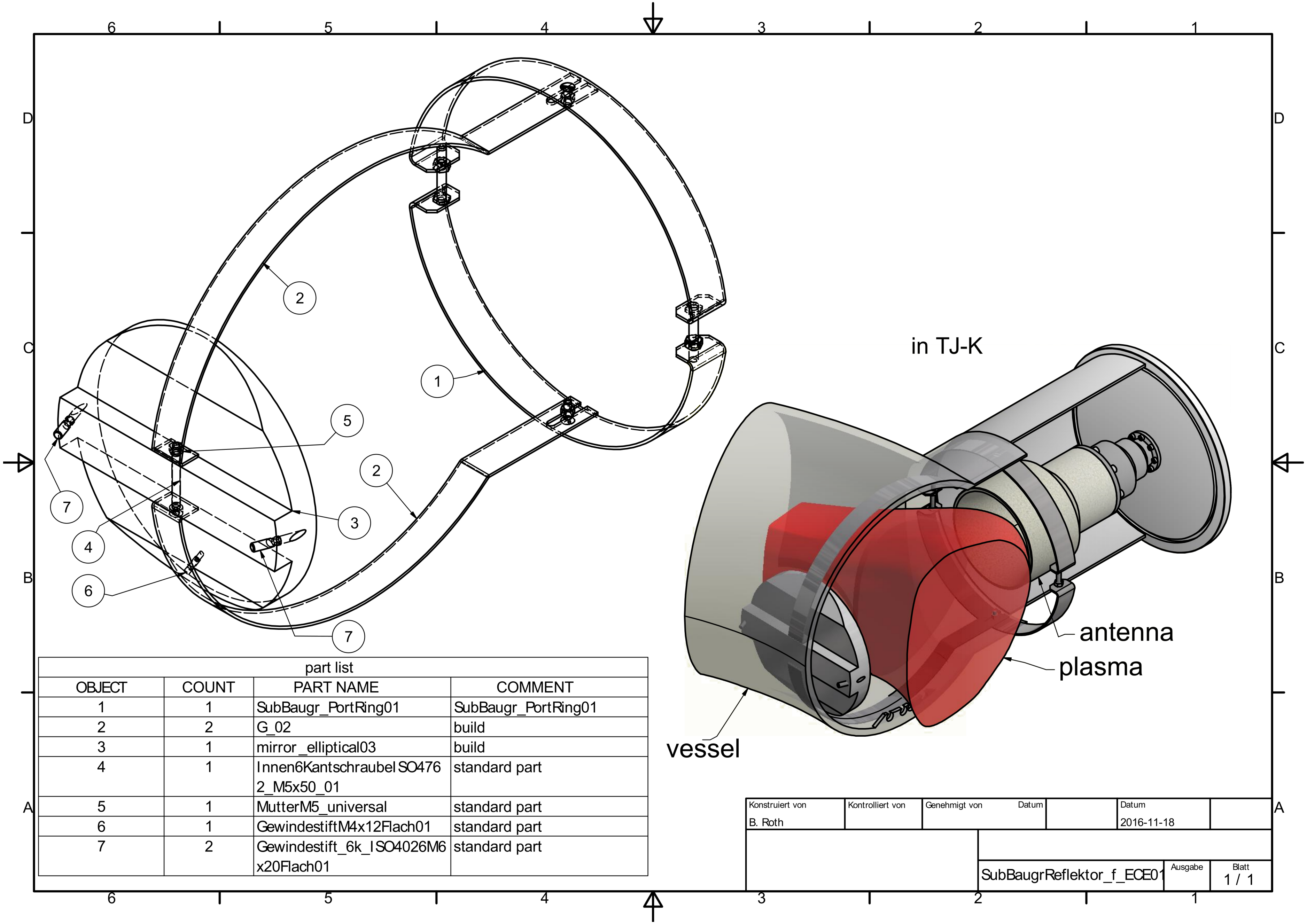

part list			
OBJECT	COUNT	PART NAME	COMMENT
1	1	SubBaugr_PortRing01	SubBaugr_PortRing01
2	2	G_02	build
3	1	mirror_elliptical03	build
4	1	Innen6KantschraubelSO4762_M5x50_01	standard part
5	1	MutterM5_universal	standard part
6	1	GewindestiftM4x12Flach01	standard part
7	2	Gewindestift_6k_ISO4026M6x20Flach01	standard part

6
5
4
3
2
1
D
C
B
A
2
1
5
2
7
3
4
6
7
in TJ-K
antenna
plasma
vessel
Konstruiert von
B. Roth
Kontrolliert von
Genehmigt von
Datum
Datum
2016-11-18
SubBaugrReflektor_f_ECE01
Ausgabe
Blatt
1 / 1

Figure A.6.: Drawing of the ECE mirror mount.

Bibliography

[1] Riccardo d'Agostino, Pietro Favia, Yoshinobu Kawai, Hideo Ikegami, Noriyoshi Sato, and Farzaneh Arefi-Khonsari, editors. *Advanced Plasma Technology.* Wiley-VCH Verlag GmbH & Co. KGaA, Weinheim, Germany, December 2007.

[2] Gregory Fridman, Gary Friedman, Alexander Gutsol, Anatoly B. Shekhter, Victor N. Vasilets, and Alexander Fridman. Applied Plasma Medicine. *Plasma Processes and Polymers*, 5(6):503–533, August 2008.

[3] Hans-Jürgen Hartfuß and Thomas Geist. *Fusion plasma diagnostics with mm-waves: an introduction.* Wiley-VCH-Verl, Weinheim, 2013.

[4] Ulrich Stroth. *Plasmaphysik Phänomene, Grundlagen, Anwendungen.* Vieweg + Teubner Verlag, 2011.

[5] IPP Max-Planck-Institut für Plasmaphysik. Tokamak. https://www.ipp.mpg.de/14869/tokamak, accessed 31.08.18.

[6] A. E. Costley. 50 Years of Electron Cyclotron Emission Research. *Fusion Science and Technology*, 55(1):1–15, January 2009.

[7] Vladimir Krivenski. Electron cyclotron emission by non-Maxwellian bulk distribution functions. *Fusion Engineering and Design*, 53(1-4):23–33, January 2001.

[8] F. J. Stauffer, D. A. Boyd, R. C. Cutler, and M. P. McCarthy. TFTR Michelson interferometer electron cyclotron emission diagnostic. *Review of Scientific Instruments*, 56(5):925–927, May 1985.

[9] M. E. Austin and J. Lohr. Electron cyclotron emission radiometer upgrade on the DIII-D tokamak. *Review of Scientific Instruments*, 74(3):1457–1459, March 2003.

[10] J. W. Hughes, D. A. Mossessian, A. E. Hubbard, E. S. Marmar, D. Johnson, and D. Simon. High-resolution edge Thomson scattering measurements on the Alcator C-Mod tokamak. *Review of Scientific Instruments*, 72(1):1107–1110, January 2001.

[11] Nikolai B. Marushchenko, Volker Erckmann, Hans J. Hartfuss, Mattias Hirsch, Heinrich P. Laqua, Henning Maassberg, and Yuri Turkin. Ray Tracing Simulations of ECR Heating and ECE Diagnostic at W7-X Stellarator. *Plasma and Fusion Research*, 2:S1129–S1129, 2007.

[12] Csaba Stefan Merli. *Magnetische und bolometrische Diagnostik zum Studium des magnetischen Plasmaeinschlusses.* Diploma Thesis, Universität Stuttgart, Stuttgart, July 2010.

[13] A Köhn, G Birkenmeier, A Chusov, P Diez, A Feuer, U Höfel, H Höhnle, E Holzhauer, W Kasparek, S Merli, M Ramisch, J Seifert, S Wolf, and U Stroth. Schemes of microwave heating of overdense plasmas in the stellarator TJ-K. *Plasma Physics and Controlled Fusion*, 55(1):014010, January 2013.

[14] F. Engelmann and M. Curatolo. Cyclotron radiation from a rarefied inhomogeneous magnetoplasma. *Nuclear Fusion*, 13(4):497–507, August 1973.

[15] Christopher Watts. A Review of ECE Correlation Radiometry Techniques for Detection of Core Electron Temperature Fluctuations. *Fusion Science and Technology*, 52(2):176–192, August 2007.

[16] M. Bornatici, R. Cano, O. De Barbieri, and F. Engelmann. Electron cyclotron emission and absorption in fusion plasmas. *Nuclear Fusion*, 23(9):1153–1257, September 1983.

[17] S. Schmuck, H.-J. Hartfuss, M. Hirsch, and T. Stange. Design of the ECE diagnostic at Wendelstein 7-X. *Fusion Engineering and Design*, 84(7-11):1739–1743, June 2009.

[18] Torsten Stange. *Aufbau einer Elektron-Zyklotron-Emissions-Diagnostik am Stellarator WEGA und erste Messungen.* Diploma Thesis, Ernst-Moritz-Arndt-Universität, Greifswald, November 2008.

[19] S. K. Rathgeber, L. Barrera, T. Eich, R. Fischer, B. Nold, W. Suttrop, M. Willensdorfer, E. Wolfrum, and the ASDEX Upgrade Team. Estimation of edge electron temperature profiles via forward modelling of the electron cyclotron radiation transport at ASDEX Upgrade. *Plasma Physics and Controlled Fusion*, 55(2):025004, February 2013.

[20] P. C. Efthimion, V. Arunasalam, R. Bitzer, L. Campbell, and J. C. Hosea. A fast-scanning heterodyne receiver for measurement of the electron cyclotron emission from high-temperature plasmas. *Review of Scientific Instruments*, 50(8):949–951, August 1979.

[21] G. L. Bell and R. F. Gandy. Third harmonic electron cyclotron emission measurements on the Advanced Toroidal Facility. *Nuclear Fusion*, 33(6):875–886, June 1993.

[22] I. H. Hutchinson and D. S. Komm. Electron cyclotron emission in Alcator tokamak. *Nuclear Fusion*, 17(5):1077–1084, October 1977.

[23] N. B. Marushchenko, Y. Turkin, and H. Maassberg. Ray-tracing code TRAVIS for ECR heating, EC current drive and ECE diagnostic. *Computer Physics Communications*, 185(1):165–176, January 2014.

[24] Severin S. Denk, Rainer Fischer, Omar Maj, Emanuele Poli, Jörg K. Stober, Ulrich Stroth, Branka Vanovac, Wolfgang Suttrop, Matthias Willensdorfer, and ASDEX Upgrade Team. Radiation transport modelling for the interpretation of oblique ECE measurements. *EPJ Web of Conferences*, 147:02002, 2017.

[25] V. Tribaldos and B.P. Van Milligen. Electron cyclotron emission calculations for TJ-II stellarator. *Nuclear Fusion*, 36(3):283–293, March 1996.

[26] D.B. Batchelor and R.C. Goldfinger. RAYS: A Geometrical Optics Code for EBT. *ORNL/TM–6844*, (182), 1982.

[27] P. E. Stott, Commission of the European Communities, and International School of Plasma Physics, editors. *Diagnostics for fusion reactor conditions: proceedings of the course held in Varenna (Como), Italy, 6-17 September 1982.* Published for the Commission of the European Communities by Pergamon Press, Oxford ; New York, 1st ed edition, 1983.

[28] Hiroshi Idei, Shin Kubo, Minoru Hosokawa, Harukazu Iguchi, Kunizo Ohkubo, Teruyuki Sato, and Chs group. Electron Cyclotron Emission from Optically Thin Plasma in Compact Helical System. *Japanese Journal of Applied Physics*, 33(Part 1, No. 3A):1543–1549, March 1994.

[29] C.M. Celata and D.A. Boyd. Cyclotron radiation as a diagnostic tool for tokamak plasmas. *Nuclear Fusion*, 17(4):735–759, August 1977.

[30] H. J. Hartfuß, T. Geist, and M. Hirsch. Heterodyne methods in millimetre wave plasma diagnostics with applications to ECE, interferometry and reflectometry. *Plasma Physics and Controlled Fusion*, 39(11):1693–1769, November 1997.

[31] K. Kawahata, Y. Nagayama, S. Inagaki, Y. Ito, and LHD Experimental Group. Broadband electron cyclotron emission radiometry for the large helical device. *Review of Scientific Instruments*, 74(3):1449–1452, March 2003.

[32] M. E. Austin, H. K. B. Pandya, J. Beno, A. D. Bryant, S. Danani, R. F. Ellis, R. Feder, A. E. Hubbard, S. Kumar, A. Ouroua, P. E. Phillips, and W. L. Rowan. Conceptual Design of the ITER ECE Diagnostic – An Update. *EPJ Web of Conferences*, 32:03003, 2012.

[33] Bernhard Pospichal, Gerrit Maschwitz, Nils Küchler, and Thomas Rose. Standing wave patterns at liquid nitrogen calibration of microwave radiometers. *Proceedings of the 9th International Symposium on Tropospheric Profiling*, September 2012.

[34] I. H. Hutchinson. *Principles of plasma diagnostics.* Cambridge University Press, New York, 2. ed., digitally printed first paperback version edition, 2005.

[35] A. E. Costley, R. J. Hastie, J. W. M. Paul, and J. Chamberlain. Electron Cyclotron Emission from a Tokamak Plasma: Experiment and Theory. *Physical Review Letters*, 33(13):758–761, September 1974.

[36] I. Fidone, G. Granata, R. L. Meyer, E. H. Jornada, R. S. Schneider, and L. F. Ziebell. Electron cyclotron emission from tokamak plasmas with mildly superthermal electrons. *Physics of Fluids*, 23(7):1336, 1980.

[37] P N Murgatroyd, A K Y Chu, G K Richardson, D West, G A Yearley, and A J Spencer. Making Rogowski coils. *Measurement Science and Technology*, 2(12):1218–1219, December 1991.

[38] S Tumanski. Induction coil sensors—a review. *Measurement Science and Technology*, 18(3):R31–R46, March 2007.

[39] H P Laqua, E Chlechowitz, M Otte, and T Stange. Stochastic acceleration of relativistic electrons and plasma heating and current drive with 2.45 GHz frequency at the WEGA stellarator. *Plasma Physics and Controlled Fusion*, 56(7):075022, July 2014.

[40] H. P. Zehrfeld, G. Fussmann, and B. J. Green. Electric field effects on relativistic charged particle motion in Tokamaks. *Plasma Physics*, 23(5):473–489, May 1981.

[41] W. A. Cooper. Relativistic guiding centre drift orbits in canonical and magnetic coordinates. *Plasma Physics and Controlled Fusion*, 39(6):931–941, June 1997.

[42] V. Fuchs, H. P. Laqua, J. Seidl, L. Krlín, R. Pánek, J. Preinhaelter, and J. Urban. Relativistic Fermi-Ulam map: Application to WEGA stellarator lower hybrid power operation. *Physics of Plasmas*, 21(6):061513, June 2014.

[43] Peshwaz A. Abdul. Magnetic Configuration Effects on the Torsatron TJ-K Plasma Parameters and Turbulent Transport. Master's thesis, Universität Stuttgart, Stuttgart, 2009.

[44] J. Stöber. *Aufbau eines Mikrowellen-Interferometers für das Torsatron TJ-K*. Diploma Thesis, Christian-Albrechts-Universität, Kiel, 2001.

[45] A. Mlynek, L. Casali, O. Ford, H. Eixenberger, and ASDEX Upgrade Team. Fringe jump analysis and implementation of polarimetry on the ASDEX Upgrade DCN interferometer. *Review of Scientific Instruments*, 85(11):11D408, November 2014.

[46] Anne Zilch. *Untersuchung von Strahlungsverlusten mittels Bolometrie an einem toroidalen Niedertemperaturplasma*. Diploma Thesis, Universität Stuttgart, Stuttgart, Germany, June 2011.

[47] A. Kramida, Yu. Ralchenko, and J. Reader. NIST Atomic Spectra Database, 2018.

[48] S. Semenov and B. Cetegen. Spectroscopic Temperature Measurements in Direct Current Arc Plasma Jets Used in Thermal Spray Processing of Materials. *Journal of Thermal Spray Technology*, 10(2):326–336, June 2001.

[49] F J Gordillo-Vázquez, M Camero, and C Gómez-Aleixandre. Spectroscopic measurements of the electron temperature in low pressure radiofrequency Ar/H $_2$ /C $_2$ H $_2$ and Ar/H $_2$ /CH $_4$ plasmas used for the synthesis of nanocarbon structures. *Plasma Sources Science and Technology*, 15(1):42–51, February 2006.

[50] L. Montgomery Smith, Dennis R. Keefer, and S.I. Sudharsanan. Abel inversion using transform techniques. *Journal of Quantitative Spectroscopy and Radiative Transfer*, 39(5):367–373, May 1988.

[51] V. Senger. *Spektroskopische Bestimmung der Ionentemperatur im TJ-K*. Diploma Thesis, Christian-Albrechts-Universität, Kiel, 2003.

[52] S. Enge. *Untersuchung der Ionendynamik in Laborplasmen - Am Beispiel von Flips und TJ-K*. PhD thesis, Universität Stuttgart, Stuttgart, 2010.

[53] O. A. Muñoz Ovalle. Effects of increased microwave power on the plasma at the stellarator TJ-K. Master's thesis, Universität Stuttgart, Stuttgart, 2015.

[54] Ulrich Stroth. *Plasmaphysik*. Springer Berlin Heidelberg, Berlin, Heidelberg, 2018.

[55] Robert L. Merlino. Understanding Langmuir probe current-voltage characteristics. *American Journal of Physics*, 75(12):1078–1085, December 2007.

[56] Francis F. Chen. Lecture Notes on Langmuir Probe Diagnostics. Jeju, Korea, June 2003.

[57] Richard H. [Herausgeber/in] Huddlestone, editor. *Plasma diagnostic techniques*. Pure and applied physics ; 21. Acad. Press, New York [u.a.], 1965.

[58] P. Manz. *Strukturentstehung in Driftwellenturbulenz toroidaler Plasmen*. Dissertation, Universität Stuttgart, Stuttgart, 2009.

[59] G. Birkenmeier. *Experimentelle Untersuchungen zur Struktur und Dynamik von Driftwellenturbulenz in Stellaratorgeometrie*. PhD thesis, Universität Stuttgart, Stuttgart, 2012.

[60] V. Erckmann and U. Gasparino. Electron cyclotron resonance heating and current drive in toroidal fusion plasmas. *Plasma Physics and Controlled Fusion*, 36(12):1869–1962, December 1994.

[61] M. Løiten. Microwave heating of plasmas with the new 14 GHz system at the stellarator TJ-K. Master's thesis, Universität Stuttgart, Stuttgart, 2013.

[62] Hendrik Höhnle. *Frequenzgesteuerte Arrayantenne zur Elektron-Zyklotron-Resonanz-Heizung mit Berstein-Wellen am Torsatron TJ-K*. Diploma Thesis, Universität Stuttgart, Stuttgart, 2008.

[63] CPI Communications And Power Industries. *Compact Klystron Power Amplifier Installation, Operation, and Preventative Maintenance Manual*. Georgetown, ON, Canada. Doc.01035202 Rev.G.

[64] D. Andruczy, D. N. Ruzic, D. Curreli, J. P. Allain, and HIDRA Team. HIDRA: Hybrid Illinois Device for Research and Applications. *Fusion Science and Technology*, 68(3):497–500, October 2015.

[65] IPP Max-Planck-Institut für Plasmaphysik. WEGA technische Daten der Anlage. https://www.ipp.mpg.de/89572/WEGA_technisch accessed 19.07.2018.

[66] H. Idei, K. Ida, H. Sanuki, H. Yamada, H. Iguchi, S. Kubo, R. Akiyama, H. Arimoto, M. Fujiwara, M. Hosokawa, K. Matsuoka, S. Morita, K. Nishimura, K. Ohkubo, S. Okamura, S. Sakakibara, C. Takahashi, Y. Takita, K. Tsumori, and I. Yamada. Transition of the radial electric field by electron cyclotron heating in the CHS heliotron/torsatron. *Physical Review Letters*, 71(14):2220–2223, October 1993.

[67] M. Takeuchi, K. Toi, K. Nagaoka, C. Suzuki, T. Minami, T. Akiyama, M. Isobe, Y. Yoshimura, S. Nishimura, A. Shimizu, C. Takahashi, K. Matsuoka, S. Okamura, and the CHS Experimental Group. Study of an edge transport barrier by Langmuir probes in the compact helical system. *Plasma Physics and Controlled Fusion*, 48(5A):A277–A283, May 2006.

[68] IPP Max-Planck-Institut für Plasmaphysik. ASDEX UPGRADE fusion experiment. https://www.ipp.mpg.de/987491/AUG_engl.pdf accessed 19.07.2018.

[69] I. G. J. Classen, J. E. Boom, W. Suttrop, E. Schmid, B. Tobias, C. W. Domier, N. C. Luhmann, A. J. H. Donné, R. J. E. Jaspers, P. C. de Vries, H. K. Park, T. Munsat, M. García-Muñoz, and P. A. Schneider. 2d electron cyclotron emission imaging at ASDEX Upgrade (invited). *Review of Scientific Instruments*, 81(10):10D929, October 2010.

[70] IPP Max-Planck-Institut für Plasmaphysik. Wendelstein 7-X fusion experiment. https://www.ipp.mpg.de/3766317/W7-XFlyer_engl_2014.pdf, accessed 19.07.2018.

[71] G. Bekefi. *Radiation processes in plasmas.* Wiley series in plasma physics. Wiley, 1966.

[72] T. H. Stix. *Waves in plasmas.* American Institute of Physics, New York, 1992.

[73] M. Dressel, O. Klein, S. Donovan, and G. Grüner. High frequency resonant techniques for studying the complex electrodynamic response in solids. *Ferroelectrics*, 176(1):285–308, February 1996.

[74] C. Lechte. Investigation of the Scattering Efficiency in Doppler Reflectometry by Two-Dimensional Full-Wave Simulations. *IEEE Transactions on Plasma Science*, 37(6):1099–1103, June 2009.

[75] Lennart Bock. Numerical Investigation of Microwave Propagation at the Stellarator TJ-K. Master's thesis, Universität Jena, Universität Stuttgart, July 2017.

[76] Allen Taflove and Susan C. Hagness. *Computational electrodynamics: the finite-difference time-domain method.* Artech House antennas and propagation library. Artech House, Boston, 2nd ed edition, 2000.

[77] Kane Yee. Numerical solution of initial boundary value problems involving maxwell's equations in isotropic media. *IEEE Transactions on Antennas and Propagation*, 14(3):302–307, May 1966.

[78] Alf Köhn. *Investigation of microwave heating scenarios in the magnetically confined low-temperature plasma of the stellarator TJ-K.* PhD thesis, Universität Stuttgart, Germany, 2010.

[79] E. R. Tracy and A. J. Brizard. *Ray tracing and beyond: phase space methods in plasma wave theory.* Cambridge University Press, Cambridge, United Kingdom ; New York, 2014.

[80] Edmund Stirner. *Antennen.* Hüthig, Heidelberg, 1977.

[81] W. Dällenbach. Der Reziprozitätssatz des elektromagnetischen Feldes. *Archiv für Elektrotechnik*, 36(3):153–165, March 1942.

[82] J. R. Carson. Reciprocal Theorems in Radio Communication. *Proceedings of the Institute of Radio Engineers*, 17(6):952–956, June 1929.

[83] A.T. Villeneuve and R.F. Harrington. Reciprocity Relationships for Gyrotropic Media. *IEEE Transactions on Microwave Theory and Techniques*, 6(3):308–310, July 1958.

[84] L. Bergmann and H. Lassen, editors. *Ausstrahlung, Ausbreitung und Aufnahme Elektromagnetischer Wellen.* Springer Berlin Heidelberg, Berlin, Heidelberg, 1940.

[85] C. Gourdon. *Programme optimisé de calculs numériques dans les configurations magnétiques toroïdales.* Centre d'études nucléaires de Fontenay-aux-Roses, Fontenay-aux-Roses, 1970.

[86] C. Lechte, E. Holzhauer, U. Stroth, and G. D. Conway. Full Wave Doppler Reflectometry Simulations in 2d. In *Proceedings of the 8th International Reflectometry Workshop for Fusion Plasma Diagnostics*, St. Petersburg, Russia, 2007.

[87] State of Baden-Württemberg. BwUniCluster. http://www.bwhpc-c5.de/, accessed 14.03.2018.

[88] Hank Childs, Eric Brugger, Brad Whitlock, Jeremy Meredith, Sean Ahern, David Pugmire, Kathleen Biagas, Mark Miller, Cyrus Harrison, Gunther H. Weber, Hari Krishnan, Thomas Fogal, Allen Sanderson, Christoph Garth, E. Wes Bethel, David Camp, Oliver Rübel, Marc Durant, Jean M. Favre, and Paul Navrátil. VisIt: An End-User Tool For Visualizing and Analyzing Very Large Data. In *High Performance Visualization–Enabling Extreme-Scale Scientific Insight*, pages 357–372. October 2012.

[89] Burkhard Plaum. Simulation of microwave beams with PROFUSION. Technical report, Universität Stuttgart, February 2019.

[90] Burkhard Plaum. Optimization of Broadband Smooth-Wall Circular Horn Antennas. *Journal of Infrared, Millimeter, and Terahertz Waves*, June 2018.

[91] Nathan Marcuvitz. *Waveguide handbook.* Number 21 in IEE electromagnetic waves series. P. Peregrinus on behalf of the Institution of Electrical Engineers, London, UK, 1986.

[92] A. Yu. Nikitin, D. Zueco, F. J. García-Vidal, and L. Martín-Moreno. Electromagnetic wave transmission through a small hole in a perfect electric conductor of finite thickness. *Physical Review B*, 78(16), October 2008.

[93] Frank Gustrau. *RF and microwave engineering: fundamentals of wireless communications.* Wiley, Chichester Hoboken, N.J, 2012.

[94] John David Jackson. *Classical electrodynamics.* Wiley, New York, 1962. OCLC: 535998.

[95] AK Steel. 316/316L stainless steel product data bulletin. Technical report. www.aksteel.com/sites/default/files/2018-01/316316L201706_2.pdf, accessed 25.02.2019.

[96] Wolfgang Demtröder. *Elektrizität und Optik.* Springer, Berlin, 2006. OCLC: 728079504.

[97] Bahaa E. A Saleh and Malvin Carl Teich. *Fundamentals of photonics.* 2001. OCLC: 835420736.

[98] Gregor Birkenmeier. *Experiments and Modeling of Transport Processes in Toroidal Plasmas.* Diploma Thesis, Universität Stuttgart, Stuttgart, Germany, 2008.

[99] J. Zhang, N. A. Crocker, T. A. Carter, S. Kubota, and W. A. Peebles. Interaction between Faraday rotation and Cotton–Mouton effects in polarimetry modeling for NSTX. *Review of Scientific Instruments*, 81(10):10D519, October 2010.

[100] A. E. Costley. Measurements of Electron Cyclotron Emission from High-Density Tokamak Plasmas in TFR. *Physical Review Letters*, 38(25):1477–1480, June 1977.

[101] C. Alejaldre, J. Alonso, L. Almoguera, E. Ascasíbar, A. Baciero, R. Balbín, M. Blaumoser, J. Botija, B. Brañas, E. de la Cal, A. Cappa, R. Carrasco, F. Castejón, J. R. Cepero, C. Cremy, J. Doncel, C. Dulya, T. Estrada, A. Fernández, M. Francés, C. Fuentes, A. García, I. García-Cortés, J. Guasp, J. Herranz, C. Hidalgo, J. A. Jiménez, I. Kirpitchev, V. Krivenski, I. Labrador, F. Lapayese, K. Likin, M. Liniers, A. López-Fraguas, A. López-Sánchez, E. de la Luna, R. Martín, A. Martínez, M. Medrano, P. Méndez, K. McCarthy, F. Medina, B. van Milligen, M. Ochando, L. Pacios, I. Pastor, M. A. Pedrosa, A. de la Peña, A. Portas, J. Qin, L. Rodríguez-Rodrigo, A. Salas, E. Sánchez, J. Sánchez, F. Tabarés, D. Tafalla, V. Tribaldos, J. Vega, B. Zurro, D. Akulina, O. I. Fedyanin, S. Grebenshchicov, N. Kharchev, A. Meshcheryakov, R. Barth, G. van Dijk, H. van der Meiden, and S. Petrov. First plasmas in the TJ-II flexible Heliac. *Plasma Physics and Controlled Fusion*, 41(3A):A539–A548, March 1999.

[102] Björn May. *Nichtthermische Elektronen in ECR-Entladungen in TJ-K.* Diploma Thesis, Christian-Albrechts-Universität, Kiel, 2005.

[103] T G Northrop. *The adiabatic motion of charged particles.* Number xiv, 109 p. in Interscience tracts on physics and astronomy,21. Interscience Publishers, New York, 1963.

[104] S. E. Grebenshchikov, I. S. Danilkin, and M. A. Tereshchenko. Properties of the drift trajectories of oppositely propagating particles in a stellarator with a magnetic shear. *Plasma Physics Reports*, 35(12):1005–1012, December 2009.

[105] Wolfgang Demtröder. *Experimentalphysik 1.* Springer-Lehrbuch. Springer Berlin Heidelberg, Berlin, Heidelberg, 2015.

[106] G. E. P. Box and Mervin E. Muller. A Note on the Generation of Random Normal Deviates. *The Annals of Mathematical Statistics*, 29(2):610–611, June 1958.

[107] Peyton Z. Peebles. *Probability, random variables, and random signal principles.* Communications and information theory. McGraw-Hill, New York, 1980.

[108] A. Aliano, L. Rondoni, and G. P. Morriss. Maxwell-Jüttner distributions in relativistic molecular dynamics. *The European Physical Journal B*, 50(1-2):361–365, March 2006.

[109] Plasma Data Exchange Project. LXcat. www.lxcat.net, acccessed on February 20, 2019.

[110] A V Phelps. Phelps database. www.lxcat.net/Phelps, retrieved on February 20, 2019.

[111] C. Yamabe, S. J. Buckman, and A. V. Phelps. Measurement of free-free emission from low-energy-electron collisions with Ar. *Physical Review A*, 27(3):1345–1352, March 1983.

[112] R. W. Crompton, M. T. Elford, and R. L. Jory. The Momentum Transfer Cross Section for Electrons in Helium. *Australian Journal of Physics*, 20(4):369, 1967.

[113] H. B. Milloy and R. W. Crompton. Momentum-transfer cross section for electron-helium collisions in the range 4-12 eV. *Physical Review A*, 15(5):1847–1850, May 1977.

[114] M. Hayashi. Recommended values of transport cross sections for elastic collision and total collision cross section for electrons in atomic and molecular gases. Technical report, Institute of Plasma Physics, Nagoya University, Japan, 1981.

[115] I. Kochetov. TRINITI database. www.lxcat.net/TRINITI , retrieved on February 20, 2019.

[116] J. L. Pack, R. E. Voshall, A. V. Phelps, and L. E. Kline. Longitudinal electron diffusion coefficients in gases: Noble gases. *Journal of Applied Physics*, 71(11):5363–5371, June 1992.

[117] Carl Ramsauer. Über den Wirkungsquerschnitt der Gasmoleküle gegenüber langsamen Elektronen. *Annalen der Physik*, 369(6):513–540, 1921.

[118] S. Sattler and H. J. Hartfuss. Experimental evidence for electron temperature fluctuations in the core plasma of the W7-AS stellarator. *Physical Review Letters*, 72(5):653–656, January 1994.

[119] H P Laqua, E Chlechowitz, M Dostal, M Otte, and T Stange. The Generation and Confinement of Relativistic Electrons at the WEGA Stellarator. *41st EPS Conference on Plasma Physics, Berlin*, 2014.

[120] Karlsruhe Institute of Technology. Konfiguration des bwUniCluster. http://www.scc.kit.edu/dienste/bwUniCluster.php, accessed 14.03.2018.

[121] Leonardo Dagum and Ramesh Menon. OpenMP: an industry standard API for shared-memory programming. *Computational Science & Engineering, IEEE*, 5(1):46–55, 1998.

Danksagung

Für die vielen Beiträge zum Gelingen dieser Arbeit möchte ich mich bedanken, vor allem bei:

Herrn Prof. Dr. Thomas Hirth für die Übernahme der Betreuung als Doktorvater und damit Ermöglichung dieser Arbeit und den Hauptbericht,

sowie Prof. Dr. Marc Kreutzbruck und Priv.-Doz. Dr. Heinrich P. Laqua für den Mitbericht,

Priv.-Doz. Dr. Laqua außerdem für die nützlichen Diskussionen,

Dr. Eberhard Holzhauer für die Unterstützung im Labor, bei Simulationen und bei Diskussionen unter hohem Zeitaufwand,

Dr. Alf Köhn für die gemeinsamen Experimente und geduldige Beratung, auch per Videokonferenz,

Dr. Mirko Ramisch für die Gruppenleitung, die Bereitstellung von MCC und die Beratung,

Bernhard Roth für die stete Hilfsbereitschaft beim Experimentaufbau, sowie den Entwurf von Bauteilen,

Dr. Walter Kasparek für viele hilfreiche Tipps und Diskussionen zu Messungen mit Mikrowellen und das Verleihen von Messgeräten,

Dr. Burkhard Plaum für die Pflege der IT, die Gespräche über Mikrowellen und die Hilfe bei der Antennenoptimierung mit PROFUSION,

Dr. Carsten Lechte für die Bereitstellung von IPF-FD3D und Unterstützung bei der Anwendung,

Lennart Bock für die Basis der 3D Full-Wave Simulationen für TJ-K,

den Teams der mechanischen und elektrischen Werkstatt, ohne die weder Instandhaltung vorhandener noch Aufbau neuer Diagnostiken möglich wären,

Frau Wagner für ihre Hilfsbereitschaft und Organisation,

Til Ullmann, Dr. Bernhard Schmid, Stephen Garland und den anderen Doktoranden für die fachlichen, technischen und privaten Gespräche,

Dr. Torsten Stange für die Diskussionen aufbauend auf seiner Diplomarbeit und darüber hinaus,

meinen Eltern Birgit und Andreas, meinem Bruder Lucas und meiner Frau Janina für die Wegbereitung zur Promotion und beständige Unterstützung neben der Arbeit.

Eigenständigkeitserklärung

Hiermit erkläre ich, dass ich die vorliegende Arbeit selbstständig verfasst und dazu keine anderen als die angegebenen Quellen und Hilfsmittel verwendet habe und dass alle Stellen, die wörtlich oder sinngemäß anderen Arbeiten entnommen wurden, durch Angabe der Quellen kenntlich gemacht sind.

Stuttgart, den

Gabriel Sichardt